Optimisation and Evaluation of Antibody-Based Immuno-PET/SPECT Imaging of Intranuclear Epitopes



Mathew Veal

Lincoln College

University of Oxford

A thesis submitted for the degree of

Doctor of Philosophy

Michaelmas Term 2020

Contents

CONTENTS ..... **II**

LIST OF FIGURES ..... **VII**

LIST OF TABLES ..... **IX**

ACKNOWLEDGEMENTS ..... **X**

ABSTRACT ..... **XII**

ABBREVIATIONS ..... **XIV**

CHAPTER 1 - GENERAL INTRODUCTION **1**

1.1 CANCER AND MOLECULAR IMAGING 1

1.1.1 What is cancer? *1*

1.1.2 Molecular imaging and cancer *2*

1.1.3 Advantages of molecular imaging over conventional diagnostic tools *3*

1.1.4 Basic Principles and Impact of PET/SPECT imaging *4*

1.1.5 Benefits and drawbacks of PET/SPECT imaging *7*

1.2 ANTIBODY BASED NUCLEAR IMAGING 9

1.2.1 Introduction to monoclonal antibodies *9*

1.2.3 Molecular imaging using antibody fragments *12*

1.4 ANTIBODY CONJUGATION STRATEGIES 14

1.4.1 Overview of antibody conjugation strategies *14*

1.4.2 Antibody conjugation of naturally occurring moieties *16*

1.4.3 Antibody conjugation using unnatural or engineered moieties *18*

1.5 CELL PENETRATING PEPTIDES 19

1.5.1 Introduction and classification of cell penetrating peptides *19*

1.5.2 Mechanisms of internalisation *20*

1.5.3 Direct translocation mechanisms of CPP internalisation *21*

1.5.4 Endocytosis-dependent mechanisms of CPP internalisation *23*

1.5.5 CPP internalisation by macropinocytosis *24*

1.5.5 CPP internalisation by clathrin-mediated endocytosis (CME) *26*

1.5.6 CPP internalisation by caveolae-mediated endocytosis (CvME) *27*

1.5.7 CPP internalisation by other endocytic mechanisms *27*

1.5.8 Endosomal release of CPPs *28*

1.5.9 Mechanisms of endosomal escape of CPPs *29*

1.6 TAT-IgG BASED MOLECULAR IMAGING OF INTRANUCLEAR EPITOPES 30

1.6.1 Overcoming cellular barriers *30*

1.6.2 The TAT peptide *30*

1.6.3 Conjugation of TAT-IgG RICs *32*

1.7 AIMS OF THE STUDY 33

CHAPTER 2 - DEVELOPMENT OF A GFP-BASED MODEL SYSTEM TO EVALUATE THE LIMITATIONS OF IGG-TAT-BASED IMAGING OF INTRANUCLEAR EPITOPES 36

2.1 INTRODUCTION 36

2.2 MATERIALS AND METHODS 38

2.2.1 Cell culture *38*

2.2.2 Stable transfection of H1299 cells *38*

2.2.3 Western blot *39*

2.2.4 Immunofluorescence microscopy *40*

2.2.5 Flow cytometry *41*

2.2.6 Enzyme linked immunosorbent assay (ELISA) *41*

2.2.7 H2B-EGFP copy number determination *42*

2.2.7 Hybridoma cell culture *42*

2.2.8 Antibody supernatant Protein G purification *43*

2.2.8 Statistical analysis *44*

2.3 RESULTS 44

2.3.1 Validation of transient expression of H2B-EGFP expression system *44*

2.3.2 Establishment of stably transfected H2B-EGFP cell population *45*

2.3.3 Selection and evaluation of H2B-EGFP clone cell lines. *46*

2.3.4 Expression stability of H2B-EGFP clones *48*

2.3.5 Validation and evaluation of murine monoclonal antibody GFP-G1 ..... *50*

DISCUSSION 52

CHAPTER 3 - DESIGN AND EVALUATION OF A NOVEL CONJUGATION APPROACH TO PRODUCE IGG-TAT BASED RADIOIMMUNOCONJUGATES 56

3.1 INTRODUCTION 56

3.2 MATERIALS AND METHODS 59

3.2.1 Preparation of antibody conjugates by EDC/NHS crosslinking method *59*

3.2.2 Preparation of antibody conjugates by DBCO-N3 click chemistry method *60*

3.2.3 Radiolabelling DTPA-Bn-IgG-TAT conjugates with $^{111}InCl_3$ *61*

3.2.4 Stability assay *61*

3.2.5 Cell-free radioimmunoassay (RIA) *62*

3.2.6 Cell culture *62*

3.2.7 Colony formation assay *63*

3.2.8 Cell uptake study *63*

3.3 RESULTS 64

3.3.1 Optimisation of antibody conjugation with STP-DBCO linker *64*

3.3.2 Optimisation of TAT-N_3 and DTPA-Bn-N_3 conjugation *65*

3.3.3 Radiolabelling and stability of DTPA-GFP-G1-TAT RICs *67*

3.3.4 Comparison of blocking properties of DTPA-GFP-G1-TAT RICs *67*

3.3.5 Investigation into toxicity of DTPA-GFP-G1-TAT RICs *69*

3.3.6 In vitro uptake comparison of DTPA-GFP-G1-TAT RICs *70*

3.4 DISCUSSION 71

CHAPTER 4 - INVESTIGATING THE DETECTION LIMITS OF ANTIBODY-BASED IMMUNO-PET/SPECT IMAGING OF INTRANUCLEAR EPITOPES 75

4.1 INTRODUCTION 75

4.2 MATERIALS AND METHODS 76

4.2.1 Cell culture *76*

4.2.2 Bioconjugation of murine monoclonal antibody GFP-G1 ..... *77*

4.2.3 Radiolabelling of DTPA-Bn-GFP-G1-TAT with $^{111}InCl_3$ *78*

4.2.4 In vitro uptake of ^{111}In-DTPA-GFP-G1-TAT *78*

4.2.5 In vivo xenograft uptake of ^{111}In-DTPA-GFP-G1-TAT *78*

4.2.6 SPECT/CT acquisition and image analysis *79*

4.2.7 Statistical analysis *80*

4.3 RESULTS 81

4.3.1 In vitro cellular uptake of ^{111}In-DTPA-GFP-G1-TAT *81*

4.3.2 Biodistribution of ^{111}In-DTPA-GFP-G1 in an in vivo xenograft model *82*

4.3.3 Evaluation of ^{111}In-DTPA-GFP-G1-TAT tumour uptake by SPECT/CT image analysis. *83*

4.4 DISCUSSION 85

CHAPTER 5 - IMAGING PHOSPHO-ATM USING ANTIBODY-BASED PET/SPECT IMAGING 89

5.1 INTRODUCTION 89

5.2 MATERIALS AND METHODS 93

5.2.1 Cell culture *93*

5.2.2 Cell irradiation *93*

5.2.3 Cell lysate preparation *93*

5.2.4 SDS-PAGE & Western Blot *94*

5.2.5 Flow cytometry *94*

5.2.6 Immunofluorescence microscopy *95*

5.2.7 Bioconjugation of DTPA-D25E5-TAT by EDC/NHS crosslinking *96*

5.2.8 Bioconjugation of DTPA-D25E5-TAT by SPAAC-based click chemistry *97*

5.2.9 Radiolabelling DTPA-D25E5-TAT with $^{111}InCl_3$ *97*

5.2.10 In vitro uptake of ^{111}In-DTPA-D25E5-TAT *98*

5.2.11 In vitro retention of ^{111}In-DTPA-D25E5-TAT *98*

5.2.12 Statistical analysis *99*

5.3 RESULTS 99

5.3.1 Validation of pATM phosphorylation kinetics *99*

5.3.2 Evaluation and selection of anti-pATM monoclonal antibodies *101*

Evaluation of ^{111}In-DTPA-D25E5-TAT uptake and retention in vitro *103*

DISCUSSION 104

CHAPTER 6 – DISCUSSION AND FUTURE WORK 108

6.1 CONCLUSION AND FUTURE DIRECTIONS 108

6.1.1 General aims *108*

6.1.2 H2B-EGFP / GFP-G1 model system *109*

6.1.3 Imaging alternative cellular compartments *110*

6.1.4 Conjugation strategies *111*

6.1.5 Cell penetrating peptide optimisation *112*

6.1.8 Closing remarks: The end of the beginning *117*

BIBLIOGRAPHY 118

APPENDIX 144

List of figures

Chapter 1 – General introduction

Figure 1.1 Basic overview of nuclear imaging using PET/SPECT…….5

Figure 1.2 Nuclear imaging of the Hallmarks of Cancer……...…….7

Figure 1.3 Annotated structure of an IgG molecule……...…....9

Figure 1.4 Examples and comparison of different antibody fragments.……14

Figure 1.5 Conjugation strategies used for the development of antibody-drug conjugates.....15

Figure 1.6 CPP internalisation by energy independent direct penetration.……23

Figure 1.7) Endocytic mechanisms of CPP internalisation.……..25

Chapter 2 - Development of GFP-based model system

Figure 2.1 Vector map of plasmid H2B-GFP.……...45

Figure 2.2 Transient expression of H2B-EGFP in H1299 cells ...…….46

Figure 2.3 Stable transfection and selection of H1299 cells with H2B-EGFP.……..47

Figure 2.4 Selection of H2B-EGFP expressing clones.…….48

Figure 2.5 Validation of stable H2B-EGFP expression in H1299 clones.…….49

Figure 2.6 Stability of H2B-EGFP expression in selected clone cell lines.……...50

Figure 2.7 Validation of monoclonal antibody GFP-G1……..51

Figure 2.8 Flow cytometry-based affinity binding assay of antibody GFP-G1……52

Chapter 3) ***Novel conjugation of IgG-TAT radioimmunoconjugates***

Figure 3.1) Non-site-specific labelling of IgG molecules with DTPA and CPP TAT……..57

Figure 3.2) Initial optimisation of DBCO-N3 based click conjugation.……65

Figure 3.3) Conjugation competition assay……..66

Figure 3.4) Radiolabelling purity and stability of ^{111}In-DTPA-GFP-G1-TAT RICs.……..68

Figure 3.5) Radioimmunoassay blocking comparison of GFP-G1 based RICs.……69

Figure 3.6) Colony formation assay demonstrating the effect of ^{111}In-GFP-G1-TAT uptake on cell viability.…….…….70

Figure 3.7) Comparison of uptake of ^{111}In-DTPA-GFP-G1-TAT prepared by different TAT conjugation methods..……71

Chapter 4) ***Investigating the limits of antibody-based intranuclear PET/SPECT imaging***

Figure 4.1) Conjugation and in vitro evaluation of ^{111}In-GFP-G1-TAT uptake..……81

Figure 4.2) Ex vivo biodistribution and tumour uptake of ^{111}In-DTPA-GFP-G1-TAT.……..83

Figure 4.3) Imaging of ^{111}In-DTPA-GFP-G1-TAT *in vivo*.……84

Figure 4.4) Image quantification of ^{111}In-DTPA-GFP-G1-TAT biodistribution *in vivo*.....85

Chapter 5) ***Imaging phospho-ATM using antibody-based PET/SPECT imaging***

Chapter 5) Imaging phospho-ATM using antibody-based PET/SPECT imaging

Figure 5.1) Activation and functions of protein kinase ATM within the DNA damage response…….91

Figure 5.2) Validation of shRNA mediated knockdown of ATM and evaluation of ATM activation kinetics……..……..100

Figure 5.4) Flow cytometry-based affinity binding assay of monoclonal antibody D25E5…101

Figure 5.3) Validation of monoclonal antibody D25E5……..102

Figure 5.5) In vitro uptake assay of ^{111}In-DTPA-D25E5-TAT…….103

Figure 5.6) In vitro retention assay of ^{111}In-DTPA-D25E5-TAT……..104

List of tables

Table 1.1) Commonly used radioisotopes for PET/SPECT imaging..……..8

Table A.1) Antibody reference table.……..143

Acknowledgements

First and foremost, I would like to thank Prof Bart Cornelissen for taking me into his laboratory. His ongoing encouragement and support throughout this project has been the best I could have hoped for when we set out on this project back in 2016 (remember those days?). I imagine that from a supervisor's perspective, taking on a DPhil student is a somewhat large leap of faith. I hope that I have repaid this trust placed in me.

I would also like to extend my thanks to the rest of the members of team RADiobiology (the Cornelissen lab group). It has been a pleasure working with all of you, sharing the occasional sporadic laugh interspersed with the torrent to failed experiments and other lab related mishaps. I'd like to especially thank Sam, Julia and Debs (plus Shreeves), for always helping me find a wry smile when all seemed to be going awry (I owe all of you several drinks). Another major thanks must go to Mike and Gemma for their help at some of the most crucial points of my project, may you always remain "fair to middling".

Throughout my time at Oxford, Lincoln College has always been a home away from home, enriching my experience as a DPhil student. Beginning with a warm welcome when I first came to Oxford and continuing to support my endeavours, both academic and non-academic, throughout my time at this weird and wonderful University.

Carrying out a DPhil is very rarely fun and games, however, I must send thanks to all the friends I have met along the way who have made my experience considerably brighter. In particular, a big thanks to Alice, Chris and Megan, for showing me that it's perfectly normal for experiments not to work, most of the time.

I don't think I could write this section without a special mention for the guys and girls at Oxford University Cycling Club (OUCC). I have spent hundreds, if not thousands, of hours out on the road with you, usually with some truly appalling chat about what chain lube we're using. From

the highs of the Passo dello Stelvio in July to the lows of Abingdon in February, I have loved every second of it. I hope one day we will win Varsity again.

It goes without saying that without the unconditional love and support of my family I would not be here today. Your faith in me has often been strained but has never been in doubt, and I will always appreciate the sacrifices you have made to give me the freedom to pursuit my (often misguided) dreams and projects. You are all uniquely inspirational and I will forever try to hold myself to the same standards that you do, one day I'll get there.

Finally, I'd like to reserve my biggest thanks to my quarantine (and actual) partner Kinga. Completing my DPhil in these turbulent times was made possible by your unrelenting love and support. Having lived in near isolation with me over the last 9 months, I know that your patience has been tested far more rigorously than mine. May we look forward with excitement to what our next big project brings (maybe a cat).

Abstract

PET and SPECT imaging of intranuclear epitopes using antibodies (IgG) tagged to cell penetrating peptides (CPPs), such as TAT (GRKKRRQRRRPPQGYG) has great potential given the versatility, specificity and sensitivity typical of antibodies. However, this process is technically challenging because of the location of the target. Previous research has demonstrated a variety of intranuclear epitopes that can be targeted with TAT-IgG-based radioimmunoconjugates (RICs). In this thesis, I set out to determine the technical limitations of intranuclear PET/SPECT using IgG-TAT-based RICs, notably the lower target abundance detection threshold.

I stably transfected the lung adenocarcinoma cell line H1299 with an enhanced green fluorescent protein (EGFP)-tagged histone protein (H2B-EGFP) and generated four cell lines expressing increasing levels H2B-EGFP. EGFP levels were quantified using western blot, flow cytometry, and ELISA (0 - 1 Mcopies/cell, including H1299 WT cells). In parallel, a murine anti-GFP monoclonal antibody was produced, purified and validated for selective binding to H2B-EGFP.

Having established a model system for interrogating the limits IgG-TAT RICs, I developed a novel conjugation strategy to label antibodies with azide modified derivatives of the CCP TAT (TAT-N_3) and chelator DTPA (N_3-Bn-DTPA) using strain-promoted alkyne-azide cycloaddition (SPAAC) click chemistry. This method of conjugation, referred to as the DBCO-N_3 method, was optimised and followed by radiolabeling with ^{111}In (^{111}In-DTPA-GFP-G1-TAT) prior to *in vitro* comparison with the conventional method of IgG-TAT RIC conjugation (EDC-NHS crosslinking), using the H2B-EGFP / GFP-G1 model system.

With this new conjugation strategy in place, the cellular uptake of ^{111}In -DTPA-GFP-G1-TAT across the H2B-EGFP transfected clones was evaluated to determine the lower abundance

detection threshold *in vitro*. Using the same model, tumour uptake in xenograft-bearing mice was quantified to determine the smallest amount of target epitope that could be detected using ^{111}In-DTPA-GFP-G1-TAT *in vivo*.

Finally, I attempted to apply IgG-TAT RICs to a practical application by imaging the DNA damage response (DDR) by targeting the serine/threonine protein kinase ataxia telangiectasia mutated (ATM), an apical regulator of the cellular response to DNA double strand breaks (DSBs).

Here, I present a proof-of-concept demonstration of what is currently possible with RIgG-TAT based RICs whilst simultaneously providing a platform for further exploration and optimisation of this technology, potentially yielding a new generation of more potent whole-body immuno-imaging devices.

Abbreviations

53BP1 - Tumour suppressor p53-binding protein 1

Ab - Antibody

ADC - Antibody drug conjugate

AE - Auger electron

AHA - Azidohomoalanine

ANTp - Antennapedia homeodomain protein-derived peptide

ATM - Ataxia telangiectasia mutated

ATR - Ataxia telangiectasia and Rad3 related protein

CAR - Conjugate to antibody ratio

cCPE - C terminus of Clostridium perfringens enterotoxin

CHK2 - Checkpoint kinase 2

CHO - Chinese hamster ovary

CME - clathrin-mediated endocytosis

CPP - Cell penetrating peptide

CT - Computerised tomography

CvME - caveolae-mediated endocytosis

CXCR4 - C-X-C chemokine receptor type 4

DAPI - 4',6-diamidino-2-phenylindole

DBCO - Dibenzocyclooctyne

DDR - DNA damage response

DFO - Deferoxamine

DMSO - Dimethyl sulfoxide

DNA - Deoxyribonucleic acid

DNA-PK - DNA-dependant protein kinase

DSB - Double strand break

DTPA - Diethylenetriaminepentaacetic acid

ECL - Enhanced chemiluminescence

EDC - 1-ethyl-3-(3-dimethylaminopropyl) carbodiimide

EDTA - Ethylenediaminetetraacetic acid

EGF - Epidermal growth factor

EGFP - Enhanced green fluorescent protein

EGFR - Epidermal growth factor receptor

ELISA - Enzyme linked immunosorbent assay

EPR - Enhanced permeability and retention

F-MISO - Fluoromisonidazole

F(Ab) - Fragment antigen binding

Fc - Fragment crystallisable

FDG - Fluorodeoxyglucose

FGF 12 - Fibroblast growth factor 12

GFP - Green fluorescent protein

GPCR - G coupled protein receptor

GPI-AP - Glycosylphosphatidylinositol-anchored protein

GST - Glutathione S-transferase

GTP - Guanosine triphosphate

H2AX - H2A histone family member X

H2B - Histone protein 2B

HER2 - Human epidermal growth factor 2

HIV-1 - Human immunodeficiency virus 1

HRP - Horseradish peroxidase

HSPG - Heparan sulphate proteoglycans

hTERT-ANON - Telomerase reverse transcriptase antisense oligonucleotide

i.v. - Intravenous

IARC - International Agency for Research

IBA - Indole-3-butyric acid

ID/g - Injected dose per gram

IgG - Immunoglobulin G

iTLC - Instant thin layer chromatography

K_D - Dissociation constant

KAP1 – KRAB-associated protein 1

KRAS - Kirsten rat sarcoma viral oncogene homologue

mAb - Monoclonal antibody

MDC - Monodansylcadaverine

MDC1 - Mediator of DNA damage checkpoint protein 1

MDM2 - Mouse double minute 2 homolog

MES - 2-(N-morpholino)ethanesulfonic acid

MIgG - Mouse immunoglobulin G

MRE11 - Double-strand break repair protein MRE11

MRI - Magnetic resonance imaging

mRNA - Messenger RNA

MYC - MYC proto-oncogene

N_3 - Azide

NaOH - Sodium hydroxide

NBS - Nucleotide binding site

NBS1 - Nibrin

NHS - *N*-hydroxysuccinimide

NLS - Nuclear localisation sequence

NRP1 - Neuropilin-1

p-TEFb - Positive transcription elongation factor

$p21^{WAF1/Cip1}$ - Cyclin-dependent kinase inhibitor 1

$p27^{Kip1}$ - Cyclin-dependent kinase inhibitor 1B

p53 - Tumour protein P53

pAb - Polyclonal antibody

PARP - Poly (ADP-ribose) polymerase

PBS - Phosphate buffered saline

PDGF - Platelet derived growth factor

PET - Positron emission tomography

PFA - Paraformaldehyde

PSMA - Prostate specific membrane antigen

PTD - Protein transduction domain

PVDF - Polyvinylidene fluoride

R_{12} - Dodeca-arginine

R_8 - Octa-arginine

R_9 - Nona-arginine

Rac1 - Ras-related C3 botulinum toxin substrate 1

RAD50 - DNA repair protein RAD50

RIA - Radioimmunoassay

RIC - Radioimmunoconjugate

RIgG - Rabbit immunoglobulin

RIPA - Radioimmunoprecipitation

RIT - Radioimmunotherapy

ROI - Region of interest

ScFv - Single-chain variable fragment

SCN - Isothiocyanate

SD - Standard deviation

siRNA - Small interfering RNA

SPAAC - Strain-promoted azide-alkyne cycloaddition

SPECT - Single photon emission computerised tomography

STP – 4-Sulfo-2,3,5,6-tetrafluorophenyl

TAT - Cell penetrating peptide trans-activator of transcription

TAT-AHA - TAT-azidohomoalanine

Tat - HIV-1 protein transactivator of transcription

TRE - Transactivator response element

Tris - 2-Amino-2-(hydroxymethyl)pro-pane-1,3- diol

US - Ultrasound

US FDA - United States Food and Drug Administration

Chapter 1

General Introduction

1.1 Cancer and molecular imaging

1.1.1 What is cancer?

The term cancer is used to describe a broad range of medical conditions, typically characterised by abnormal cell proliferation. This proliferation of cells results in the formation of a tumour, which damages or even invades surrounding tissues, eventually spreading around the body (metastasis), culminating in the aberrant or complete loss of function of vital systems and ultimately death. Cancer is the second leading cause of death globally, with an estimated 19 million new cases of cancer and 9.5 million deaths reported by the International Agency for Research on Cancer in 2020 (Wild et al., 2020). Furthermore, the projected burden of cancer on the world population is set to rise disproportionately, with 27.5 million new cases and 16.3 million deaths projected in 2040. Although this rise can in part be attributed to aging populations in developed nations, it is also important to account for the growing prevalence of lifestyle factors associated with increased cancer risk, such as diet and reduced physical activity, in economically developing nations.

Given the sheer diversity of neoplastic diseases, it is important to determine characteristics that unify cancer as a means of developing and implementing effective clinical strategies. The first unifying concepts of the molecular biological basis of cancer are the presence of *oncogenes*

and *tumour suppressor genes* which promote and supress tumour cell proliferation, respectively (Croce, 2008, Sherr, 2004). A major refinement of these concepts came in 2000 with the seminal paper on the *hallmarks of cancer*, where authors Hanahan and Weinberg set out a classification of the phenotypes of cancer into six distinct characteristics; 1) self-sufficiency in growth signals, 2) insensitivity to growth supressing signals, 3) resisting cell death, 4) replicative immortality, 5) invasion and metastasis and 6) induction of angiogenesis (Hanahan and Weinberg, 2000). In an update released in 2011, four additional 'hallmarks' were added, including 7) immune system evasion, 8) deregulation of cellular metabolism, 9) increased genomic stability and finally 10) promotion of inflammation (Hanahan and Weinberg, 2011). In turn, research into understanding the mechanisms that drive tumourigenesis are focused on the understanding the biomolecular pathways that regulate these processes.

1.1.2 Molecular imaging and cancer

Clinical imaging is a fundamental cornerstone of the diagnosis and treatment of cancer, with a variety of different methods such as computerised tomography (CT), magnetic resonance imaging (MRI), ultrasound (US), single-photon emission computed tomography (SPECT) and position emission tomography (PET). Molecular imaging can be broadly defined as the non-invasive, real-time visualisation of biochemical features/processes at the molecular level, which is scalable from individual cells to tissues and even whole intact organisms (James and Gambhir, 2012). In practise, molecular imaging works through the use of molecularly targeted vectors, such as antibodies, peptide fragments and small molecule inhibitors, in combination with a detectable signal moiety, such as a gamma-emitting nuclide or fluorophore, allowing the observation of abundance of the targeted agent in tissues of interest.

The ever-increasing complexity revealed by molecular biology along with the implementation of highly specialised precision therapeutics in oncology has created a demand for complementary molecular imaging modalities for both clinical and preclinical applications, such as biomarker detection, drug discovery and real-time therapy evaluation. Subsequently the field of molecular imaging is rapidly expanding, utilising a range of different imaging techniques, such as functional MRI, bioluminescence, and molecular PET/SPECT imaging.

1.1.3 Advantages of molecular imaging over conventional diagnostic tools

Cancer drug development is one of the most active areas of research in all of clinical research, with more clinical trials than any other field of medicine (Informa, 2020). However, the clinical impact of this new wave of therapeutics has often been underwhelming, especially true in cases where patient stratification has not occurred (Tibau et al., 2018). One of the major challenges facing modern oncology is the ability to identify and harness predictive biomarkers to pinpoint the optimum therapy for a particular patient (Jaffee et al., 2017).

Conventional imaging modalities, such as CT, MRI and US have become reliable mainstays of clinical oncology. However, these techniques are often limited to giving a clinician basic morphological information, such as the size and location of a tumour. In order to utilise the rapid expansion of knowledge surrounding the pathophysiology of cancer at the subcellular level, more relevant diagnostic readouts at the biomolecular level are required. Although more comprehensive molecular characterisation is possible without molecular imaging, such as determining expression levels of a particular marker from a biopsy sample, these diagnostics often require highly invasive removal of tissue (Wolff et al., 2018). In addition, by only being able to sample a small, excised section of tissue from a single tumour lesion, standard biopsy techniques are unable to account for the phenotypic/genotypic heterogeneity of a cancer, both intratumourally, and between multiple lesions within the same patient. Alternative, minimally

invasive biomarker evaluation techniques, such as liquid biopsies are currently under development, but these techniques are unable to characterise single specific lesions and also may be unable to effectively account for tumour heterogeneity.

Molecular imaging has the potential to overcome these challenges by using minimally invasive imaging probes to functionally characterise tumours at the molecular level on a whole-body scale, thereby giving the pathophysiological detail of a biopsy on the scale of a conventional imaging modality, in a non-invasive manner.

1.1.4 Basic Principles and Impact of PET/SPECT imaging

Although a plethora of molecular imaging modalities are in different stages of development, such as fluorescent, photoacoustic and Raman spectroscopy imaging, the majority of molecular imaging in the clinic is carried out using radioactive imaging probes, known as nuclear medicine imaging (Garousi et al., 2020). In particular, PET and SPECT imaging, which image the emissions of positron- and gamma-emitting radionuclides, respectively, have shown great promise as extremely sensitive and versatile imaging modalities. In essence, PET and SPECT imaging are similar in that they both utilise a radioactive isotope, such as Fluorine-18 (^{18}F) or Indium-111 (^{111}In), either unbound, or bound to a targeted imaging vector (**Figure 1.1**) (Weber et al., 2020). Once administered, the targeted portion of the vector then interacts with the relevant biological target, resulting in an accumulation of the probe, and therefore the isotope in the tissue or organs where the target is present, creating a contrast that can be visualised and quantified using a PET or SPECT camera. The fundamental difference between the two modalities is the choice of radioisotope and subsequent type of radiation detected for imaging (**Table 1.1** (Conti and Eriksson, 2016)**)**. PET cameras detect gamma rays that result from the annihilation of a positron from a positron emitting isotope, such as Copper-64 (^{64}Cu). Whereas

SPECT cameras detect gamma rays produced directly by gamma emitting radioisotopes, including ^{111}In.

The origins of SPECT imaging can be traced back to the mid twentieth century with the invention of the gamma camera and basic stationary tomographic scanners in the 1960s (Hutton, 2014). However, it was not until 1976 that the first general purpose SPECT scanner was available to the clinic, developed by John Keyes (Keyes et al., 1977). Although both PET and SPECT have great potential for imaging modalities, PET has become more popular for clinical use, with several advantages over SPECT, such as better spatial resolution, sensitivity and greater capacity for quantification (Wernick and Aarsvold, 2004). One of the most well-established clinical applications of PET imaging is FDG-PET, which uses the ^{18}F glucose derivative, 2-deoxy-2-^{18}F-fluoro-D-glucose (^{18}F-FDG), to image the increased uptake of

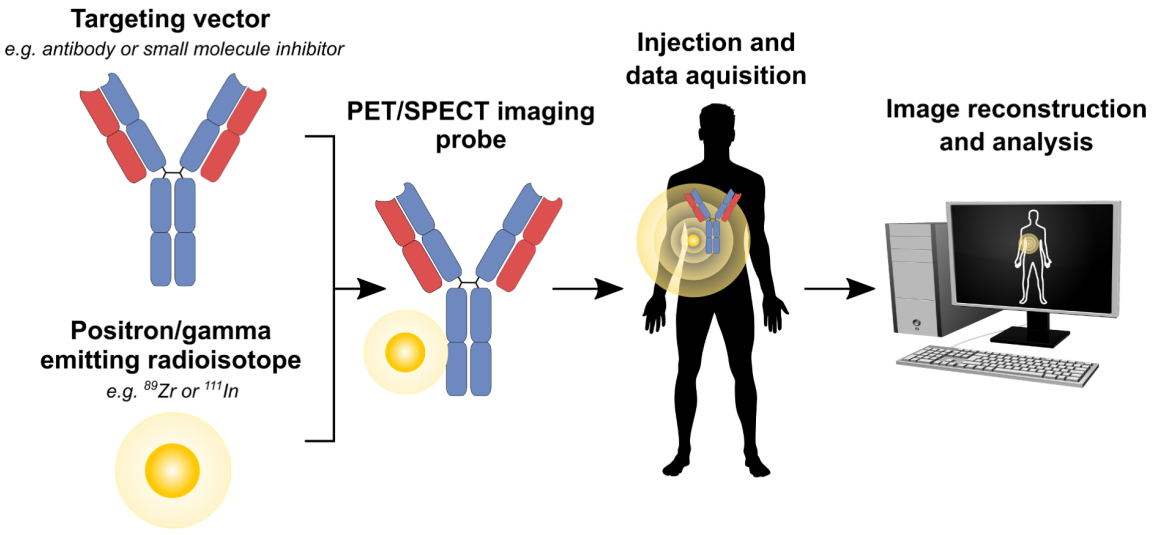


Figure 1.1) Basic overview of nuclear imaging using PET/SPECT. A targeted vector, such as an antibody or small molecule inhibitor is radiolabelled with a positron or gamma radiation emitting radioisotope to produce a PET/SPECT imaging probe. The targeted imaging probe is then administered to the subject where it engages with the target of interest. Gamma radiation is detected using a PET or SPECT camera, often in conjunction with computerised tomography (CT). A spatial distribution of the radiotracer is determined by reconstruction of the emission detection data acquired by the PET or SPECT camera.

glucose, typical of many cancerous tissues. This increase in glucose uptake is a consequence of metabolic deregulation of many types of cancer that promote glycolysis as the primary method of energy production, also known as the Warburg effect (Liberti and Locasale, 2016). This application of PET has become a well-established tool for various procedures in oncology, including tumour staging and treatment evaluation (Gallamini et al., 2014).

PET/SPECT imaging, however, is not just limited to FDG-PET, through the design of novel radioactive tracers, PET imaging has been used to visualise a large and diverse range tumour characteristics, including the majority of the "Hallmarks of Cancer" (**Figure 1.2**), with over 4,000 different PET probes listed on The Radiosynthesis Database of PET Probes (RaDaP) (Alam et al., 2015, Petroni et al., 2020). At the time of writing, the ClinicalTrials.gov database included 3,467 and 231 clinical trials involving the use of PET and SPECT in cancer treatment respectively, indicating a strong future for nuclear imaging (US National Library of Medicine, 2020).

PET radioisotopes

Radionuclide	^{11}C	^{13}N	^{15}O	^{18}F	^{64}Cu	^{68}Ga	^{82}Rb	^{89}Zr	^{86}Y
Energy (keV)*	386	492	735	250	278	890	1535†	396	535†
$T_{1/2}$	20.4 min	10.0 min	2.0 min	109.8 min	13 h	67.6 min	1.3 min	78 h	14.7 h

SPECT radioisotopes

Radionuclide	^{67}Ga	^{67}Cu	^{99m}Tc	^{111}In	^{123}I	^{153}Sm	^{159}Gd	^{166}Ho	^{177}Lu
Energy (keV)	93	185	140	245	159	103	363	80	208
$T_{1/2}$	78.3 h	61.8 h	6.0 min	67.2 h	13.2 h	46.3 h	18.5 h	26.8 h	159.5 h

Table 1.1) Commonly used radioisotopes for PET/SPECT imaging. Energies given a mean value. (*) For PET isotopes, the energy of the positron emission is given. For positron-emitting isotopes with more than one β^+ decay (†), the energy given is for the emission with the largest branching ratio (Conti and Eriksson, 2016).

1.1.5 Benefits and drawbacks of PET/SPECT imaging

In comparison to other conventional imaging modalities, and even other molecular imaging methods, PET/SPECT imaging enjoys the powerful combination of unparalleled sensitivity and near limitless depth of penetration. Unlike, for instance MRI, PET and SPECT are both capable of detection of tracers in sub-nanomolar quantities (10^{-11} and 10^{-12} M respectively), which gives PET and SPECT imaging several indispensable advantages. Firstly, high sensitivities allow the visualisation of biomolecular abnormalities at very low quantities, making diagnostic tests feasible at earlier timepoints. Furthermore, the high sensitivity of PET and SPECT imaging allows for the use of significantly less imaging tracer, thereby reducing the opportunity for the imaging probe to have an influence on the function of the target and significantly reducing probe toxicity. The relatively high sensitivities of PET and SPECT imaging may also allow for potentially reduced acquisition times, in contrast with MRI, which could be critical when imaging short lived biological phenomena (James and Gambhir, 2012). In addition to sensitivity, PET and SPECT imaging offers a high degree of versatility, with a variety of molecular probes and available isotopes in both pre-clinical and clinical development (**Figure 1.2**). For instance, small molecule compounds with incorporated radioisotopes have been used for imaging tumour hypoxia using ^{18}F-fluoromisonidazole (^{18}F-FMISO), and expression levels of poly(ADP ribose) polymerase (PARP) using ^{18}F-olaparib (Wilson et al., 2019). The use of small molecule imaging agents can be limited by what is achievable through chemical synthesis methodology. In contrast, given the availability of a large variety of highly selective antibodies, with excellent binding affinity, antibody-based imaging with RICs has the potential to offer an even broader range of imaging possible targets.

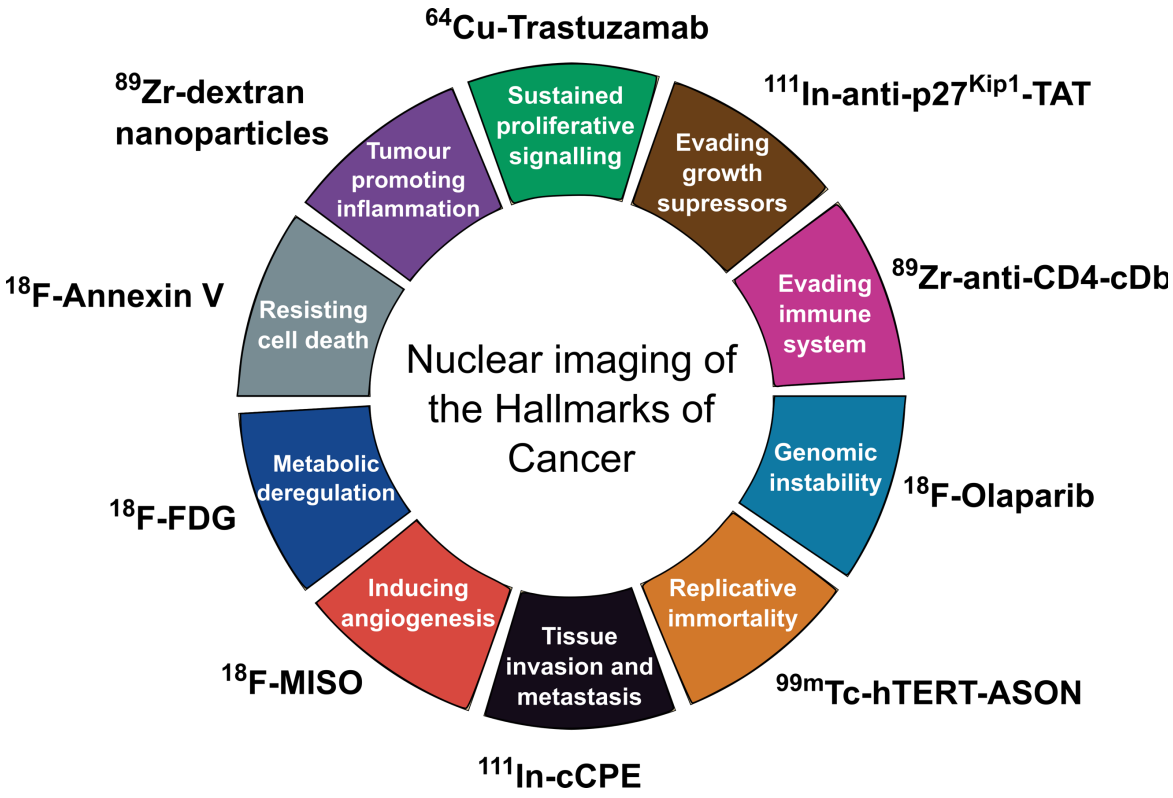


Figure 1.2) Nuclear imaging of the *Hallmarks of Cancer*. One of the greatest assets of molecular imaging using PET/SPECT imaging is versatility. By combining targeted vectors with radioactive isotopes, PET and or SPECT imaging has been successfully used to image aspects of all of the *hallmarks of cancer*. Adapted from Alam et al., 2015.

One of the major drawbacks of nuclear imaging is the requirement for ionising radiation, which has several implications. Firstly, there is a limitation on the number of imaging sessions a patient can undergo before accumulating a potentially harmful dose of radiation. Another, albeit practical, consideration for PET and SPECT imaging in particular is reliable access to radioisotopes for imaging, this is especially the case for short lived isotopes, such as ^{18}F ($t_{½}$ = 1.83 hours) or technitium-99m (^{99m}Tc) ($t_{½}$ = 6.01 hours), such isotopes require short and efficient supply chains in order to prevent detrimental losses in radioactivity. The final key disadvantage of PET and SPECT imaging is that they are costly techniques, requiring advanced equipment with extensive running costs and highly skilled operators. For the year 2018/19, the

average cost of a FDG-PET scan cost the UK National Health Service (NHS) between 549 and 776 GBP, in comparison to 40 GBP for histopathology and histology testing (NHS, 2020). However, the information gained from molecular PET imaging could be used to make strategic decisions that could not only improve patient outcome and quality of life, but also be cost effective, for instance avoiding unnecessary and costly surgeries (Smith et al., 2017a).

1.2 Antibody Based Nuclear Imaging

1.2.1 Introduction to monoclonal antibodies

An antibody (Ab), also known as an immunoglobulin (Ig) is a relatively large (~150 kDa), Y-shaped glycoprotein that binds to a specific target molecule, also known as an antigen or epitope (**Figure 1.3**). Antibodies are produced and secreted by B lymphocytes, which form part of the adaptive immune system (Alberts et al., 2008). In most mammals, antibodies are comprised of four polypeptide chains, two pairs of identical heavy (50 kDa) and light chains (25 kDa), connected by a series of disulphide bonds. Antibodies are classified into five different isotypes (IgA, IgD, IgE, IgG and IgM), according to which variety of heavy chain the antibody features. However, the isotype which is predominantly used for research and clinical practice is IgG (Beers et al., 2016). Antibody molecules feature three functional domains. Two fragment antigen binding domains (Fabs), which are responsible for target engagement, and a single fragment crystallisable (Fc) domain, which interacts with the host immune system.

Monoclonal antibodies (mAbs) are antibodies produced by identical immune cells that have been generated from the same parental cell line, subsequently each individual IgG molecule is also identical and is targeted towards a specific antigen. Given that mAbs can be generated to target an expansive variety of epitopes with predictable and reproduceable binding properties, it is no surprise that they have become an indispensable tool in both preclinical biomedical

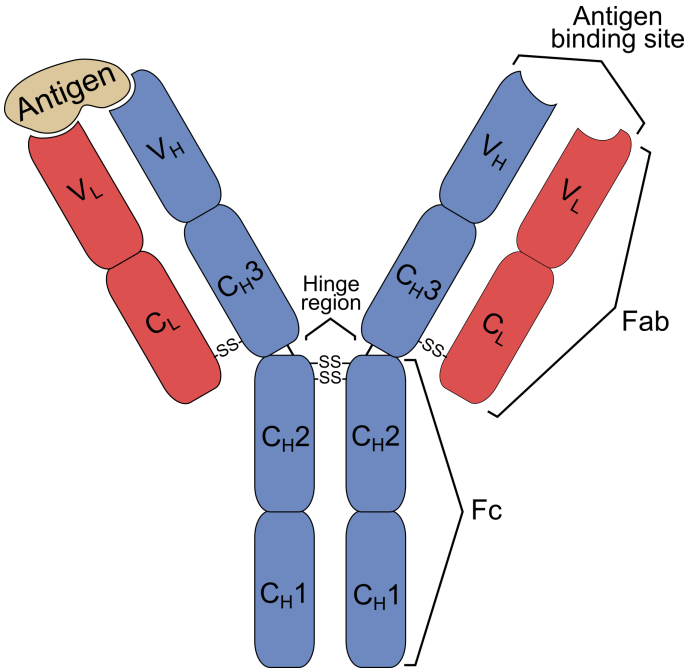


Figure 1.3) Annotated structure of an IgG molecule. The IgG molecule consists of four polypeptide chains featuring two identical pairs of heavy chains (~50 kDa, blue) and light chains (~25 kDa, red), arranged as a dimer of dimers linked together by disulphide bonds. The complete IgG molecule can be divided into three regions, one fragment crystallisable (Fc) region and two fragment antigen binding (Fab) regions.

research and clinical practise, diagnosing and treating a variety of diseases including cancer, rheumatoid arthritis and psoriasis (Beck et al., 2017).

The ability to produce sufficient quantities of mAbs for experimental and clinical use was made possible through the process of hybridisation, pioneered by Köhler and Milstein in 1975 (Kohler and Milstein, 1975). With highly reliable, sensitive and specific binding characteristics, mAbs very quickly became powerful tools for research, forming the basis of a variety of now essential techniques, including immunoblotting, flow cytometry and enzyme-linked immunosorbent assay (ELISA).

The concept that antibodies could be utilised for clinical benefit was first described as early as 1900, where they were labelled as ‘magic bullets’ by the German Nobel laureate Paul Ehrlich

(Strebhardt and Ullrich, 2008). Despite clear potential, mAbs initially yielded modest success as therapeutic agents in the clinic. One major drawback was the application of murine mAbs in humans, which instigated a host response against the antibody itself, along with rapid blood clearance and limited interaction with the effector arms of the host immune system (Green et al., 1994). A significant breakthrough came with the genetic modification of murine mAbs to produce chimeric human-mouse mAbs, which effectively bypassed many of the issues associated with previous iterations (Carter, 2001). Since the approval of the first anti-cancer chimeric mAb Rituximab in 1997 by the United Stated Food and Drug Administration (US FDA), mAbs have revolutionised anti-cancer drug design and treatment in the clinic. At the time of writing, 90 therapeutic mAbs have been approved by the US FDA, and mAbs accounted for seven of the ten top selling drugs in 2019, of which five were anti-cancer therapeutics (Maloney et al., 1997, Urquhart, 2020).

1.2.2 Antibody-based molecular imaging

In addition to direct therapeutic use, mAbs also have great potential for the basis of molecular imaging probes. As with most molecular imaging probes, antibody-based imaging probes involve the combination a detectable signal agent, such as a gamma-emitting radionuclide or fluorophore to a targeted vector, in this case an antibody or antibody fragment (Dammes and Peer, 2020).

Monoclonal antibody-based imaging probes provide several advantages over other conventional imaging probes. Firstly, antibodies are capable of engaging targets at picomolar concentrations, which is ideal when trying to minimise radioactive dose (Hamid et al., 2013). Furthermore, the specificity of antibodies is generally considered to be superior to other molecularly targeted approaches, such as small molecule inhibitors (Huang et al., 2004). This

is vital in molecular imaging where high-fidelity binding is required for reliable characterisation an epitope of interest.

Another feature of mAbs is their relatively large molecular weight and size (~150 kDa, 20 nm), which has several associated benefits and drawbacks. Firstly, at the cellular level the size and hydrophilicity of monoclonal antibodies renders them unable to efficiently bypass cellular membranes, limiting their range of applications to extracellular targets. At the organismal level, the size of antibodies results in poor tissue penetration relative to small molecule inhibitors when imaging solid tumours (Li et al., 2016). Furthermore, the size of antibodies is too large for rapid renal clearance, greatly enhancing blood plasma half-life (c. 2-3 weeks) (Vieira and Rajewsky, 1988). Whilst high blood plasma persistence is advantageous for therapeutics when maximising concentration in target tissues over a long period of time, this is disadvantageous when imaging as it both increases radiation burden to non-targeted tissues and reduces image contrast at earlier timepoints (Carter et al., 2018). Despite these drawbacks, the size of mAbs does present a major opportunity for conjugation of a range of additional functional groups without compromising target affinity. This allows the researcher, or clinician, to effectively tailor the characteristics of a mAb for a variety of different tasks, such as the addition of cytotoxic payloads, or alternative radionuclides for targeted radionuclide therapy (Dammes and Peer, 2020).

1.2.3 Molecular imaging using antibody fragments

In addition to whole antibodies, a large variety of antibody-based fragments and engineered forms have been explored for the purposes of molecular imaging probes, altering the molecular weight and valency of the imaging vector (Freise and Wu, 2015). Antibody-based fragments can vary largely in size, from bivalent $F(ab')_2$ antigen binding fragments (~110 kDa), to affibodies (7 kDa) (**Figure 1.4**). The size of the antibody-based fragment can significantly

affect the pharmacokinetics of the imaging probe. This is primarily a result of alternative clearance pathways as proteins that are larger than 60 kDa are removed from circulation by the relatively slow hepatic clearance pathway, whereby smaller fragments are removed via the faster renal clearance pathway. The increased serum half-life of larger antibodies or antibody-fragments results in higher tissue concentrations, making them better suited to ensuring interaction with low abundance targets. Whilst beneficial in some cases, higher tissue concentrations also result in greater non-specific uptake, potentially compromising signal-to-noise ratios of acquired images at earlier time points, in comparison to smaller fragments. In a side-by-side comparison using a Zirconium-89 (^{89}Zr) radiolabelled prostate specific membrane antigen (PSMA) targeted minibody (80 kDa) and cys-diabody (50 kDa), using quantitative PET image analysis in conjunction with a PSMA expressing *in vivo* xenograft model, the ^{89}Zr-cys-diabody yielded a tumour to heart (blood) ratio 24 hours post injection almost two fold higher than the minibody equivalent (Viola-Villegas et al., 2014).

Another important consideration with antibody fragment selection is the presence of the fragment crystallisable (Fc) region. Where the Fragment antigen binding (FAb) regions is required for epitope engagement, the Fc region of an antibody is responsible for interaction with proteins of the complement system, as well as effector cells of the immune system, such as dendritic or natural killer cells, via the Fc receptor (Park et al., 2016). Where interaction with the host immune system can potentially be advantageous for antibody-based therapeutics, it is generally preferable that molecular imaging probes are biologically inert to avoid perturbing the system under examination. An additional consequence of the presence of an Fc region is enhanced serum half-life and therefore tissue concentration through neonatal Fc receptor (FcRn) mediated recycling (Pyzik et al., 2015). Lutje et al. demonstrated this using ^{111}In labelled whole antibodies (150 kDa, Fc region present) and F(ab')$_2$ fragments (110 kDa, Fc region absent) targeted against PSMA. Despite both probes being large enough to avoid

rapid renal clearance, the Fc region containing full antibody reached a peak tumour to blood ratio after 168 h, whereas the Fc region lacing $F(ab')_2$, reached this peak after only 24 h (Lutje et al., 2015).

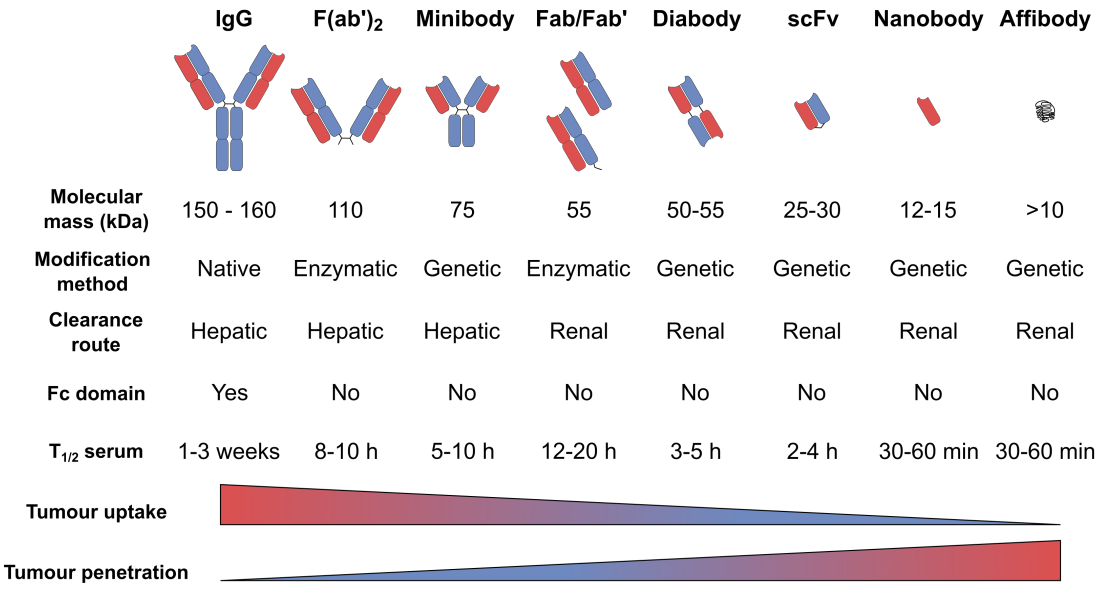


Figure 1.4) Examples and comparison of different antibody fragments. Antibody fragments can be engineered into a broad range targeted probes, each with specific characteristics that are optimal for different applications. Adapted from Freise and Wu 2015.

1.4 Antibody conjugation strategies

1.4.1 Overview of antibody conjugation strategies

Unmodified monoclonal antibodies already represent an incredibly powerful tool for both researchers and clinicians. However, to fully exploit the benefits of monoclonal antibody technology, a large amount of research is now being directed towards the modification of antibodies with additional functional groups to produce novel classes of therapeutics, such as antibody drag conjugates (ADCs) or RICs. Subsequently, this field of research is rapidly

expanding with more than sixty ADCs currently in clinical trials (Khongorzul et al., 2020). The ability to consistently modify antibodies with one, or more functional groups is dependent on a reliable conjugation strategy, which has itself become a burgeoning area of research, with a diverse range of conjugation strategies now available or in development.

With the broad selection of conjugation techniques now available, each with a unique set of benefits and drawbacks, it is more convenient than ever to find a strategy suited for a particular application (**Figure 1.5**). Antibody conjugation strategies can be classified in several different ways, such as site specificity. One method of classification divides strategies into methods that modify naturally occurring moieties and methods that require genetic modification of the antibody, which is an important consideration if the operator does not have the means to genetically modify the antibody.

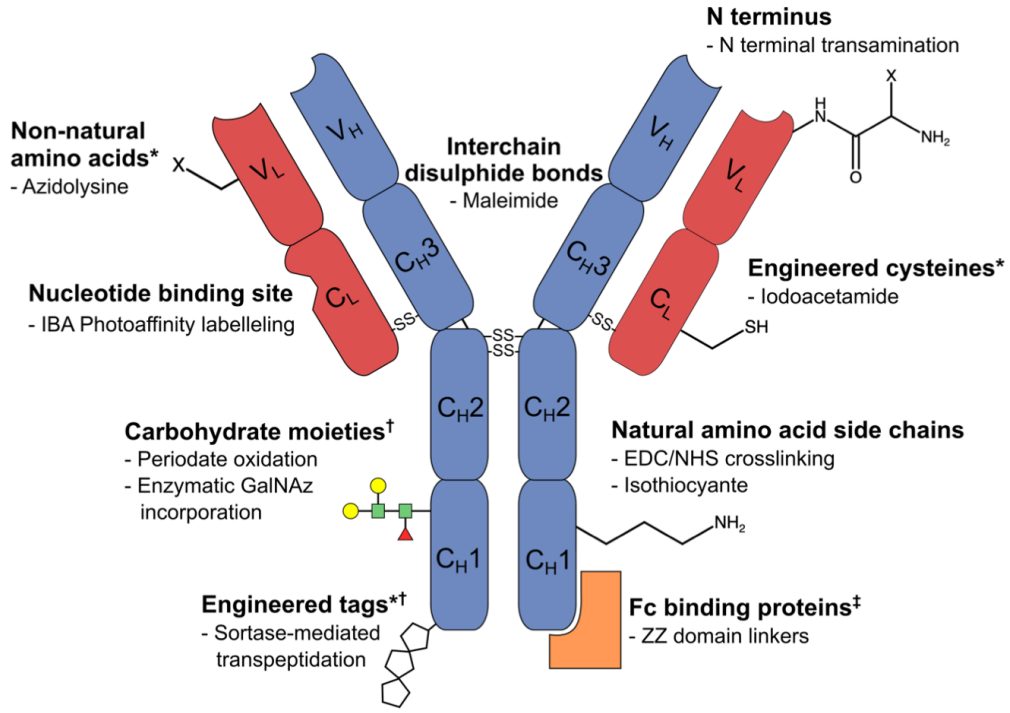


Figure 1.5) Conjugation strategies used for the development of antibody-drug conjugates. Monoclonal antibodies have been modified extensively with range of conjugation chemistries, including modification of naturally occurring moieties, genetically engineered conjugation sites (*), moieties that require enzymatic modification (†) and conjugation by non-covalent protein-protein interaction (‡). Adapted from Dennler et al. 2015.

1.4.2 Antibody conjugation of naturally occurring moieties

Antibodies are relatively large molecules, and therefore feature an abundance of naturally occurring sites that could be targeted for conjugation. One of the most common sites of modification is the ε-amine present on lysine side chains, due to its high abundance (>80 per IgG), positive charge and solvent accessibility (Mueller et al., 1988). Although the high amount of surface accessible lysine side chains is good for achieving high conjugate to antibody ratio (CAR), there is little to no control over site specificity or CAR, leading to the production of highly heterogenous mixtures which make thorough characterisation and optimisation difficult (Wakankar et al., 2010). One method of adding control to the amine conjugation technique is to carry out the reaction under stringent conditions, exploiting the difference in pKa values to selectively label the N-terminal α-amine instead of the lysine ε-amine group (Scheck and Francis, 2007). However, due to the proximity of the N-termini to the antigen biding domains, there is a risk of comprising the binding characteristics of the antibody.

Another attractive, naturally occurring site for conjugation is the cysteine side chain. Unlike lysine, cysteine is considerably less abundant than lysine with four interchain cysteine bonds within a typical IgG molecule, which translates to much greater control over the CAR and site selectivity (Mcauley et al., 2008). Furthermore, these cysteine residues almost exclusively form disulphide bonds, and must be reduced prior to conjugation, which has been exploited to add further control over site selectivity (Liu et al., 2010). Typically, cysteine side chains are labelled using disulphide exchange or addition of electrophiles, such as maleimide or iodoacetamide (Gauthier and Klok, 2008). One of the major drawbacks of these conjugation approaches is that they are prone to substitution *in vivo* with other naturally occurring thiol groups, such albumin or glutathione, reducing stability, although several groups have developed novel cysteine labelling techniques which are more resistant to substitution (Tumey et al., 2014, Bernardim et al., 2019).

Moving away from amino acid modification, antibodies can also be conjugated by modification of carbohydrate moieties, more specifically *N*-glycans which are added post translationally to specific asparagine residues within the Fc region on the antibody heavy chain, most notably asparagine 297 (N297) which is ubiquitous amongst the IgG class of antibodies (Krapp et al., 2003). Numerous approaches have been developed to modify antibody glycan residues, including using periodate oxidation or enzymatic methods to produce a biorthogonal aldehyde group for reaction with hydrazide- or primary amine-functionalised linkers (Ranadive et al., 1993, Zhou et al., 2014). In fact, enzymatic modification of *N*-linked glycan residues has previously been demonstrated to site specifically conjugate a monoclonal antibody with a radiometal chelator. Zeglis et al. used enzyme mediated modification to exchange the terminal galactose residues of the *N*-glycans on the Fc region of the prostate specific membrane antigen (PSMA) specific monoclonal antibody J591 with *N*-azidoacetylgalactosamine. This allowed for the subsequent reaction with a dibenzocyclooctyne modified derivative of the chelator deferoxamine (DIBO-DFO) by strain-promoted azide-alkyne cycloaddition (SPAAC), for radiolabelling with the PET isotope ^{89}Zr (Zeglis et al., 2013). Despite clear potential, the heterogenous nature of glycosylation patterns, glycan targeted antibody conjugation strategies often require significant optimisation from antibody to antibody, hindering versatility and translatability (Mastrangeli et al., 2019).

Recently, a novel conjugation has been developed to take advantage of the naturally occurring nucleotide binding site (NBS) within the non-variable region of the Fab domains, which is highly conserved across most antibody classes. Alves and co-workers used UV photo-crosslinking to conjugate indole-3-butyric acid (IBA) linked functional groups to IgG, specifically at the NBS, providing a method of relatively straightforward site-specific conjugation, although this method is yet to be evaluated *in vivo (Alves et al., 2013)*.

Finally, site-specific conjugation of native antibodies can also be achieved through protein-protein interactions, for instance, Fc specific binding proteins which interact non-covalently with the Fc region of an antibody. One such example is the ZZ domain, derived from Streptococcal protein A, which has been used as a linker to conjugate the epidermal growth factor receptor (EGFR) specific monoclonal antibody cetuximab to the cytotoxic payload PE28 (Barnea et al., 2013).

1.4.3 Antibody conjugation using unnatural or engineered moieties

In addition to modification of naturally occurring moieties, recombinant technology has been used to engineer specific moieties for conjugation, including canonical and non-canonical amino acids and enzyme-specific peptide tags. The most extensively used of these approaches involves the incorporation of unpaired cysteine residues into the backbone of the antibody, allowing the use of highly developed thiol specific conjugation technologies without disrupting interchain disulphide bonds (Stimmel et al., 2000). This technique is highly advantageous for controlling of both the site of conjugation and the CAR, however the addition of solvent accessible cysteine residues does increase the risk of aggregation.

The incorporation of non-canonical amino acids (NCAAs), or unnatural amino acids has also been explored for the purposes of antibody conjugation, utilising engineered orthogonal tRNA/aminoacyl-tRNA synthetase pairs to integrate NCAAs into the backbone of antibodies (Gao et al., 2019). Xiao et al. successfully used this technology to add the NCAAs p-acetylphenylalanine (pAcF) and azido-lysine (AzK) into an antibody backbone, allowing site specific conjugation of both cytotoxic payload and a fluorescent dye (Xiao et al., 2013). Although technologies such as these clearly have great potential for precise conjugation applications, they require significant amounts of antibody specific development, greatly limiting adaptability.

In addition to incorporation of single amino acid sites for subsequent conjugation, another approach involves the addition of a short peptide sequence, or tag, which can then be modified with a specific enzyme. Such methods have been used with several enzymes, including sortase A, a bacterial transpeptidase derived Staphylococcus aureus that catalyses the ligation of the peptide tag sequence LPXTG and a polyglycine motif (Ritzefeld, 2014). Interestingly, peptide directed enzymatic conjugation can also be carried out on some native IgG molecules by using the 'Q-tag' system, which uses a microbial transglutaminase to site selectively conjugate the highly conserved glutamine Q297 in the Fc region (Strop, 2014). Recent research, however, has raised concerns over the selectivity of this method when labelling the HER2 specific monoclonal antibody trastuzumab, showing labelling of an additional glutamine residue near the antigen binding site (Marculescu et al., 2019).

1.5 Cell penetrating peptides

1.5.1 Introduction and classification of cell penetrating peptides

A major challenge facing modern biomedical research is enhancing the bioavailability of potential therapeutic compounds. The ability to cross cellular membranes in particular presents a significant bottleneck as many novel therapeutic compounds, especially large macromolecules such as antibodies, are unable to penetrate biological membranes due to their large size and hydrophilicity without chemical, electrical, or mechanical assistance. Cell penetrating peptides (CPPs), also protein transduction domains (PTDs) represent a diverse collection of short length peptides (typically less than 30 amino acids) with the ability to facilitate the transmission of covalently, or non-covalently, associated molecular cargos across cellular membranes (Guidotti et al., 2017). Since the initial discoveries of the HIV-1 derived trans-activator of transcription (TAT) (Frankel and Pabo, 1988), or drosophila derived

antennapedia homeodomain protein-derived peptide (Antp) (Joliot et al., 1991), research characterising mechanisms of action and identification of novel CPPs has rapidly expanded, with over 1,800 unique CPPs currently listed on the online database CPPsite (Agrawal et al., 2016).

Given the large repertoire of available CPPs, there are several approaches towards classification, including origin, sequence and application (Pooga and Langel, 2015). The most commonly used classification system categorises CPPs based on chemical properties, into three groups: cationic, hydrophobic and amphipathic. Cationic CPPs were the first to be characterised and typically incorporate a succession of positively charged amino acids, notably arginine and lysine. Typical examples include the TAT peptide (GRKKRRQRRRPPGYG), Antp (RQIKIWFQNRRMKWKK) and nona-arginine (R_9). Hydrophobic CPPs represent a smaller proportion of CPPs and typically contain mostly non-polar residues and a low net charge, which is essential for correct function. Examples include Pep-7 (SDLWEMMMVSLACQY) (Gao et al., 2002) and the fibroblast growth factor 12 (FGF-12) derived CPP-C (PIEVCMYREP) (Nakayama et al., 2011). The final class of CPPs are the amphipathic group, which contain both charged, mostly lysine and arginine, and non-charged amino acids. The amphipathic group is somewhat diverse, containing both naturally occurring peptides, and chimeric peptides with hydrophobic motifs to aid membrane penetration, and charged motifs to facilitate trafficking to the nucleus.

1.5.2 Mechanisms of internalisation

Despite the discovery and establishment of an exhaustive array of CCPs over the last three decades, the exact nature of their internalisation mechanism remains elusive. The complexity of interactions that occur at the cell surface in conjunction with the physicochemical diversity of different classes of CPPs has resulted in the proposal of a variety of potential internalisation

mechanisms, which could be utilised to different extents by different CPPs (Ruseska and Zimmer, 2020). Initially, attempts to determine the principle mechanisms of internalisation were hampered by fixation artefacts prior to confocal microscopy, leading to invalid conclusions (Vives et al., 2003). Although this issue has been addressed, the establishment of definitive answers is further confounded by the fact that the preferred mechanism of internalisation is dependent on a myriad of other factors, such as temperature (Fretz et al., 2007), extracellular concentration (Kosuge et al., 2008) and associated cargo (Tunnemann et al., 2006). The proposed mechanisms exploited by different CPPs can be broadly divided into two categories, energy independent direct translocation pathways and the energy dependent endocytic pathways.

1.5.3 Direct translocation mechanisms of CPP internalisation

Initial evidence of CPP internalisation by direct translocation mechanisms resulted from experiments showing internalisation to occur even at low temperatures, suggesting these mechanisms occur without an active process facilitated by the target cell (**Figure 1.6**) (Wender et al., 2000). Further support for direct translocation mechanisms came from research that internalisation of certain CPPs could occur in energy depleted systems and in the presence of endocytosis inhibitors (Suzuki et al., 2002). It is important to note that most reports suggest that mechanisms of direct translocation of CPPs are favoured at higher extracellular concentrations (Duchardt et al., 2007), and in the absence of cargo proteins (Tunnemann et al., 2006), which suggests these mechanisms are less likely to be relevant in the context of delivering antibody-based imaging agents into cells.

The first direct translocation mechanism to be characterised was described as inverted micelle formation, which was reported to be exploited by the well documented CPP penetratin (Derossi et al., 1998). The mechanism initiates with an electrostatic interaction between the CPP and

the lipid bilayer that modifies the curvature of the membrane, inducing an invagination of the CPP-cargo complex into an inverted micelle, the hydrophilic nature of the inverted micelle propagates accumulation of the CPP until it becomes destabilised, releasing the CPP-cargo complex into the cell cytoplasm.

In addition to the inverted micelle mechanism, several CPPs have been reported to achieve direct translocation by a transient pore forming mechanism. These pore forming mechanisms are typically utilised by primary amphipathic CPPs and involve two possible mechanisms, the 'barrel-stave' and the 'toroidal' models (Trabulo et al., 2010). The barrel stave model involves the formation of CPP bundles that form a structure in the lipid bilayer with a hydrophilic core. Alternatively, the toroidal model relies on the interaction between positively charged side chains of amphipathic CPPs and phosphate head groups of the cell membrane, this results in an accumulation of the CPP that perturbs the outer leaflet of the lipid bilayer, exposing a hydrophilic pocket, facilitating the movement of the CPP and hydrophilic cargo across the cellular membrane.

The final proposed mechanism of direct translocation is the carpet destabilisation model. In a similar fashion to the other proposed mechanisms of direct translocation, it involves interaction between the charged residues of the CPP and the lipid bilayer (Lundberg and Langel, 2003). The positively charged amino acids interact with acidic phospholipid head groups of the cell membrane causing multiple CPPs to accumulate in an orientation parallel to the cell surface, forming a 'carpet'. This allows the orientation of hydrophobic and hydrophilic residue side chains towards the lipid and hydrophobic components of the lipid bilayer respectively, triggering a conformational change and destabilisation in the membrane required for the translocation of the CPP-cargo complex.

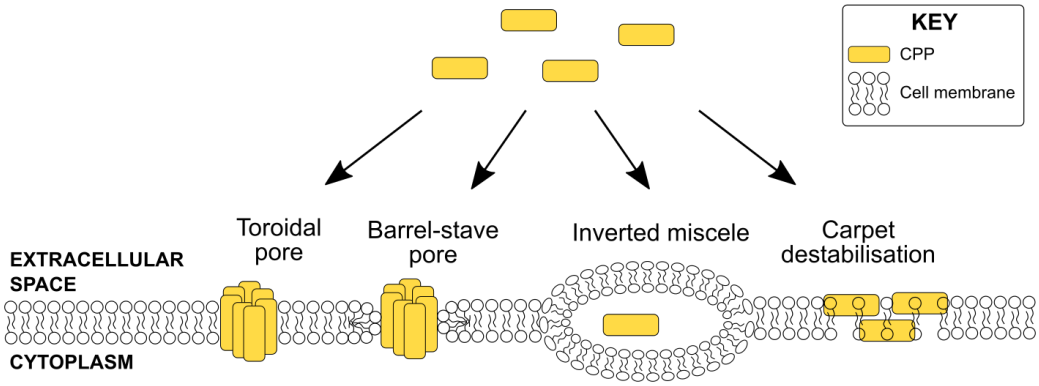


Figure 1.6) Proposed models of CPP internalisation by energy independent direct penetration. Unlike endocytosis mediated cell entry, these mechanisms rely on the formation of hydrophilic pores within or destabilisation of the cell membrane. Energy independent CPP internalisation is generally favoured at high extracellular concentrations of CPP and not when attached to a cargo protein. Adapted from Trabulo et al. 2010.

1.5.4 Endocytosis-dependent mechanisms of CPP internalisation

The alternative mechanisms to internalisation of CPPs by direct translocation involve endocytosis, which is an energy dependent cellular process where the cell invaginates a target into an endosome prior to endosome escape (**Figure 1.7**) (Zhao et al., 2011). There are several methods of endocytosis that can be utilised by the cell, which broadly fall into two categories, phagocytosis and pinocytosis. Whilst phagocytosis is limited to a distinct group of specialised immune cells and is used to engulf large cellular structures, pinocytosis is used universally by cells to take up materials from the extracellular matrix and is utilised by CPPs (Conner and Schmid, 2003). Furthermore, pinocytosis can be further be classified primarily into four mechanisms, including macropinocytosis, clathrin-mediated endocytosis (CME), caveolae-mediated endocytosis (CvME) and clathrin- and caveolae-independent endocytosis. In contrast to direct translocation, endocytosis driven mechanisms predominate in cases of lower

extracellular concentration (< 10 μM) and when co-transporting cargo proteins (Kauffman et al., 2015).

1.5.5 CPP internalisation by macropinocytosis

Macropinocytosis is a receptor independent, yet regulated form of endocytosis that involves a rearrangement of the actin cytoskeleton to form protrusions from the cell membrane. This protrusion then surrounds a section of extracellular material and collapses back into the cell membrane, in turn creating an endocytic vesicle within the cell cytoplasm called a macropinosome. Macropinocytosis is regulated by a range of signalling cascades associated with cytoskeleton remodelling, for instance Rho GTPase signalling pathways, and likewise is usually initiated by stimulation by growth factors, for instance epidermal growth factor (EGF) or platelet derived growth factor (PDGF) (Swanson and King, 2019). The role of macropinocytosis in the uptake of cationic CPPs, has been established by findings that uptake of a range of cationic CPPs was significantly reduced in conditions where macropinocytosis was inhibited, whether by reducing temperature of cell culture to 4°C (Kaplan et al., 2005), or in the presence of macropinocytosis specific inhibitors, including the inhibitor of actin polymerisation cytochalasin D and Amiloride, a Na^+/H^+ exchanger blocker (Wadia et al., 2004).

Extensive research has been focused on determining the extent to which CPPs modulate macropinocytosis, with several proposed interactions at the cell membrane. Numerous reports demonstrated the importance of cell membrane associated proteoglycans, in particular heparan sulphate proteoglycans (HSPGs) (Letoha et al., 2010). Research using Chinese hamster ovary (CHO) cells with compromised HSPG synthesis pathways showed a significant reduction in internalisation of several cationic CPPs, including octa-arginine (R_8) and TAT (Nakase et al., 2007). The syndecan family of HSPGs have been shown to act as co-receptors for G protein

coupled receptors (GPCRs), which have been linked with the initiation of endocytosis (Carey, 1997). In the presence of R_8, elevated expression of syndecan-4 in He-La cells resulted in increased internalisation of R_8, which is believed to promote macropinocytosis in a Rac1 dependent manner (Nakase et al., 2014). However, research from other groups has linked internalisation of TAT-conjugated nanoparticles with the transmembrane protein neuropilin-1 (NRP1), a co-receptor with roles in a variety of cellular processes, in a HSPG-independent manner (Pang et al., 2015). Interestingly, internalisation of a longer length CPP, dodeca-

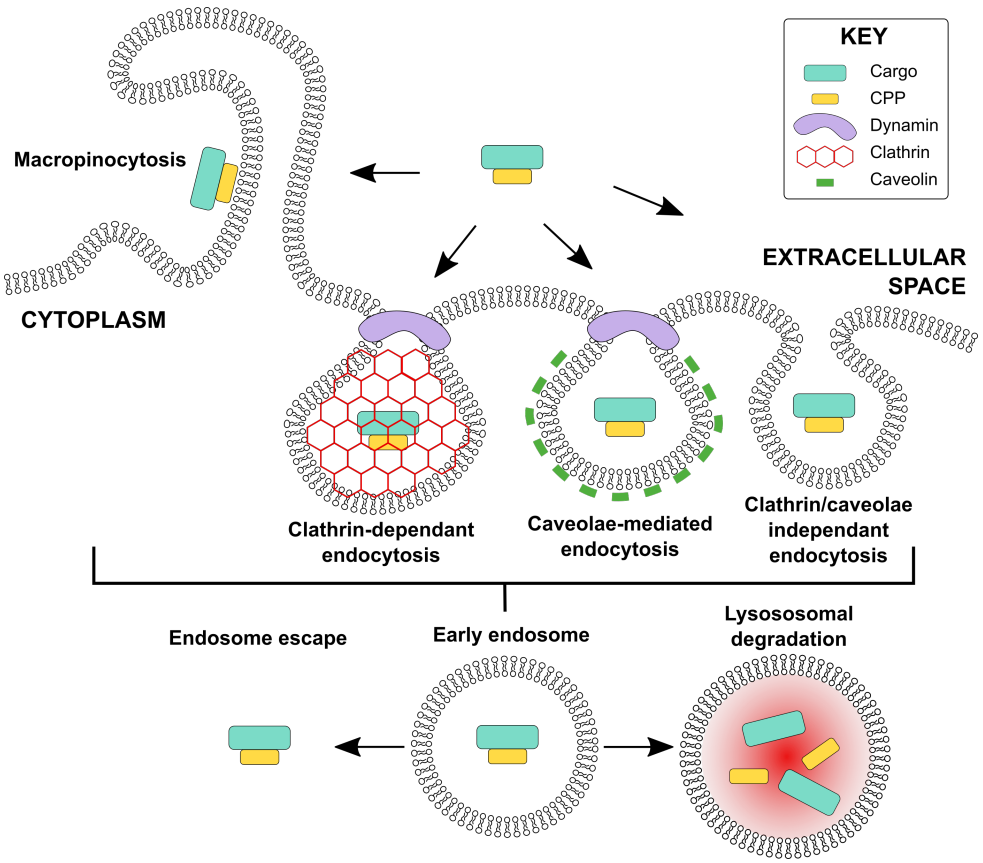


Figure 1.7) Endocytic mechanisms of CPP internalisation. Reports from several studies have shown that CPPs are capable of exploiting a range of endocytic pathways to achieve cell entry. Unlike proposed models of direct penetration, these mechanisms are energy dependent and are favoured at lower extracellular concentrations of CPP (<10 μM). Once a CPP-cargo complex has been endocytosed, it must undergo endocytic escape in order to evade lysosomal degradation and gain access to the cell cytoplasm. Adapted from Trabulo et al. 2010.

arginine (R_{12}) could be inhibited by siRNA knockdown of the chemokine receptor CXCR4, but this was not the case with either TAT or R_8, suggesting that different CPPs utilise different receptors to facilitate the same mechanisms of internalisation (Tanaka et al., 2012).

1.5.5 CPP internalisation by clathrin-mediated endocytosis (CME)

Clathrin-mediated endocytosis (CME) is a receptor dependent endocytic pathway that is reliant on the GTPase dynamin and is the most studied mechanism of endocytosis. CME is initiated by various receptor pathways and is characterised by the formation of polyhedral lattices comprised of clathrin proteins assembled into a triskelion formation that forms an invagination in the cell membrane, which undergoes dynamin mediated vesicle fission to yield an endocytic vesicle (McMahon and Boucrot, 2011). CPPs have been documented to exploit CME as a means of entering a cell and research has shown that specific inhibition of CME, using chlorpromazine and K^+ depletion, reduces uptake of TAT in He-La and CHO cells (Richard et al., 2005). Interestingly this effect was found to be dependent on the presence of HSPG, which has been identified previously as having a primary role in macropinocytosis-mediated CPP uptake (Richard et al., 2005). This report was further supported by more recent findings that siRNA knockdown of the HSPG syndecan-4 was unable to further reduce uptake of the cationic CPP R_8 after addition of CME specific inhibitors monodansylcadaverine (MDC) and Pitstop® 2, suggesting a non-redundant relationship between HSPG syndecan-4 and clathrin-coated endocytosis of R_8, suggesting that HSPG dependent uptake of R_8 was driven primarily by CME rather than macropinocytosis (Kawaguchi et al., 2016). Although these results seem contradictory to other reports suggesting macropinocytosis as the primary mechanism behind syndecan-4 mediated internalisation, it is plausible that syndecans perform roles in both clathrin-mediated endocytosis and macropinocytosis.

1.5.6 CPP internalisation by caveolae-mediated endocytosis (CvME)

Caveolae-mediated endocytosis (CvME), like CME, is a receptor and dynamin dependent mechanism of endocytosis. Unlike clathrin-coated pits, caveolae are characterised by uniformly sized, bulb shaped invaginations comprised of oligomerised proteins of the caveolin family in associated with cavin proteins (Parton, 2018). Furthermore, where the occurrence of CME is consistent across most cell types, CvME shows a striking polarity in incidence depending on cell type, with some tissues, such a skeletal muscle featuring up tp 50% of cell surface membrane incorporated into caveolae, whereas in other tissues, such as liver, caveolae formation is rare or even totally absent.

Several reports have suggested that in some cases, CvMW might be the preferred mechanism of internalisation. One study using TAT tagged with glutathione S-transferase (GST) and enhanced green fluorescent protein (EGFP) showed colocalization between GST-TAT-EGFP and caveolin-1 (Ferrari et al., 2003). Further support comes from research demonstrating that knockdown of caveolin-1 lead to a reduction in internalisation of the amphipathic CPP Transportan bound to biotin in complex with avidin (Saalik et al., 2009). Interestingly, this study and others suggesting a CvMV dependent CPP internalisation mechanism involve CPPs that have been conjugated to relatively large molecular cargos. Given that some reports suggest that larger size molecular cargos are preferentially trafficked by CvMV over CVM (Rejman et al., 2004), this could be yet another example of how CPPs can utilise different internalisation mechanisms under different physiological conditions.

1.5.7 CPP internalisation by other endocytic mechanisms

Cells are capable of undertaking endocytosis even in cases where dynamin activity is disrupted, and in the presence of the macropinocytosis specific inhibitor amiloride, therefore other mechanisms of endocytosis that are clathrin- and caveolae-independent are also available to

the cell (Kirkham and Parton, 2005). This diverse group are the least characterised mechanisms of endocytosis, and current findings suggest that they are almost invariably actin- and cholesterol-dependent, involving the organisation of specific lipid species with lipid anchored proteins, such as glycosylphosphatidylinositol-anchored proteins (GPI-APs) on the cell surface (Mayor et al., 2014). Together, they instigate a conformational change in the cell membrane, resulting in the formation of an endocytic vesicle. The role of these mechanisms in the internalisation of CPPs is still unclear, with limited number of studies. However, one study focused on the uptake of siRNA in complex with the cationic CPP low molecular weight protamine (LMWP) showed uptake of siRNA even in the presence of inhibitors of both CME and CvME, in addition to the GTPase inhibitor dynasore (Ye et al., 2018).

1.5.8 Endosomal release of CPPs

Once a CPP-cargo has been internalised into a cell by endocytosis, the CPP-cargo must be released from the endosome in order to reach the cytoplasm where it can perform its intended action (LeCher et al., 2017). Under normal circumstances, vesicles formed by endocytosis are trafficked to an early endosome, which has a slightly acidic lumen (pH ~6.5) (Hu et al., 2015). The early endosome then undergoes maturation to a late endosome, becoming more acidic in the process (pH ~5.5), before finally fusing with a lysosome (pH ~4.7). At this stage the contents of the lysosome are degraded by hydrolytic enzymes. Endosomal release, or escape, before lysosomal degradation presents a critical bottleneck for effective cytoplasmic CPP-cargo delivery, and is highly inefficient (Varkouhi et al., 2011). Subsequently, extensive research has been carried out to elucidate both the mechanisms behind endosomal escape and how to increase efficiency of CPP delivery to the cytosol.

1.5.9 Mechanisms of endosomal escape of CPPs

As with mechanisms of endocytic internalisation of CPPs, several mechanisms of endosomal release have been postulated and it is possible that different CPPs utilise different mechanisms under different physiological conditions. One of the earliest suggested mechanisms was the 'proton-sponge' hypothesis, which has been suggested to facilitate the endosomal release of large, polycationic CPPs, such as polyethyleneimine (PEI), which have large buffering capacities at pH 5-7 (Sonawane et al., 2003). This mechanism relies on the ability of polycationic CPPs to effectively buffer early endosomes, forcing the endosome to increase the influx of H^+ ions to counteract the buffering capacity of the CPP. The increased charge of endosomes containing CPPs leads to the influx of Cl^- ions causing an increase in osmotic pressure and lysis of the endosome, releasing the contents of the endosome into the cytosol. This mechanism, though, is confounded by the fact that several cationic polymers were unable to induce endosomal escape in spite of buffering capacity in the desired range (Funhoff et al., 2004). Furthermore, both TAT and polyarginine-based CPPs do not undergo protonation in the pH range required to act as a lysosomal proton sponge but can nevertheless evade lysosomal degradation (Pei and Buyanova, 2019). Finally, lysis of late-stage endosomes would result in significant cell toxicity, which is inconsistent with the low cytotoxicity observed with many CPPs.

Other proposed mechanisms involve the direct translocation of the CPP-cargo complex over the endosomal membrane, including pore formation and membrane destabilisation in a similar manner to direct penetration mechanisms discussed previously (ur Rehman et al., 2013). However, these mechanisms rely on achieving high concentrations of CPP at cellular membranes and are ineffective at transporting cargo proteins (Sahni et al., 2020). The most recent hypothesis, proposed by Pei and colleagues, suggests that CPPs escape the endosome by promoting budding of the endosomal membrane to form smaller sub-vesicles, which

collapse, releasing the CPP and associated cargo into the cytoplasm (Qian et al., 2016). This mechanism relies on the conformation of the CPP and spatial arrangement of charged side chains to induce endosome escape and is distinct from other proposed mechanisms as it maintains the integrity of the majority of the endosome whilst still resulting in the localised deterioration of the endosomal membrane.

1.6 TAT-IgG based molecular imaging of intranuclear epitopes

1.6.1 Overcoming cellular barriers

Monoclonal antibodies clearly have great potential as molecular imaging agents. However, the overwhelming majority of research surrounding mAb based molecular imaging is focused on targets that are expressed on either the cell membrane or secreted extracellular epitopes. This is a consequence of the relative size and hydrophilicity of mAbs, which dramatically reduces their ability to cross cellular membranes. Given that approximately 30% of cellular proteins are located within the cell nucleus, and coordinate a multitude of essential cellular functions, the ability to target nuclear proteins would considerably increase the range of applications of antibody based molecular imaging (Shaiken and Opekun, 2014). The utilisation of cell penetrating peptides (CPPs), such as TAT, have shown initial promise in overcoming the barriers of cell permeability and thus increasing the repertoire of targets available for mAb-based nuclear imaging.

1.6.2 The TAT peptide

First identified as having cell penetrating characteristics in 1988, transactivator of transcription (Tat) is a 14 kDa, RNA binding protein encoded by the *tat* gene of human immunodeficiency virus 1 (HIV-1), which dramatically increases the transcription efficiency of HIV-1 mRNA.

Tat has several domains involved in the recognition of transactivator response element (TAR), a HIV-1 specific secondary mRNA structure, and the recruitment of elongation factor complexes, such as the positive transcription elongation factor (P-TEFb). Further research with truncated variants of Tat identified the basic domain (^{48}GRKKRRQRRRPPQC^{60}) was essential for cell membrane translocation (Vives et al., 1997). This breakthrough ultimately led to the development of the cationic cell penetrating peptide TAT (GRKKRRQRRRPPQGYG). As a cationic CPP, the internalisation of TAT and TAT-bound bioconjugates is facilitated primarily by endocytosis. In addition to having cell penetration capacity, TAT is also capable of translocation into the cell nucleus via an intrinsic nuclear localisation sequence (NLS; GRKKR), with in vitro analysis showing that TAT is capable of binding both importin-α (Smith et al., 2017b) and importin-β (Truant and Cullen, 1999), which are principally involved in the classical energy dependent nuclear import pathway (Freitas and Cunha, 2009).

The combination of both cell penetrating and nuclear localisation characteristics make TAT an ideal CPP for targeting macromolecular cargo proteins to the cell nucleus. Subsequently TAT and TAT-bound bioconjugates have undergone extensive research investigating potential applications for intranuclear therapeutic delivery, including enhanced delivery of small molecule inhibitors (Staecker et al., 2019), nucleic acids (Kanazawa et al., 2014), and full size proteins (Gaston et al., 2019). Most applications of TAT-cargo conjugates typically rely on targeting an extracellular moiety, exploiting the internalising characteristics of TAT to deliver an intranuclear therapeutic cargo to a cell expressing the appropriate extracellular marker. However, several reports have demonstrated that TAT-conjugated RICs are capable of specifically targeting intranuclear epitopes, which significantly increases the range of potential target moieties and subsequent applications. Among the first, Hu et al. demonstrated increased tumoural uptake of a ^{123}I labelled TAT-conjugated RIC targeting the nuclear localised cyclin dependent kinase inhibitor p21$^{WAF1/Cip1}$ after its induction in a mouse xenograft model by

intratumoural EGF injection (Hu et al., 2007). A similar approach was utilised by Cornelissen and colleagues to show increased tumoural uptake of an ^{111}In labelled TAT-anti-p27^{Kip1} RIC in a xenograft MDA-MB-361 breast cancer model following treatment with trastuzumab (Cornelissen et al., 2009). The most promising application of TAT-based RIC imaging of intranuclear targets has been the *in vivo* imaging of the DNA damage response marker γH2AX using both PET and SPECT imaging modalities. Initially characterised by Cornelissen et al. (2011), this approach has spawned several potentially useful applications, including early detection of neoplasia in breast (Cornelissen et al., 2014) and pancreatic (Knight et al., 2019a) cancer models, in addition to early monitoring of the tumour response to both chemotherapy (Knight et al., 2017) and radionuclide therapy (Poty et al., 2020, O'Neill et al., 2020).

1.6.3 Conjugation of TAT-IgG RICs

The modification of an antibody to produce an intranuclear targeted RIC requires the conjugation of the CPP/NLS TAT and a suitable chelating agent for radiolabelling with the desired radioisotope. The conjugation of functional moieties onto antibodies and the development of antibody-drug conjugates (ADCs) has become a rapidly accelerating field of research and there is an abundance of conjugation chemistries available, including site-specific and 'unnatural' engineered approaches. It is important to note that each conjugation strategy will have specific advantages and disadvantages and different applications will require different conjugation chemistries for optimal performance.

Previous studies using TAT-IgG based RICs have employed carbodiimide crosslinker chemistry, using the protein-protein crosslinker 1-ethyl-3-(3-dimethylaminopropyl) carbodiimide (EDC) crosslinker, to conjugate TAT to the antibody (Hermanson, 2013). This method relies on the presence of naturally occurring, solvent-accessible carboxylic acid sidechains on the antibody, which are covalently bound to accessible primary amine groups of

the TAT peptide. The major advantage of this method is that neither the antibody nor the TAT peptide requires modification prior to conjugation, therefore this approach can easily be translated to alternative antibodies/CPP combinations. However, the lack of site specificity can lead to significant variation in the location of TAT conjugation and the TAT:IgG ratio, potentially yielding inconsistent results, especially when making comparisons between different antibodies. Also, as EDC indiscriminately crosslinks any accessible primary amines and carboxyl groups, there is a small albeit tangible risk of crosslinking antibody molecules together, potentially reducing the potency of the RIC.

The generation of a TAT-IgG RIC also requires the covalent addition of a metal ion chelator for radiolabelling with the desired radioisotope. Commonly used examples include diethylenetriaminepentaacetic acid (DTPA) and desferoxamine (DFO) for subsequent labelling with ^{111}In and ^{89}Zr respectively. This conjugation is typically carried out using a chelator already modified with an amine reactive activated ester group, such as isothiocyanate (SCN) or *N*-hydroxysuccinimide (NHS) to label accessible primary amines present on the antibody, typically the ε-amino group on lysine side chains. Similar to the EDC-crosslinker chemistry, this technique does not require prior manipulation of the antibody and can easily be translated to different applications.

1.7 Aims of the study

Cell penetrating peptide, and more specifically TAT-IgG-based *in vivo* imaging of intranuclear targets with RICs has great potential as a highly sensitive, specific and versatile imaging modality. However, this technology is still very much in the early stages of development. Before this imaging modality can be successfully translated into clinical applications, TAT-IgG based PET/SPECT imaging will require a rigorous and robust characterisation of its

technical limitations. Furthermore, this characterisation will facilitate future optimisation of TAT-IgG based imaging *in-vivo*, increasing the potential of this already promising technology. Detection of intranuclear biomarkers using TAT-IgG based imaging probes has already been validated for targeting several key cancer targets, including $p21^{WAF1/Cip1}$, $p27^{Kip1}$ and γH2AX. However, in order to guide future research when selecting candidate biomarkers for imaging, it would be highly beneficial to know what biological parameters must be met for successful *in vivo* imaging, principally what is the minimum requirement copy number for a prospective biomarker.

In order to explore what is possible with TAT-IgG based intranuclear imaging, a recombinant cell model system expressing different levels of a nucleus bound enhanced green fluorescent protein (H2B-EGFP) was developed and validated (**Chapter 2**). In tandem, a murine anti-GFP monoclonal antibody (GFP-G1) was expressed and purified prior to validation *in vitro* of specificity and sensitivity.

In addition to testing the technical limits of the IgG-TAT imaging of nuclear targets, this study will develop and evaluate a new conjugation strategy to covalently modify polyclonal and monoclonal antibodies using a non-site-specific SPAAC click chemistry approach. The GFP-G1 monoclonal antibody will be conjugated using this proposed new method to produce an anti-GFP RIC (^{111}In-DTPA-GFP-G1-TAT) and the complementary H2B-EGFP model system will be used to compare this conjugation strategy with the traditional method of RIC production by carbodiimide cross-linking (**Chapter 3**).

With a new conjugation strategy and target model system in place, cell-based uptake of ^{111}In-DTPA-GFP-G1-TAT will be evaluated in response to decreasing levels of expression of H2B-EGFP to determine the lowest detectable protein copy number of H2B-EGFP *in vitro* (**Chapter 4**). This was followed by *in vivo* evaluation of ^{111}In-DTPA-GFP-G1-TAT uptake using an

H2B-EGFP xenograft tumour model, where both *ex vivo* biodistribution and SPECT image analysis were conducted.

Finally, in a separate project, the TAT-IgG architecture was employed to image the phosphorylation of the protein kinase ataxia telangiectasia mutated (ATM), as a way of imaging of the DNA damage response (DDR), principally the response to double strand breaks (DSBs) (**Chapter 5**). This initially involved the validation of ATM expression and phosphorylation after DSB induction, followed by evaluation of a range of commercially available anti-pATM antibodies. The optimum antibody was then conjugated with CCP TAT and chelator DTPA for radiolabelling with ^{111}In for *in vitro* by uptake and retention assays.

Chapter 2

Development of a GFP-based model system to evaluate the limitations of IgG-TAT-based imaging of intranuclear epitopes

2.1 Introduction

Monoclonal antibody-based molecular imaging has great potential to provide an abundance of applications within clinical oncology, offering a highly sensitive, specific, and versatile molecular imaging modality (Wu, 2014). Whilst antibody- or antibody fragment-based molecular imaging has already been explored extensively for imaging target proteins expressed on the surface of the cell, the ability to utilise the benefits of monoclonal antibodies for imaging intracellular targets would significantly increase the range of potential targets, and subsequent applications. For example, an estimated 30% of all cellular proteins are expressed in the nucleus, including a variety of cancer relevant markers, such as the tumour suppressor protein p53 or the oncoprotein MYC (Shaiken and Opekun, 2014).

One of the major obstacles facing antibody-based intracellular imaging is the relatively high molecular mass and hydrophilicity of antibodies that, as with most proteins, render them unable to penetrate cellular membranes. However, the use cell penetrating peptides, such as TAT (Frankel and Pabo, 1988), or penetratin (Derossi et al., 1994), have shown that it is possible to

translocate large biomolecules, including proteins up to 540,000 kDa across the cellular membrane in an endocytosis dependant manner (Mussbach et al., 2011).

Previous research from this group and others have demonstrated that IgG-TAT-based RICs can be used to target several intranuclear proteins, including p21, p27 and γH2AX (Cornelissen et al., 2011, Cornelissen et al., 2009, Hu et al., 2007, Poty et al., 2020). However, given the versatility of antibody targeting, one of the key outstanding questions surrounding IgG-TAT based RICs is what characteristics make a target epitope a suitable candidate for RIC based molecular imaging, both *in vitro* and *in vivo*? In particular, I aimed to determine the effect of decreasing target abundance on imaging an exclusively intranuclear epitope using an IgG-TAT-based RIC in a controlled model setting, establishing a platform for both evaluation and optimisation of this technology.

To explore the detection limits of IgG-TAT based RICs, I set out to produce and interrogate a model system that expressed a target protein at a quantifiable level that was both stable over time and resistant to change in response to environmental factors imposed on the model system, such as DNA damage or pharmacological intervention. I chose to use the histone-2B tagged enhanced green fluorescent protein (H2B-EGFP) as a model target system, as the expression level and subcellular location of H2B-EGFP could be conveniently assessed during the generation of model cell lines (Kanda et al., 1998).

In addition to using a defined target model system, the validation and characterisation of complementary anti-GFP antibody would also be essential as the specificity and affinity of the native antibody would present a critical factor influencing the efficacy of any IgG-TAT based intranuclear imaging probe (Reddy and Robinson, 2010). For this project, I also validate the specificity and determine the affinity of murine monoclonal antibody GFP-G1 against H2B-EGFP (Yamagata and Sanes, 2012). In summary, the principal objective of this chapter was to

develop a GFP-based model system to evaluate and in the future optimise the use of TAT-IgG RICs for targeting intranuclear epitopes.

2.2 Materials and methods

2.2.1 Cell culture

Human lung adenocarcinoma H1299 cells (ATCC, VA, USA) were cultured in Dulbecco's Modified Eagles Medium (DMEM) (MilliporeSigma, MO, USA), supplemented with 10% foetal bovine serum (Thermo Fisher Scientific, MA, USA), 2 mM L-glutamine, 100 units/mL penicillin, and 0.1 mg/mL streptomycin and maintained in a 5% CO_2 humidified atmosphere at 37°C. Cells were authenticated by the providers. Cells were tested for the absence of mycoplasma at regular intervals. Cells stably transfected with H2B-EGFP plasmid were cultured with 50 μg/mL G418/geneticin to promote stability of transfection. Cells were harvested and passaged as required using trypsin-EDTA solution.

2.2.2 Stable transfection of H1299 cells

H1299 cells were seeded onto 6 well plate cell culture dishes and allowed to attach overnight and reach 75-90% confluency. Cells were then transfected with H2B-EGFP plasmid (Addgene #11680) (Kanda et al., 1998) using lipofectamine 3000 (Invitrogen, CA, USA) according to manufacturer protocols. After transfection (48 h), stably transfected cells were selected by culture with 800 μg/mL G418/geneticin antibiotic for 6 passages (2 weeks). Cells that survived initial selection were sorted for EGFP green fluorescence and plated as individual cells using flow assisted cell sorting (FACSAria III, BD Biosciences). Individual cell colonies were expanded under G418 selection (200 μg/mL) and H2B-EGFP expression in candidate cell lines

was initially assessed qualitatively using immunofluorescence microscopy. After establishing four stably transfected cell lines, in addition to wild type (WT) H1299 cells, which were used as a negative control, H2B-EGFP expression was evaluated by western blot, immunofluorescence microscopy, flow cytometry and ELISA. Stability of H2B-EGFP expression in the absence of G418 was determined using flow cytometry.

2.2.3 Western blot

Aliquots of 1.2 x 10^5 cells were plated in 6 well plates with complete culture medium and incubated overnight at 37°C with 5% CO_2. Cells were placed on ice and washed twice with ice cold phosphate buffered saline (PBS) (137 mM NaCl, 2.7 mM KCl, 10 mM Na_2HPO_4, 1.8mM KH_2PO_4, pH 7.4) before lysis by addition of 100 µL radioimmunoprecipitation assay (RIPA) buffer (50 mM Tris-HCl, 150 mM NaCl, 1% Triton X-100, 0.5% sodium deoxycholate, pH 8.0) plus cOmplete™ EDTA-free Protease Inhibitor Cocktail (Sigma-Aldrich, MO, USA). Lysates were collected and set on ice for 20 min with vortexing every 5 min. Lysates were clarified by centrifugation (30 min, 16,000 x g, 4℃) and protein concentration of supernatants was determined using a colourimetric bicinchoninic acid (BCA) assay (Sigma-Aldrich, MO, USA) prior to storage at -20℃ until required. Lysates were denatured and linearised by the addition of 2X Laemmli sample loading buffer (4% SDS, 20% glycerol, 120 mM Tris-HCl pH 8.6, 0.02 % w/v bromophenol blue) and heated to 96℃ for 5 minutes prior to loading for separation on pre-cast SDS-PAGE gels (Thermo Scientific, MA, USA). Separated proteins were transferred onto a polyvinylidene fluoride (PVDF) membrane using an XCell II™ Blot Module according to manufacturer protocol (Invitrogen, CA, USA). Transferred membranes were rinsed in tris buffered saline (TBS) pH 7.4 and blocked in blocking buffer (5% milk powder dissolved in TBS + 0.1% Tween®-20 (TBST)) for 1 h at room temperature. Membranes were incubated with primary antibody in blocking buffer overnight at 4℃. Blocked

membranes were washed 3 x 15 min in TBST, incubated with horseradish peroxidase (HRP) conjugated secondary antibody for 1 h at room temperature and washed 3 x 15 min again in TBST. Membranes were developed by addition of Pierce™ ECL Western Blotting Substrate (Thermo Scientific, MA, USA) and chemiluminescence was detected using C-DiGit® Blot Scanner (LI-COR, NE, USA). See appendix (**Table A1**) for references to antibodies used in this thesis.

2.2.4 Immunofluorescence microscopy

2 x 10^4 cells were plated in 8 well chambered tissue culture slides (Fisher Scientific, NH, USA) with complete culture medium and incubated overnight at 37℃ and 5% CO_2. Cells were rinsed three times in ice cold PBS twice before fixation by addition of PBS containing 4% paraformaldehyde (PFA) at 37℃ for 10 min followed by washing with PBS. Cells were then permeabilised by addition of 0.2% Triton X-100 at 4℃ for 20 min and washed again with PBS. Blocking solution of PBS + 2% FBS was added for 1 h at room temperature before washing in PBS and addition of blocking solution with the primary antibody at the desired concentration, which was incubated at 4℃ for 16 hours. The primary antibody solution was removed, and cells washed three times in PBS for 15 min before addition of blocking solution containing the appropriate secondary antibody for 1 hour at room temperature. Stained cells were then washed three times in PBS for 15 min before mounting with Vectashield® mounting media containing 4',6-diamidino-2-phenylindole (DAPI) (Vector Laboratories, CA, USA). Confocal microscopy of stained cells was carried out on the Leica TCS SP8 platform (Leica Microsystems, Wetzlar, Germany), equipped with 63 × oil-immersion objective lenses. Within each experiment, image acquisition and processing parameters were kept consistent for each sample.

2.2.5 Flow cytometry

Aliquots of 2 x 10^6 cells were plated in a T175 cell culture flask with complete culture medium and incubated overnight at 37℃ with 5% CO_2. Cells were washed twice in ice cold PBS and collected by scraping followed by another wash by centrifugation (400 × g, 5 min). Cells were fixed by incubation in PBS containing 4% PFA at 37℃ for 10 min followed by washing by centrifugation in PBS. Fixed cells were permeabilised by addition of 0.25% Triton X-100 in PBS at 4℃ for 20 min and washed again in PBS prior to blocking in flow cytometry blocking buffer (PBS containing 2% foetal bovine serum (FBS)) for one hour at room temperature, then washed in PBS and incubated for 2 h at room temperature with the appropriate primary antibody in flow cytometry blocking buffer at the desired concertation. Stained cells were washed with PBS before incubation for 1 h at room temperature with an appropriate fluorophore conjugated secondary antibody. Data was acquired using Invitrogen Attune NxT flow cytometer (Invitrogen, CA, USA). Data analysis was carried out using FlowJo™ v10.6.2 (FlowJo LLC, OR, USA).

2.2.6 Enzyme linked immunosorbent assay (ELISA)

The concentration, of H2B-EGFP was determined using a SimpleStep ELISA® GFP ELISA KIT, which includes all buffers used in this assay (Abcam, Cambridge, UK). Lysates of H1299 WT and H2B-EGFP expressing clones were prepared by incubation with ELISA 1X cell extraction buffer PTR (Abcam, Cambridge, UK) on ice for 20 min, followed by clarification by centrifugation (16,000 x g, 20 min). Concentration of clarified lysates was adjusted to 2 ug/mL and incubated for 1 h, at room temperature, with an anti-GFP capture and detection antibody cocktail within 8 well ELISA strip plates coated with a capture protein specific tag. Lysates were removed and plates with bound antibody were washed three times with ELISA wash buffer. Bound detection antibody was detected by incubation with 3,3′,5,5′-

tetramethylbenzidine (TMB) buffer for 20 min, followed by addition of stop solution. The optical density (450 nm) was gathered using a Tecan M200 Pro microplate reader (Tecan, Männedorf, Switzerland) and concentration was determined by interpolation of a simultaneously prepared synthetic GFP standard curve (2 pg/mL – 1200 pg/ml). Mass concentration was adjusted for the increased molecular mass of H2B-EGFP (~45 kDa) relative to GFP (~27 kDa).

2.2.7 H2B-EGFP copy number determination

To determine copy number, all H2B-EGFP clones and H1299 WT cells were repeatedly counted (n = 5) by haemocytometer prior to splitting into aliquots and lysis by incubation with ELISA 1X cell extraction buffer PTR (Abcam, Cambridge, UK) on ice for 20 min, followed by clarification by centrifugation (16,000 x g, 20 min). Lysed cell aliquots were prepared in five different concentrations, ranging from 2.0 x 10^5 - 3.3 x 10^6 cells/mL. The protein concentration of each prepared lysate was determined by BCA assay. Results of the BCA assay (mg/mL) were combined with the cell counts conducted previously (cells/mL) to calculate the amount of recovered lysate per cell (mg/cell). This value was multiplied by the concentration of H2B-EGFP in lysates of each H2B-EGFP clone determined by ELISA (pg/mg) to give the mass of H2B-EGFP per cell (pg/cell) in each H2B-EGFP clone. The mass of H2B-EGFP per cell was converted to moles/cell by division of the molecular weight of H2B-EGFP (~ 45 kDa), allowing for determination of copy number by multiplication by the Avogadro constant (6.02 x 10^{23}).

2.2.7 Hybridoma cell culture

The GFP-G1 hybridoma cell line was acquired from the Developmental Studies Hybridoma Bank (DSHB, University of Iowa, USA), which was originally raised against the 1-10 fragment

of superfolder GFP and is validated for use with several GFP derivatives (Yamagata and Sanes, 2012, Donate-Macian et al., 2019). For initiation after thawing, maintenance, and preparation for freezing, the GFP-G1 hybridoma cell line was cultured in Roswell Park Memorial Institute (RPMI) 1640 medium (Sigma-Adrich, MO, USA) containing 10% FBS (Thermo Fisher Scientific, MA, USA), 2 mM L-glutamine, 100 units/mL penicillin, 0.1 mg/mL streptomycin, 50 μg/mL gentamicin. For antibody containing supernatant production, GFP-G1 cell cultures were expanded in CD Hybridoma Medium (Life Technologies) containing 100 units/mL penicillin, 0.1 mg/mL streptomycin, 50 μg/mL gentamicin and were incubated for a further 2 weeks to allow for maximal antibody production. Antibody containing supernatant was clarified by centrifugation (4000 x g, 20 min) and passed through a 0.2 μm filter prior to antibody purification.

2.2.8 Antibody supernatant Protein G purification

Before protein G purification, the pH of clarified hybridoma supernatant was adjusted to pH 7.4. Protein G purification was carried out by fast protein liquid chromatography (FPLC), using an ÄKTA prime plus sytem (GE Healthcare, Uppsala, Sweden) in conjunction with a 1 mL HiTrap protein G purification column (GE Healthcare, Uppsala, Sweden). The protein G column was primed by passing 10 column volumes of binding buffer (20 mM sodium phosphate, pH 7) through the column. The hybridoma supernatant was then passed through the column, followed by washing with 10 column volumes of binding buffer. Antibody bound to the column was eluted into 500 μL fractions with elution buffer (0.1 M glycine, pH 2.7). Fractions were neutralised by addition of 50 μL neutralisation buffer (0.5 M sodium bicarbonate, pH 8.5). The concentration of each fraction was determined by UV absorbance spectrometry 280 nm and pooled together. Pooled fractions were concentrated to 2 mg/mL using a Vivaspin® 50,000 MWCO centrifugal concentrator (Sigma-Adrich, MO, USA) and

buffer exchanged to PBS pH 7.4 using a HiTrap desalting column (Sigma-Adrich, MO, USA). Buffer exchanged antibody was separated into 100 µL (200 µg) aliquots and stored at -20°C for future use.

2.2.8 Statistical analysis

All statistical analysis was carried out using GraphPad Prism v8 (GraphPad Software, CA, USA). Differences between two groups were compared by Welch's t-test. Linear regression with an extra sum of squares F test was used to determine the statistical significance of correlation between H2B-EGFP expression and binding of monoclonal antibody GFP-G1. One-way ANOVA with Tukey's post hoc test, or 2-way ANOVA was used to compare grouped data to compare individual group means, as appropriate. All data was collected at least in triplicate and presented as mean ± one standard deviation unless otherwise stated.

2.3 Results

2.3.1 Validation of transient expression of H2B-EGFP expression system

In order to generate a nucleus-bound GFP model system, I used the H2B-GFP plasmid (Addgene: #11680) (**Figure 2.1**). This plasmid encodes a fusion protein consisting of the enhanced GFP (EGFP) variant of GFP tagged at the N terminus with the histone protein 2B (H2B). This expression system was selected as it has been reliably used in multiple applications for imaging chromosomal dynamics, thus making H2B-EGFP a good candidate for a nucleus bound GFP-based model system. H1299 lung adenocarcinoma cells were selected for transfection as they have been used extensively in oncology research and are amenable to transfection.

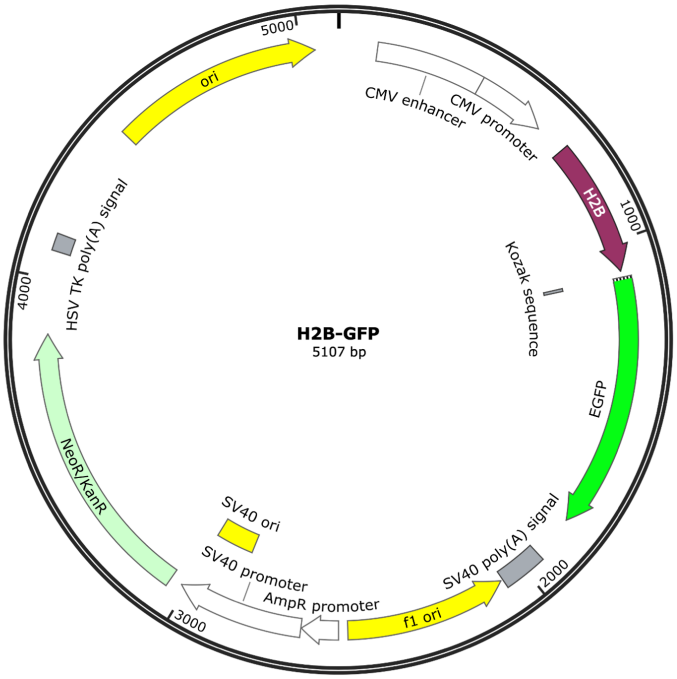


Figure 2.1) Vector map of plasmid H2B-GFP. (Addgene #11680), including H2B-EGFP fusion protein and a synthetic neomycin/G418 resistance gene.

Before attempting to establish a stable expression of H2B-EGFP, conditions were optimised for transient transfection of H1299 cells with the H2B-GFP plasmid. The efficacy of transfection and expression of H2B-EGFP was determined by flow cytometry alongside immunofluorescent microscopy. Analysis by flow cytometry showed a 370-fold increase in fluorescence intensity of the BL1 channel, corresponding to H2B-EGFP fluorescence, 48 hours after transient transfection with the H2B-GFP plasmid (**Figure 2.2A & 2.2B**). Meanwhile, immunofluorescence microscopy demonstrated that H2B-EGFP was restricted to the cell nucleus (**Figure 2.2C**).

2.3.2 Establishment of stably transfected H2B-EGFP cell population

Once conditions were optimised for transfection of H1299 cells with plasmid H2B-GFP, a stably transfected H2B-EGFP expressing cell population was generated (**Figure 2.3A**). In order to select monoclonal cell lines expressing different levels of H2B-EGFP, the transfected

cell population were sorted by FACS and plated individually, selecting 96 cells each from 6 groups of cells expressing increasing levels of H2B-EGFP (**Figure 2.3A & 2.3B**).

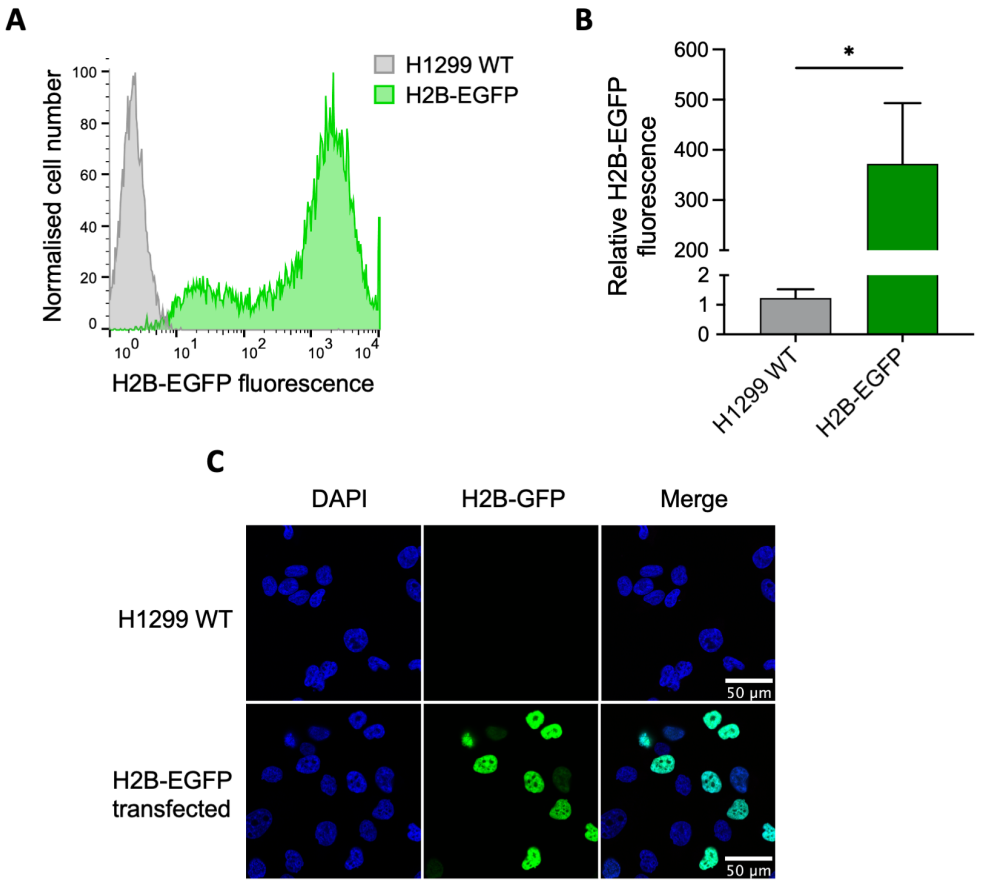


Figure 2.2) Transient expression of H2B-EGFP in H1299 cells. A) Histogram showing expression of H2B-EGFP after transient transfection of H2B-GFP plasmid. **B)** Comparison of geometric mean fluorescence between H1299 WT and H1299 cells expressing H2B-EGFP. Bars represent mean ± SD, * = $P < 0.05$, n = 3. **C)** Confocal immunofluorescence microscopy showing localisation of H2B-EGFP in the cell nucleus (DAPI stain).

2.3.3 Selection and evaluation of H2B-EGFP clone cell lines.

From the collection of monoclonal cell populations, 18 clones were selected for expansion, based on cell growth under G418 antibiotic selection (800 µg/mL) and H2B-EGFP expression, detected by fluorescence microscopy. To determine which clones would be suited for further

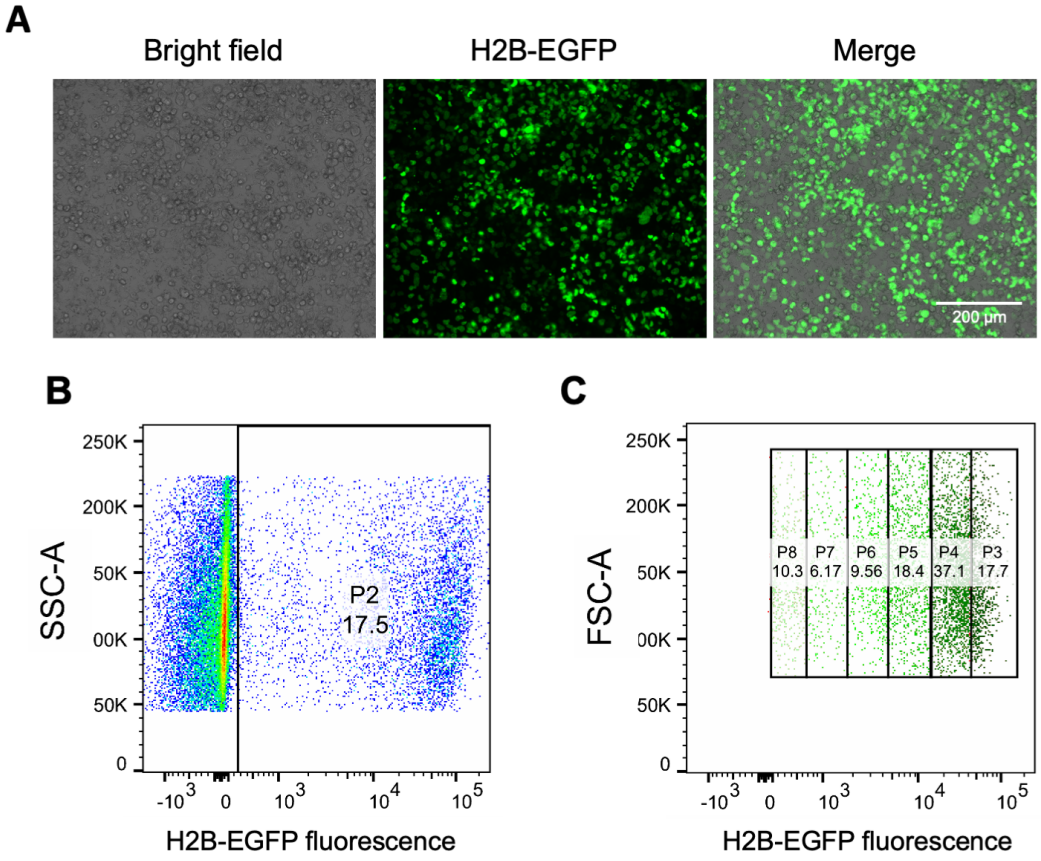


Figure 2.3) Stable transfection and selection of H1299 cells with H2B-EGFP. A) Fluorescence microscopy showing H1299 cells expressing H2B-EGFP after six passages under antibiotic selection (800 µg/mL G418). **B**) Flow cytometry of H1299 cells after six passages under antibiotic selection (800 µg/mL G418) post transfection with H2B-GFP plasmid. **C**) Selection and sorting of H2B-EGFP expressing H1299 cells prior to clonal expansion.

research, flow cytometry was used to evaluate both the level of H2B-EGFP expression and the proportion of cells in each clonal population expressing H2B-EGFP (**Figure 2.4A-C**). From the range of clones, H2B-EGFP 45, 56, 61 and 62 were selected for future work (highlighted in green). These clones were selected as collectively they offered a broad range of expression levels with at least 90% H2B-EGFP positive cells.

Further validation of H2B-EGFP expression across the selected cell lines was carried out by western blot (**Figure 2.5A**) and immunofluorescence microscopy (**Figure 2.5B**). The level of

H2B-EGFP expression per cell within each clone was additionally quantified by ELISA, which ranged from 1.8 x 10^5 to 1.1 x 10^6 copies/cell (**Figure 2.5C**).

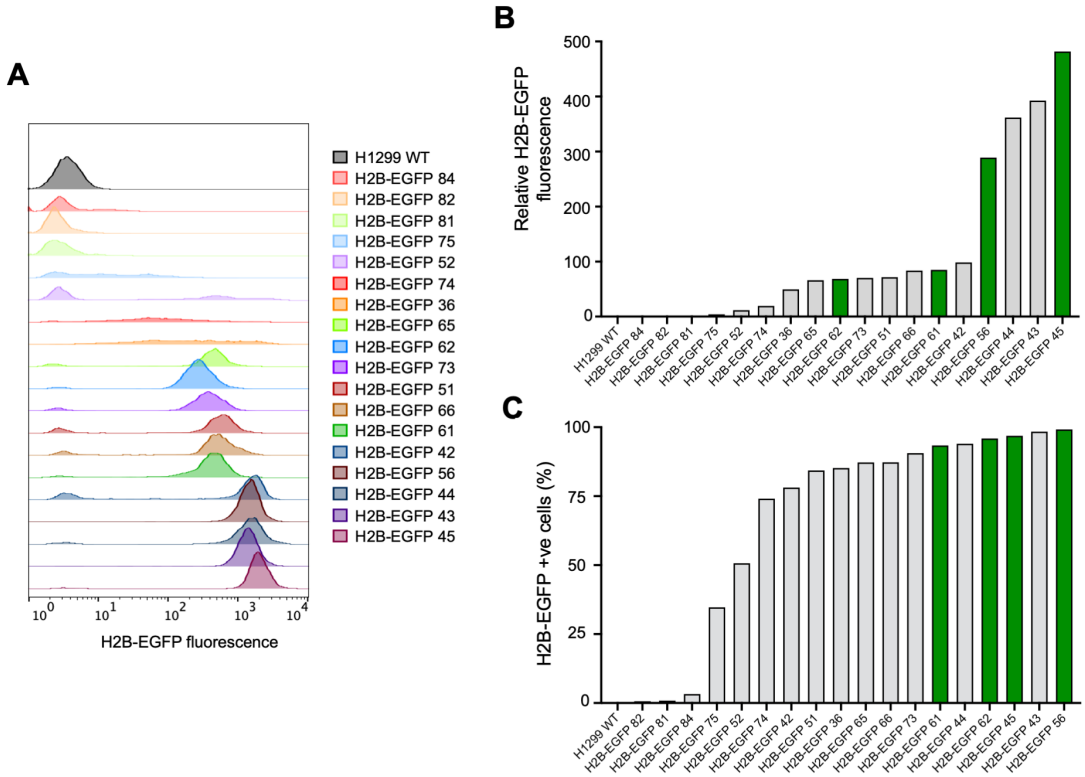


Figure 2.4) Selection of H2B-EGFP expressing clones. A) Flow cytometry analysis of H2B-EGFP expression of clonal populations after expansion under antibiotic selection (800 µg/mL G418). **B**) Comparison of H2B-EGFP geometric mean fluorescence intensity across the clonal population, with selected clones highlighted in green. **C**) Proportion of EGFP positive cells within each clonal population, with selected populations highlighted in green.

2.3.4 Expression stability of H2B-EGFP clones

To evaluate H2B-EGFP expression stability over time, without antibiotic selection, each of the selected H2B-EGFP clone cell lines were cultured for 18 passages (six weeks) in complete culture medium, without G418 antibiotic compound. H2B-EGFP expression was then assessed by flow cytometry and compared to freshly thawed stock (**Figure 2.6A**). Clones H2B-EGFP

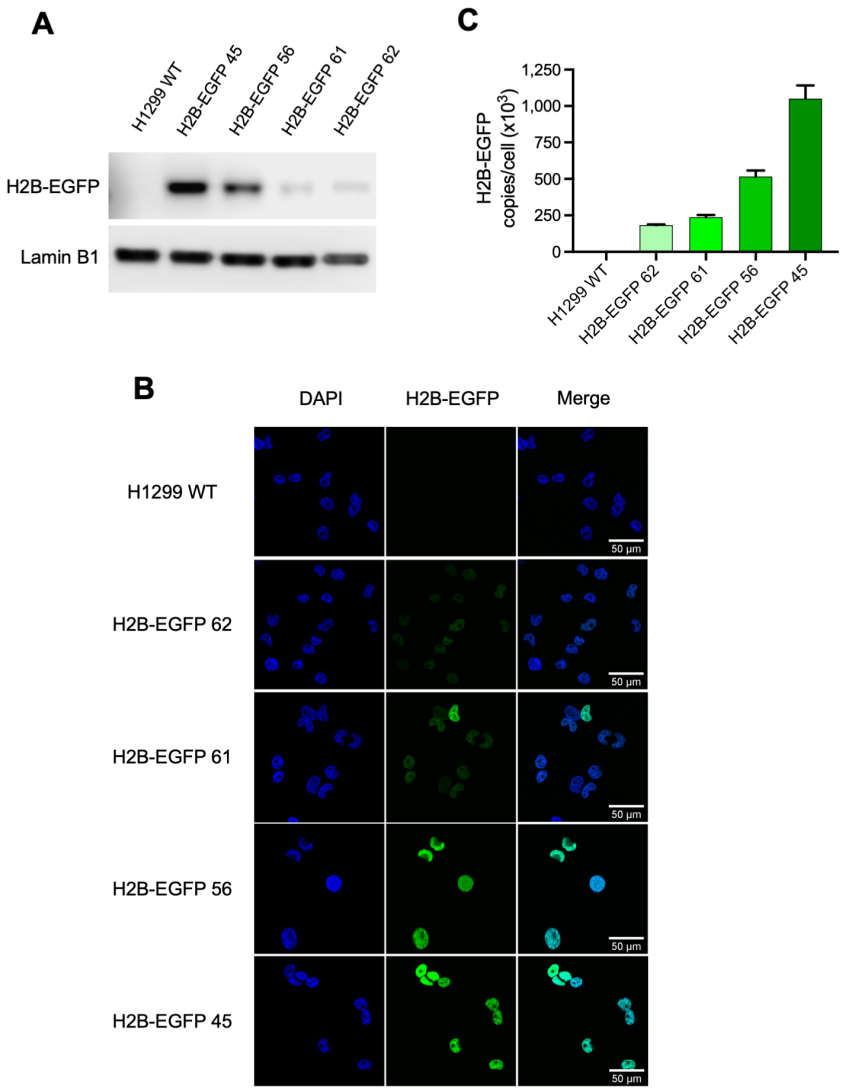


Figure 2.5) Validation of stable H2B-EGFP expression in H1299 clones. A) Western blot validation of H2B-EGFP expression in selected H2B-EGFP expressing cell line clones, relative to WT H1299 cells. Bars represent mean ± SD, n = 3. **B**) Immunofluorescence microscopy showing both extent of expression of H2B-EGFP and co-localisation with the nucleus (DAPI stain) in selected H1299 clone cell lines. **C**) ELISA-based quantification of H2B-EGFP expression (copies/cell) in each selected H2B-EGFP clone.

45 and 62 remained highly stable with a 2.5% and 3.7% reduction in H2B-EGFP positive cells after 6 weeks of passaging without G418 selection (**Figure 2.6B**). However, clones H2B-EGFP 56 and 61 were less stable, H2B-EGFP positive cells reduced by 24.0% and 26.2% respectively.

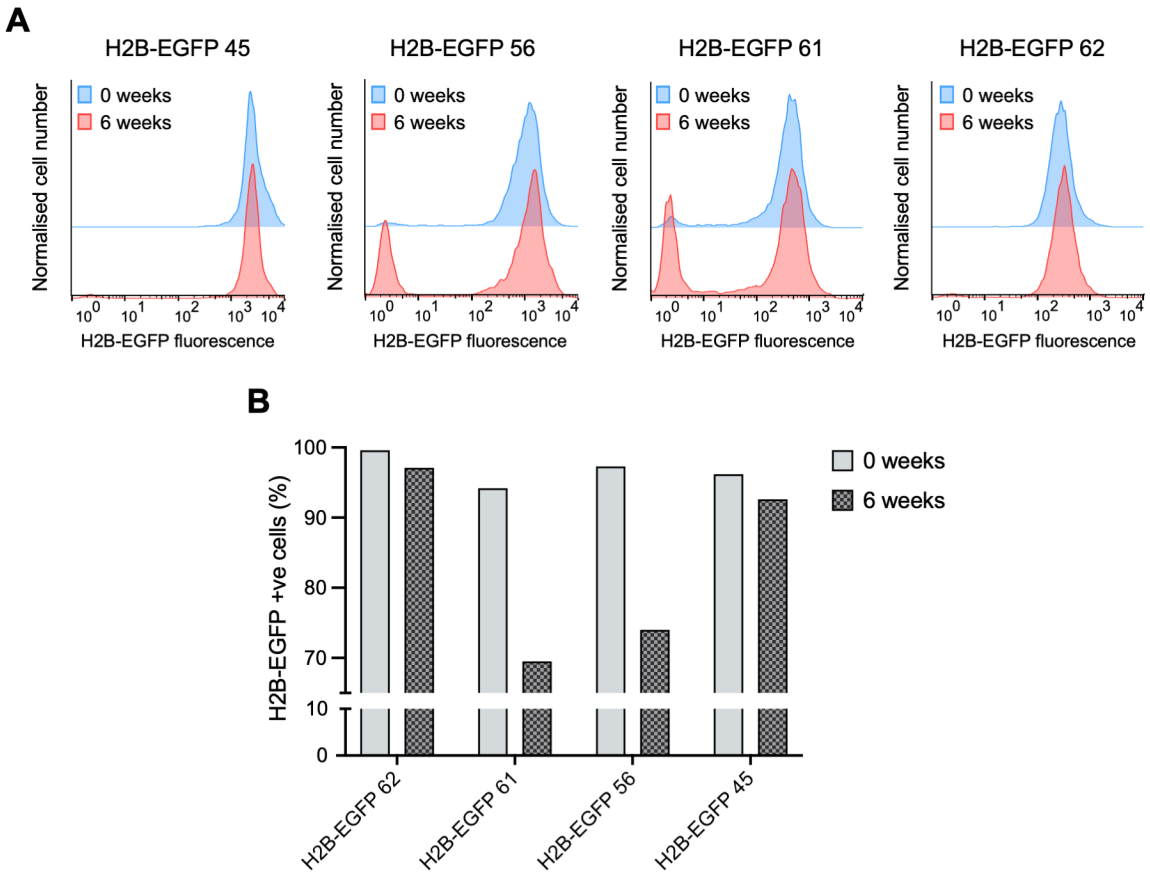


Figure 2.6) Stability of H2B-EGFP expression in selected clone cell lines. **A**) Histograms of flow cytometry analysis showing H2B-EGFP fluorescence of selected H2B-EGFP clone cell lines before and after 6 weeks (18 passages) of culture in complete culture medium, without G418 antibiotic. **B**) Complementary bar chart showing % GFP positive cells before and after six weeks of antibiotic-free culture.

2.3.5 Validation and evaluation of murine monoclonal antibody GFP-G1

To complement the H2B-EGFP model system, the anti-GFP murine monoclonal antibody GFP-G1 was characterised initially with flow cytometry, which showed a 9.7-fold increase in fluorescence between WT H1299 cells and H2B-EGFP 45 cell line (**Figure 2.7A**, $P < 0.001$). Furthermore, when GFP-G1 binding was tested across each H2B-EGFP clone cell line, GFP-G1 uptake correlated with increasing H2B-EGFP expression, as measured previously by ELISA (**Figure 2.7B**, r = 0.87, $P < 0.001$).

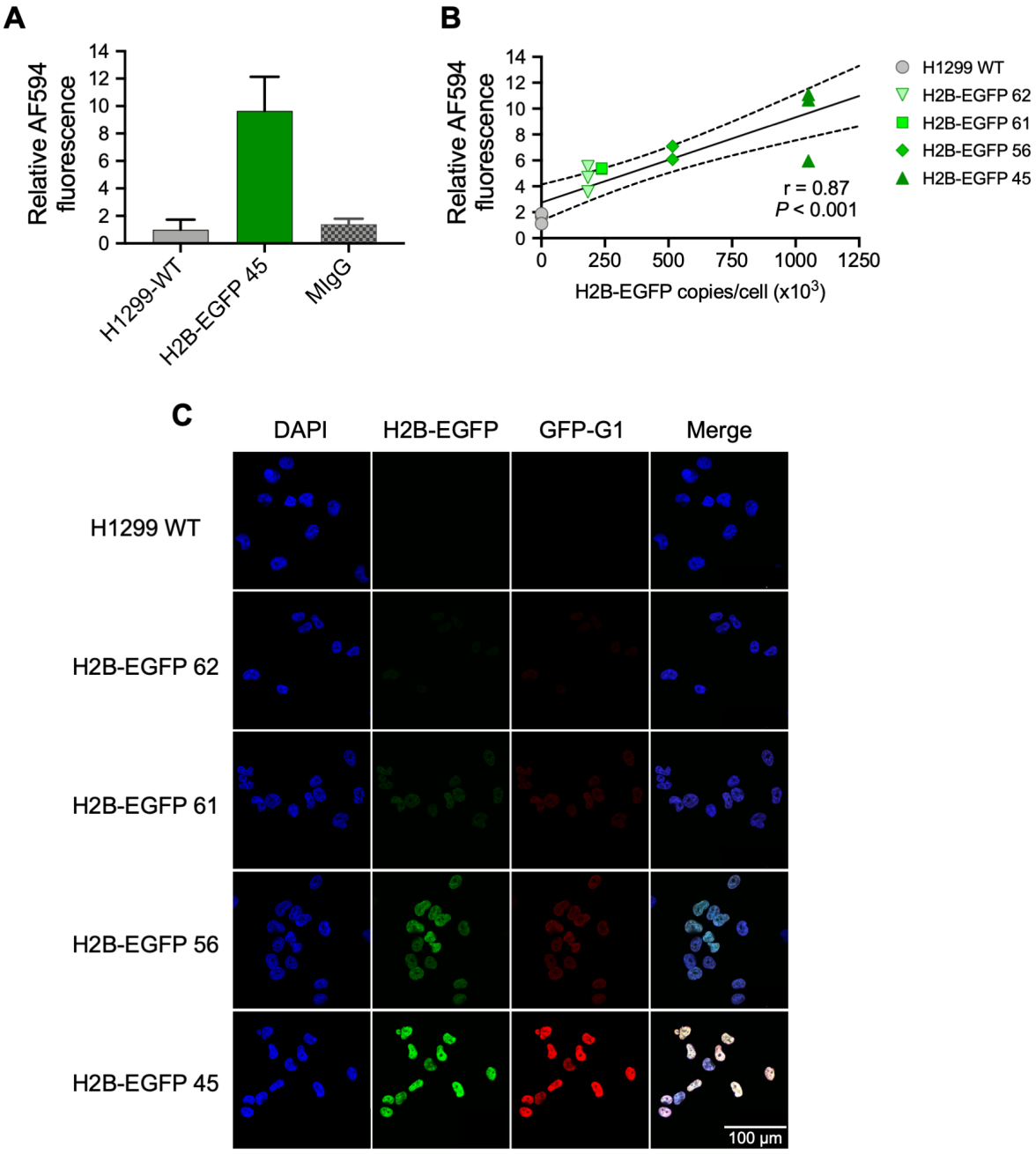


Figure 2.7) Validation of monoclonal antibody GFP-G1. A) Flow cytometry comparison of monoclonal antibody GFP-G1 binding between wild type H1299 WT and clone H2B-EGFP 45 along with isotype control (MIgG) binding to H2B-EGFP 45. Bars represent mean ± SD. **B)** Flow cytometry data showing binding of monoclonal antibody GFP-G1 with increasing expression of H2B-EGFP, dotted lines represent 95% confidence intervals. **C)** Immunofluorescence microscopy showing binding and distribution of monoclonal antibody GFP-G1 with increasing expression of H2B-EGFP.

To further validate the specificity of GFP-G1, immunofluorescence microscopy was used to determine the cellular location of GFP-G1 binding, which showed a strong correlation between H2B-EGFP, GFP-G1, and DAPI stain (**Figure 7C**). Finally, a flow cytometry-based saturation binding assay using cell clone H2B-EGFP 45 demonstrated that the dissociation constant (K_D) of GFP-G1 for H2B-EGFP was 5.1 ± 5 nM (**Figures 8A, 8B**).

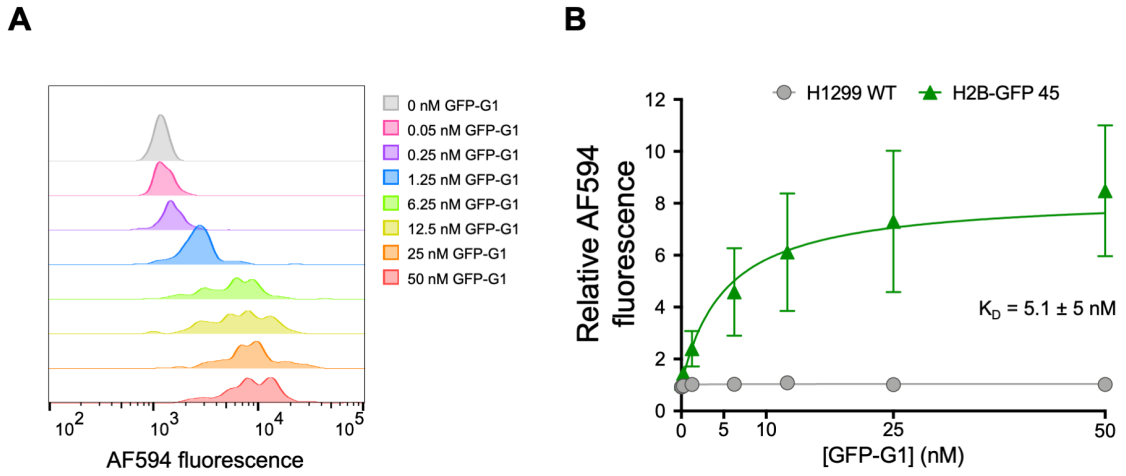


Figure 2.8) Flow cytometry-based affinity binding assay of antibody GFP-G1. A) Staggered histograms showing the effect of increasing concentration of monoclonal antibody GFP-G1 on uptake of GFP-G1 in fixed and permeabilised H2B-EGFP 45 cells. **B)** Affinity binding curve estimated the affinity (K_D) of monoclonal antibody GFP-G1 for H2B-EGFP to be 5.1 ± 5 nM. Modelled using a non-linear regression model with GraphPad Prism v8, assuming one binding site and background signal constrained to 1. Error bars represent 95% confidence intervals, n = 3.

Discussion

Antibody- or antibody fragment- based molecular imaging is an exciting and rapidly expanding field of research within clinical oncology, with an ever-increasing repertoire of novel targets, probe designs and radioisotope chemistries, which can be fine-tuned towards specific tasks (Freise and Wu, 2015). The incorporation of cell penetrating peptides, such as TAT, to facilitate

imaging of intranuclear epitopes would significantly increase the range of potential applications of antibody- or antibody fragment-based molecular imaging. Despite several studies providing a tantalising glimpse into the possibilities of IgG-TAT based intranuclear imaging, a thorough analysis to evaluate the potential of this technology has yet to be undertaken.

When evaluating a novel technology, it is important to employ a well characterised model system that will ultimately allow the researcher to draw valid conclusions on the efficacy of the technology. Although a multitude of factors will contribute towards imaging effectiveness in *vivo*, these can be reduced to three critical factors (Reddy and Robinson, 2010). First is target abundance and availability: the target abundance must be suitably high to generate a contrast in the tissue of interest, whilst also being presented in an orientation and sub-cellular location which will allow interaction with the imaging probe. Secondly is probe specificity and affinity; an effective probe will bind exclusively to the target epitope with high enough affinity to achieve a detectable signal at the concentration of probe applied to the desired tissue. Finally, the pharmacokinetic and clearance characteristics *in vivo* must allow for an adequate concentration of the imaging probe to reach the target. The purpose of this chapter was to develop a model system to minimise the experimental variation of the first two factors, which would allow for a more robust analysis of the limitations of IgG-TAT based intranuclear imaging and in particular the lower target abundance detection threshold.

H2B-EGFP was selected as a model target system for several reasons, firstly the plasmid H2B-GFP is well characterised as a reliable expression system for stable transfection of a nucleus bound variant of GFP (Kanda et al., 1998). Furthermore, the fluorescent qualities of H2B-EGFP allows for direct observation of target presence, thereby making the process of monitoring the efficiency of transfection and selection of stable clone cell lines significantly more practical (**Figure 2.2 & 2.3**). From the pool of stably transfected cells, four clones were

selected to both maximise the range of H2B-EGFP expression whilst utilising those with the highest stability of H2B-EGFP expression (**Figure 2.4**).

One of the principal objectives of this project was to determine the lower target abundance threshold. The expression level of the clone cell line with lowest expression of H2B-EGFP (H2B-EGFP 62) was shown to be 1.8 x 10^5 copies/cell (**Figure 2.5B**). High throughput mass spectrometry analysis of He-La and U2OS cells have approximated that only a fifth of cellular proteins are expressed at an equal or greater extent than H2B-EGFP in clone H2B-EGFP 62 (Beck et al., 2011, Bekker-Jensen et al., 2017). This, however, may not be representative as these reports do not account for fluctuation of abundance of select proteins throughout the cell cycle or indeed changes in protein (over)expression in a pathological or pharmacologically altered state. As the method of stable transfection of plasmid H2B-GFP relied on antibiotic selection, a H2B-EGFP clone cell line expressing H2B-EGFP at a level lower than that of H2B-EGFP 62 may not have been feasible as this clone would not be able to pass through antibiotic selection.

Another important consideration when evaluating the H2B-EGFP model cell lines was H2B-EGFP expression stability. Although H2B-EGFP expression could be maintained by antibiotic selection for studies *in vitro*, antibiotic selection cannot be carried out an *in vivo* xenograft model. Whilst clones H2B-EGFP 45 and 62 demonstrated good expression stability without antibiotic selection (**Figure 2.6**), H2B-EGFP 56 and 61 showed a reduction in H2B-EGFP expression that must be taken into account when used in an *in vivo* model. In future research, it would be advantageous to utilise an alternative stable transfection method, such as a CRISPR/Cas9-mediated introduction of H2B-EGFP into a host cell line using a lentiviral vector (Banan, 2020).

In addition to target abundance and presentation, imaging probe affinity must also be considered when choosing to develop a molecular imaging device. The murine monoclonal

antibody GFP-G1 was selected as a complementary antibody to the H2B-EGFP expression model system as the original hybridoma cell line was readily available, thus allowing for production and purification on the scale required for subsequent bioconjugation optimisation and radioassays (Yamagata and Sanes, 2012). Furthermore, flow cytometry and immunofluorescence microscopy both demonstrated that GFP-G1 was highly selective for H2B-EGFP, showing little detectable non-specific binding (**Figure 2.7**). Affinity binding assays also demonstrated a dissociation constant (K_D) for GFP-G1 to be 5.1 ± 5 nM (**Figure 2.8**), which is comparable to antibodies currently in clinical use, such as Trastuzumab (5.0 nM) (De Lorenzo et al., 2005). Whilst the affinity of GFP-G1 is adequate for this application, many antibodies are capable of far greater affinities, some with dissociation constants within the sub picomolar range, future research could investigate the effect of using alternative anti-GFP antibodies, with higher or lower affinities, on anti-GFP-TAT RIC uptake (Vaughan et al., 1996).

In summary, this chapter describes the development of a model target and complementary antibody system, which is suitable for use to determine the effect on target abundance on the efficacy of IgG-TAT based imaging of intranuclear epitopes.

Chapter 3

Design and evaluation of a novel conjugation approach to produce IgG-TAT based radioimmunoconjugates

3.1 Introduction

Molecular PET/SPECT imaging using antibody- or antibody fragment- based imaging probes, or RICs, has great potential as a highly versatile clinical imaging modality (Freise and Wu, 2015). The ability to add and combine additional functional groups, such as radiometal chelators and cell penetrating peptides (CPPs) allows the researcher, or clinician, to tailor the features of an RIC towards specific applications (Wu, 2014).

Critical to the development of any novel RIC is a conjugation approach that is reliable and does not compromise the stability or binding characteristics of the antibody, or fragment (Dennler et al., 2015). In order to transform a monoclonal antibody into a PET/SPECT RIC capable of engaging intracellular targets, an antibody requires the conjugation of two functional groups, a chelator to carry a radiometal of choice, and a cell penetrating peptide, such as TAT, to increase the efficiency of translocation across cellular membranes (Kersemans et al., 2008). This approach, using IgG-TAT-based RICs for PET/SPECT imaging has been used in previous reports to successfully target several intranuclear proteins, including p21, p27 and γH2AX (Hu et al., 2007, Cornelissen et al., 2009, Knight et al., 2015, Poty et al., 2020).

Traditionally, the conjugation of an IgG-TAT-based RICs for PET/SPECT has been carried out using carbodiimide crosslinking chemistry (Cornelissen et al., 2011) (**Figure 3.1A**). This approach uses a carbodiimide, such as EDC, which reacts with solvent accessible carboxyl groups present on the antibody to form an amine-reactive ester intermediate. Reaction with EDC is often combined with NHS to improve the stability of the intermediate ester, preventing detrimental hydrolysis (Hermanson, 2013). This activated antibody is then reacted with the CPP under neutral conditions, promoting the formation of a peptide bond between the activated groups of the antibody and the N-terminal amino group of the CPP. Once the CPP has been attached, the solvent accessible nucleophilic groups of the antibody are reacted with an amine-

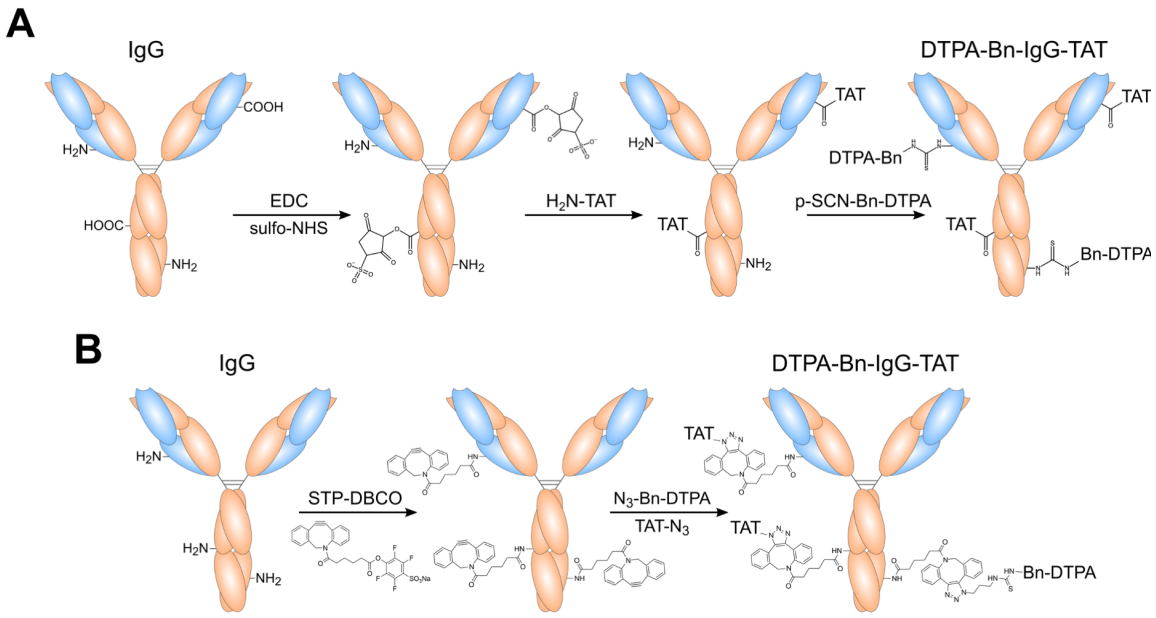


Figure 3.1) Alternative Conjugation strategies for non-site-specific labelling of IgG molecules with radiometal chelator DTPA and CPP TAT. A) Current conventional strategy of labelling, using EDC/NHS mediated crosslinking of IgG with CPP TAT, followed up isothiocyanate driven labelling of primary amines with *p*-SCN-Bn-DTPA. **B)** Alternative conjugation approach, which labels IgG with a strained cyclooctyne (DBCO) for simultaneous SPAAC click chemistry reactions with azide modified derivatives of TAT (TAT-N_3) and DTPA (DTPA-Bn-N_3).

reactive bifunctional chelator, for instance S-2-(4-isothiocyanatobenzyl)-diethylenetriamine pentaacetic acid (*p*-SCN-Bn-DTPA) (Hermanson, 2013).

Whilst this sequential conjugation strategy, henceforth referred to as the EDC/NHS method, has been reliably used to generate a variety of RICs capable of targeting intranuclear epitopes, this approach has several potential drawbacks. Firstly, the EDC mediated crosslinking method is bidirectional, therefore creating the risk of antibody-antibody crosslinking as opposed to antibody-CPP conjugation, potentially negating performance. Also, the sequence of the CPP TAT contains several solvent accessible primary amines, which could react with the amine reactive chelator, possibly altering the structure, charge and therefore the functionality of TAT itself. Another plausible issue with this method is that it involves the reaction of both solvent accessible amines and carboxyl groups, thus increasing the likelihood of modifying a group that is integral to the stability or targeting function of the antibody (Kaur et al., 2015, Wakankar et al., 2010). Finally, there is no simple method of carrying out quality control of reactions within the EDC/NHS method, which would be highly beneficial to the maker of the RIC.

In light of the shortcomings of the EDC/NHS method of producing TAT-IgG based RICs, this project aimed to develop and evaluate a different method of conjugation, which could effectively avoid these issues (**Figure 3.1B**). This new method, henceforth referred to as the DBCO-N_3 method, incorporates the bifunctional conjugation agent, dibenzocyclooctyne-4-sulfo-2,3,5,6-tetrafluorophenol ester (STP-DBCO) (Click Chemistry Tools, AZ, USA), featuring an amine reactive activated ester group (STP Ester), which is used decorate the solvent accessible primary amines on an antibody of choice with a DBCO moiety. DBCO is a highly reactive strained cyclic alkyne, which can be specifically reacted with additional functional groups, such as azide-modified chelators or CPPs that contain an organic azide moiety, via SPAAC (Dommerholt et al., 2016). In combination with the bifunctional STP-DBCO conjugation agent, I deployed azide-modified derivatives of the CPP TAT, TAT-

azidohomoalanine (TAT-N_3, Cambridge Peptides, Cambridge, UK), and the chelator DTPA (N_3-Bn-DTPA), which was synthesised by Deborah Sneddon (Department of Chemistry, University of Oxford, Oxford, UK).

In this thesis, I will initially optimise the conditions for the preparation of an IgG-TAT based RIC using the DCBO-N_3 conjugation method, then the resulting RIC will be compared *in vitro* to an alternative IgG-TAT RIC prepared using the EDC/NHS approach. To make a valid comparison, the previously validated murine monoclonal antibody GFP-G1 will be conjugated and evaluated for cell uptake into lung adenocarcinoma H1299 cells, stably transfected with the nucleus bound fusion protein histone-2B-enhanced green fluorescent protein (H2B-EGFP, see chapter 2). Ultimately, this chapter will demonstrate the development, optimisation and evaluation of a novel method of IgG-TAT conjugation, providing a new standard method of producing IgG-TAT based RICs.

3.2 Materials and methods

3.2.1 Preparation of antibody conjugates by EDC/NHS crosslinking method

250 μg of polyclonal or monoclonal antibody was buffer exchanged to 0.1 M MES pH 6 and concentrated to 25 μM. The solvent accessible carboxyl groups of the desired antibody were activated for reaction with primary amines by addition of a 40-fold molar excess of 1-ethyl-3-(3- dimethylaminopropyl)carbodiimide hydrochloride (EDC) for 15 min at room temperature. A 100-fold excess of *N*-hydroxysulfosuccinimide sodium salt (sulfo-NHS) was simultaneously added for increased stability of the O-acylisourea intermediate. Excess EDC/NHS was removed and MES buffer was exchanged with PBS by centrifugal filtration using a Zeba Spin desalting column (7 K MWCO, 0.5 mL) (Thermo Scientific, MA, USA). Antibody concentration was determined by NanoDrop (Thermo Fisher Scientific) before incubation with

a 10-fold molar excess of the peptide TAT for 2 h. Excess TAT was removed and PBS buffer was exchanged with 0.1 M sodium bicarbonate (pH 8.5) by centrifugal filtration. TAT conjugated antibodies were then reacted with a 20-fold molar excess of S-2-(4-Isothiocyanatobenzyl)-diethylenetriamine pentaacetic acid (*p*SCN-Bn-DTPA) (Macrocyclics, TX, USA) for 1 h at 37°C before centrifugal filtration to remove unconjugated *p*SCN-Bn-DTPA and exchange buffer to 0.5 M sodium citrate pH 5.5 for subsequent radiolabelling with ^{111}In. The concentration of DTPA-Bn-IgG-TAT was determined by nanodrop and adjusted to a final concentration of 6.8 mM.

3.2.2 Preparation of antibody conjugates by DBCO-N_3 click chemistry method

Bioconjugation of antibodies with cell penetrating peptide TAT and metal ion chelating agent DTPA was also carried out using SPAAC in a non-site-specific manner. The antibody of choice was buffer exchanged in 0.1 M $NaHCO_3$ pH 8.5, concentrated to 25 µM and reacted with a seven-fold molar excess of dibenzocyclooctyne-4-sulfo-2,3,5,6-tetrafluorophenyl (DBCO-STP) (Click Chemistry Tools) dissolved in dimethyl sulfoxide (DMSO) at room temperature for 4 h. The antibody-DBCO conjugate was purified and buffer exchanged to PBS by centrifugal filtration using a Zeba Spin desalting column (7 K MWCO, 0.5 mL, Thermo Scientific, MA, USA). The amount of DBCO tags conjugated to the antibody was determined by absorbance spectroscopy at 280 and 309 nm, with a DBCO:antibody ratio of 5:1. The antibody-DBCO conjugate, at approximately 10 µM, was then reacted with a 2-fold molar equivalent relative to DBCO of 3.4 mM N_3-Bn-DTPA dissolved in PBS + 20% DMSO (synthesised by Deborah Sneddon, Department of Chemistry, University of Oxford, UK), and, concurrently, a 1-fold molar equivalent, also relative to DBCO, of 1 mM azide-tagged cell penetrating peptide TAT-azidohomoalanine (TAT-N_3, GRKKRRQRRRPPQGYG-hA(N_3) dissolved in PBS (Cambridge Peptides, Birmingham, UK) at 4°C for 16 h. The antibody

conjugate was purified, and buffer exchanged to 0.5 M sodium citrate pH 5.4 to remove unreacted products by centrifugal filtration. The completion of the conjugation reaction was confirmed by the reduction of UV absorption spectrometry at 309 nm to background level. After purification, the concentration of DTPA-Bn-IgG-TAT was determined by nanodrop and adjusted to a final concentration of 6.8 mM.

3.2.3 Radiolabelling DTPA-Bn-IgG-TAT conjugates with $^{111}InCl_3$

Radiolabelling of immunoconjugates was carried out by addition of $^{111}InCl_3$ (Perkin Elmer, MA, USA). Aliquots of 150 µg of DTPA-IgG-TAT conjugate (1 mg/mL in 0.5 M sodium citrate pH 5.4) were reacted with $^{111}InCl_3$ (1 MBq/µg of antibody) in 0.5 M sodium citrate buffer pH 5.4 for 1 h at room temperature. Radiolabelling yield was confirmed by instant thin layer chromatography (iTLC) to be greater than 95%. The resulting RIC was buffer exchanged to PBS to remove any free $^{111}In^{3+}$ prior to subsequent studies.

3.2.4 Stability assay

GFP-G1 based RICs, radiolabelled with ^{111}In, were tested for stability in both PBS and mouse serum (Sigma, Dorset, UK). RICs were diluted to 0.25 µg/ml in the chosen solution and incubated at 37°C. Samples were taken at 24, 48 and 72 hours from the onset of incubation. For samples incubated in PBS, the extent of ^{111}In dissociation from each RIC was determined by iTLC and calculated as a percentage of total radioactivity detected. Samples that were incubated in mouse serum were analysed by SDS-PAGE to determine whether ^{111}In had undergone transchelation to another protein present in mouse serum.

3.2.5 Cell-free radioimmunoassay (RIA)

Lyophilised GFP protein (Insight Biotechnology, Middlesex, UK), was reconstituted to 2 µg/ml in radioimmunoassay (RIA) coating buffer (0.2 M sodium bicarbonate pH 9.5). RIA plates (96 well) were covered with 50 µl RIA assay coating buffer with 2 µg/ml GFP and incubated for 16 h at 4°C. Coating buffer was then removed, and coated wells were washed with 250 µl RIA washing buffer (PBS + 0.05% Tween®-20) three times for 5 min at RT with gentle agitation. Washed plates were blocked by incubation with 250 µl RIA blocking buffer (RIA wash buffer + 2% bovine serum albumen (BSA)) for 60 min at RT, followed by a further three washes as previously described. Antibody/RIC combination solutions were prepared at the desired concentrations in RIA blocking buffer and added to GFP coated wells and incubated for 1 h at RT. Antibody combination solutions were removed and collected, followed by washing as previously described, which was also collected when removed. Bound antibodies/RICs were removed and collected following addition of RIA stripping buffer (0.1 M sodium hydroxide) for 15 min, which was repeated twice more to ensure maximal antibody/RIC recovery. The amount of ^{111}In which was bound to each RIA plate well was determined using the Wizard^2 2480 automated gamma counter (Perkin Elmer, MA, USA), which was calculated as percentage of total ^{111}In added, normalised to a control group without a blocking agent.

3.2.6 Cell culture

Human lung adenocarcinoma H1299 cells (ATCC) were cultured in DMEM (Sigma-Aldrich, MO, USA), supplemented with 10% foetal bovine serum (Thermo Fisher Scientific, MA, USA), 2 mM L-glutamine, 100 units/mL penicillin, and 0.1 mg/mL streptomycin and maintained in a 5% CO_2 humidified atmosphere at 37°C. Cells were tested and authenticated by the providers. The cumulative length of culture was less than 6 months following retrieval

from liquid nitrogen storage. Cells were tested for the absence of mycoplasma at regular intervals. Cells stably transfected with H2B-EGFP plasmid were cultured with 50 μg/mL G418/geneticin to promote stability of transfection. Cells were harvested and passaged as required using trypsin-EDTA solution.

3.2.7 Colony formation assay

Aliquots of 2.5 x 10^2 cells were plated in 6 well plates with complete culture medium and incubated overnight at 37°C with 5% CO_2. Culture medium was removed, and cells washed with PBS before addition of fresh culture medium containing either ^{111}In-DTPA-GFP-G1-TAT (1.5 nM, 1 MBq/μg), ^{111}In-DTPA-GFP-G1 without TAT (1.5 nM, 1 MBq/μg), or no RIC, followed by incubation at 37°C for a further 60 min. Supernatant containing unbound radiolabelled compound was removed and cells were washed twice with PBS before addition of fresh culture medium. To allow for colony formation, cells were incubated for a further 14 days without disruption. Cells were then washed with PBS and stained with crystal violet biological stain (Sigma-Aldrich, MO, USA) at room temperature (RT) for 24 h. Stained cells were washed with ddH_2O and dried before colonies were imaged and counted using the GelCount™ colony counter (Oxford Optronics, Oxfordshire, UK).

3.2.8 Cell uptake study

Aliquots of 8 x 10^4 cells/well were plated in a 24 well plate cell culture dishes and allowed to adhere for 16 h. Culture medium was removed, and cells washed with PBS before addition of fresh culture medium containing ^{111}In-DTPA-GFP-G1-TAT (1.5 nM, 1 MBq/μg) and incubated at 37°C for a further 60 min. Supernatant containing unbound radiolabelled compound was collected, cells were washed twice with PBS before cells were washed for 5 min on ice in 0.1 M glycine pH 2.5 solution to remove membrane-bound radiolabelled antibody

conjugate. Finally, cells were lysed by addition of 0.1 M NaOH, and cell-associated compound was collected. The amount of ^{111}In within each fraction was determined using the Wizard^2 2480 automated gamma counter (Perkin Elmer, MA, USA), which was used to calculate the percentage of cell-associated radioactivity.

3.3 Results

3.3.1 Optimisation of antibody conjugation with STP-DBCO linker

The initial stages of this project involved optimisation of the conditions, primarily the stoichiometry for labelling antibodies with the DBCO linker moiety. Starting with a non-specific rabbit polyclonal antibody (RIgG), increasing amounts of STP-DBCO were reacted with the antibody. As unreacted DBCO absorbs UV light (A_{309}), the molar ratio of DBCO linkers to RIgG molecule could be determined (**Figure 3.2A**). To further validate the conjugation method, the DBCO modified RIgG was reacted with an azide tagged fluorophore, sufo-Cy5-N_3 (A_{647}). Increasing STP-DBCO concentration correlated almost linearly with conjugated DBCO-RIgG ratio until approximately 4 molar equivalents of STP-DBCO/RIgG. Subsequent reaction with sulfo-Cy5-N_3 showed a similar trend, however the sulfo-Cy5-RIgG ratio was approximately 50% of the recorded DBCO-RIgG ratio for the same fold excess of STP within the initial reaction. From this initial optimisation, it was decided that a seven-fold excess of STP-DBCO relative to antibody would be optimal to ensure enough DBCO linkers had been added for addition of at least two functional groups whilst minimising the chances of perturbing the stability or binding properties of a suitable antibody. Next, RIgG was reacted with a 7-fold excess of STP-DBCO before reaction with increasing concentrations of sulfo-Cy5-N_3, which showed a high level of efficiency with maximal Sulfo-Cy5-RIgG ratios

achieved at approximately one molar equivalent of sulfo-Cy5-N_3 relative to DBCO linkers (**Figure 3.2B**).

3.3.2 Optimisation of TAT-N_3 and DTPA-Bn-N_3 conjugation

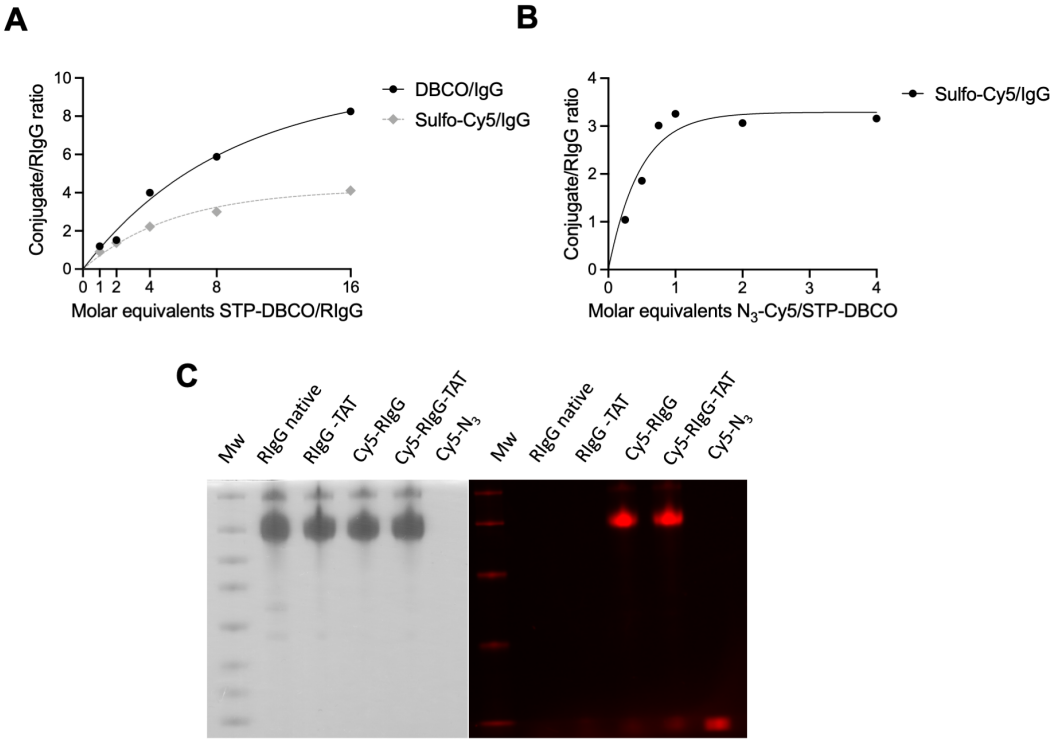


Figure 3.2) Initial optimisation of DBCO-N_3 based click conjugation. A) Ultraviolet-visible (UV-vis) spectroscopy-based quantification, showing the difference in conjugate/RIgG ratio of both DBCO handle (A_{309}) and sulfo-Cy5 fluorophore (A_{647}) conjugation with increasing input of STP-DBCO in the initial activation reaction. **B)** UV-vis quantification showing change CAR with increasing sulfo-Cy5-N_3 input into a reaction with RIgG previously reacted with a 7-fold molar excess of STP-DBCO. **C)** SDS page of RIgG labelled with combinations of sulfo-Cy5-N_3 (Cy5) and an azide modified derivative of CPP TAT (TAT-N_3)

For evaluation of the conjugation of a targeted monoclonal antibody with azide modified derivatives of CPP TAT (TAT-N_3) and chelator DTPA (DTPA-Bn-N_3), the conditions which had been optimised for labelling RIgG with fluorophore sulfo-Cy5 were used as the basis for

a conjugation competition assay. By using sulfo-Cy5 as a detectable marker, I predicted the relative reactivity of TAT-N_3 and chelator DTPA-Bn-N_3 towards a DBCO labelled monoclonal antibody, which would be used to determine the optimum reaction stoichiometry to conjugate each IgG molecule with at least one TAT and one DTPA functional group. The murine monoclonal antibody GFP-G1 (see Chapter 2) was activated with a seven-fold excess of STP-DBCO and then reacted simultaneously with a stoichiometric equivalent of sulfo-Cy5-N_3 (relative to conjugated DBCO linkers) and increasing amounts of either TAT-N_3 or DTPA-Bn-N_3 (**Figure 3.3**). The relative reactivity of TAT-N_3 and DTPA-Bn-N_3 was calculated based on the rate of sulfo-Cy5 displacement, which showed TAT-N_3 was able to displace sulfo-Cy5-N_3 nearly twice as effectively at DTPA-Bn-TAT. Therefore, when performing a simultaneous conjugation, the molar ratios of TAT-N_3 and DTPA used, relative to conjugated DBCO linkers, was 1- and 2-fold respectively.

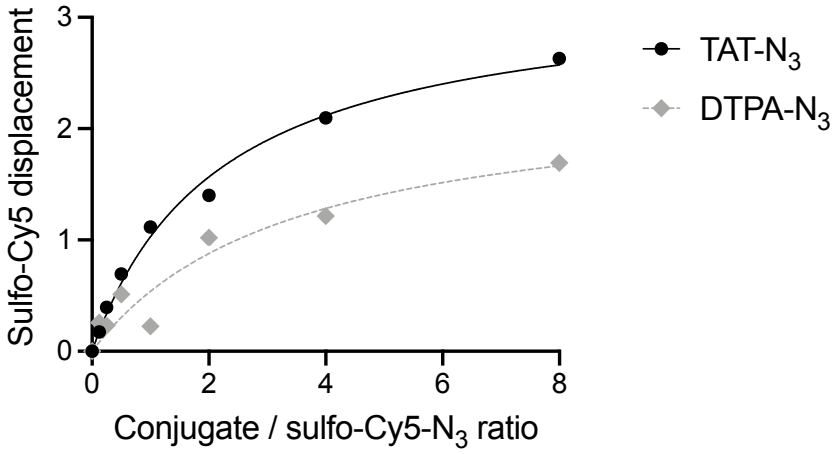


Figure 3.3) Conjugation competition assay. Murine monoclonal antibody was reacted with a seven-fold molar excess of DBCO-STP prior to simultaneous reaction with the azide modified fluorophore sulfo-Cy5-N_3 and increasing amounts of either TAT-N_3 or DTPA-Bn-N_3. The extent of displace sulfo-Cy5 was used to determine optimum stoichiometry for simultaneous reaction of TAT-N3 and DTPA-Bn-N3 with the DBCO-labelled GFP-G1 antibody.

3.3.3 Radiolabelling and stability of DTPA-GFP-G1-TAT RICs

Once stoichiometry conditions were optimised for conjugation of GFP-G1 with TAT-N_3 and DTPA-Bn-N_3 were determined, these parameters were used to produce the GFP targeted RIC DTPA-Bn-GFP-G1-TAT. Prior to evaluation of uptake *in vitro*, DTPA-GFP-G1-TAT was radiolabelled with ^{111}In and tested for radiolabelling stability. For comparison, DTPA-GFP-G1-TAT was prepared using both the novel N_3-DBCO method, the previous standard EDC-NHS crosslinking method, and additionally a DTPA-Bn-GFP-G1 RIC without TAT prepared with an amine-reactive isothiocyanate linked DPTA conjugate (*p*-SCN-Bn-DTPA). Initial radiolabelling efficiency, determined by iTLC, showed all three prepared RICs radiolabelled with at least 95% efficiency (**Figure 3.4A**). Each RIC was incubated at 37°C in both PBS and mouse serum to better resemble an *in vivo* application, with samples taken every 24 hours over a 72-hour period. In PBS, iTLC was used to determine radiolabelling purity, ^{111}In-DTPA-GFP-G1-TAT prepared by the DCBO-N_3 showed the lowest stability with a 72.5% radiolabelling purity after 72 hours, in comparison to 83.4% and 86.2% for the ^{111}In-DTPA-GFP-G1-TAT prepared by the EDC-NHS method and ^{111}In-DTPA-GFP-G1 without TAT respectively (**Figure 3.4B**). However, SDS-PAGE and autography of samples taken from RICs that had been incubated in mouse serum showed relatively no clear signs of either degradation or transchelation of ^{111}In (**Figure 3.4C**).

3.3.4 Comparison of blocking properties of DTPA-GFP-G1-TAT RICs

To investigate the potential effect of TAT conjugation on binding affinity, a cell-free blocking radioimmunoassay (RIA) was conducted. Recombinant purified GFP protein was immobilised onto a RIA assay plate and binding of radiolabelled ^{111}In-DTPA-GFP-G1, without TAT, was assessed with quantities of non-radiolabelled DTPA-GFP-G1-TAT immunoconjugates,

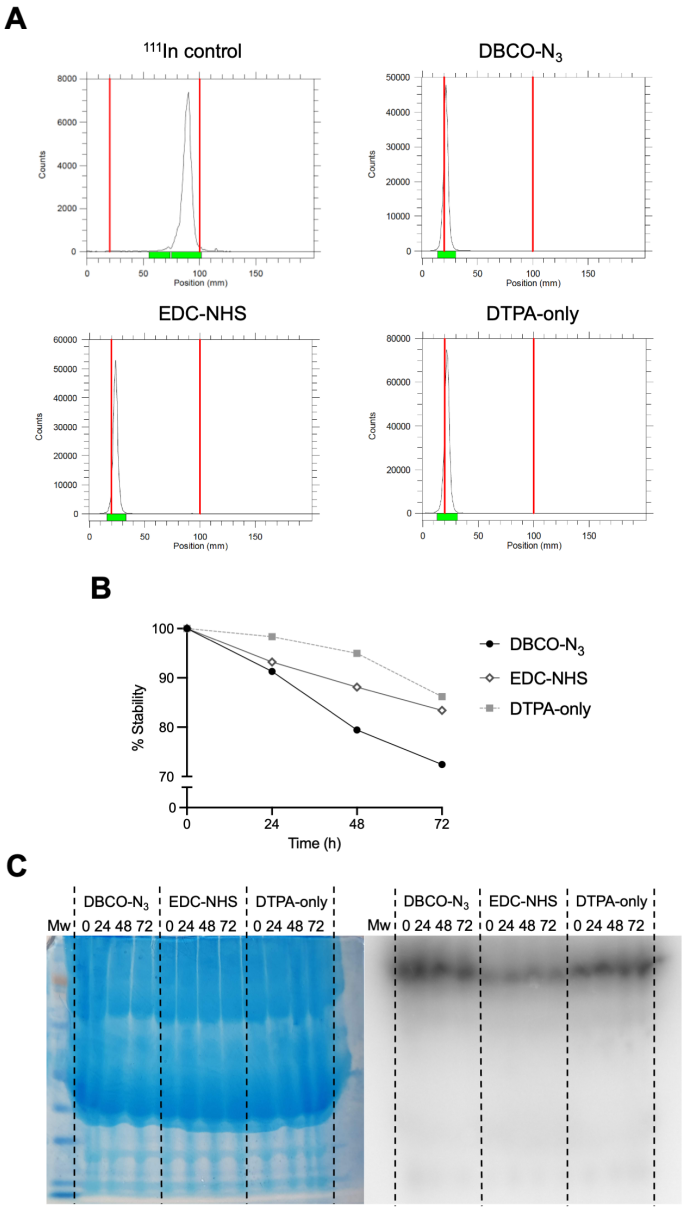


Figure 3.4) Radiolabelling purity and stability of ^{111}In-DTPA-GFP-G1-TAT RICs. **A)** ITLC of ^{111}In-DTPA-GFP-G1-TAT RICs prepared using alternative conjugation strategies. **B)** Summary of reduction in radiolabelling purity of DTPA-Bn-GFP-G1-TAT RICs incubated at 37°C in PBS over a 72-hour period, determined by iTLC. **C)** SDS-PAGE followed by autoradiography showing stability of ^{111}In-DTPA-GFP-G1-TAT RICs incubated at 37°C in mouse serum over a 72-hour period.

including a non-modified, native GFP-G1 antibody (**Figure 3.5**). The RIA demonstrated that there was no statistically significant difference (*P = 0.80*) between the blocking capacity of any of the GFP-G1-based immunoconjugates ($LogIC_{50}$ = 2.5 ± 0.6, 2.2 ± 0.6, 2.4 ± 0.6 nM

EDC-NHS, DBCO-N_3 and DTPA only respectively) and the native GFP-G1 ($LogIC_{50}$ = 5.1 ± 0.9 nM). The blocking capacity of the non-specific mouse IgG (MIgG) ($LogIC_{50}$ = 49.7 ± 1.0 nM) was significantly lower than all GFP-G1-based immunoconjugates.

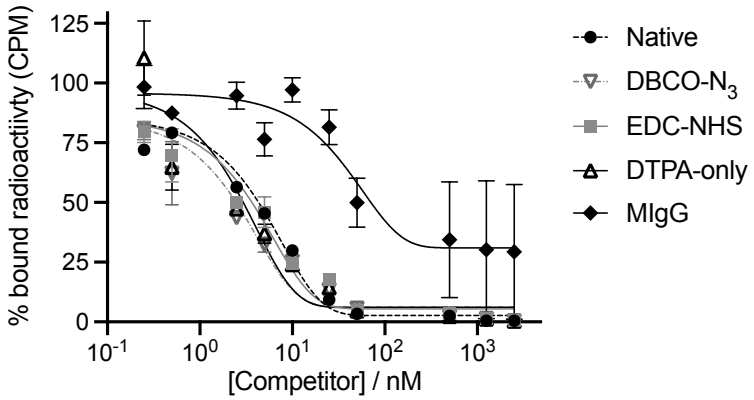


Figure 3.5) Radioimmunoassay blocking comparison of GFP-G1 based RICs. Competition radioimmunoassay comparing blocking capacities of GFP-G1 based immunoconjugates and a radiolabelled GFP-G1 RIC (^{111}In-DTPA-GFP-G1). Symbols and error bars represent mean ± SD, n = 3.

3.3.5 Investigation into toxicity of DTPA-GFP-G1-TAT RICs

Before proceeding to a cell based, *in vitro* radiouptake assay, a clonogenic cell viability assay was carried out to determine whether or not ^{111}In-labelled, DTPA-GFP-G1-TAT RICs, conjugated using either the EDC-NHS or DBCO-N_3 techniques, resulted in increased cytotoxicity. CPPs when delivered at high concentrations can be cytotoxic, though reports show that TAT is generally well tolerated by cells up to 100 μM (Cardozo et al., 2007). However, given that the primary objective of ^{111}In-DTPA-IgG-TAT based RICs is to deliver ^{111}In, an Auger electron emitting radioisotope, to an intranuclear target, it is conceivable that this could also induce DNA damage, affecting cell viability. To show if increased cellular uptake in cells expressing a nuclear target protein reduced cell viability, H1299 wild type (WT) and H1299 cells stably transfected with a nucleus bound EGFP fusion protein (H2B-EGFP 45)

were incubated for one hour with complete cell culture medium supplemented with ^{111}In-DTPA-GFP-G1-TAT (1.5 nM / 1MBq/μg) (**Figure 3.6)**. In both cell lines, no statistically significant difference in colony formation was observed between the untreated group (NT) and cells incubated with all types of GFP-G1 based RICs.

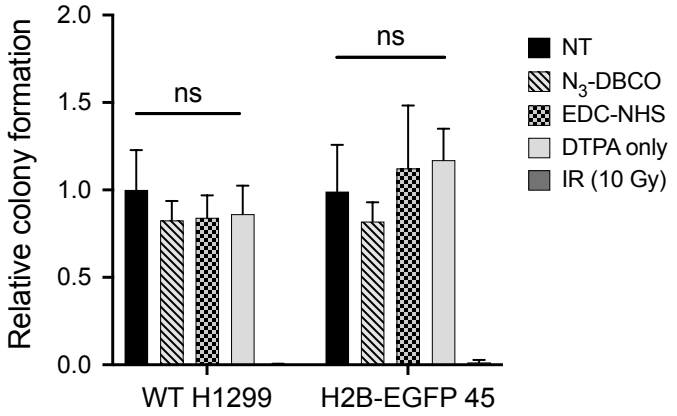


Figure 3.6) Colony formation assay to determine the effect of ^{111}In-GFP-G1-TAT uptake on cell viability. In vitro colony formation assay demonstrated no significant difference in relative colony formation between cells exposed to ^{111}In-DTPA-GFP-TAT produced by the N3-DBCO method, EDC-NHS method, or ^{111}In-DTPA-GFP-G1-TAT. Bars represent mean ± SD, ns = $P > 0.05$.

3.3.6 In vitro uptake comparison of DTPA-GFP-G1-TAT RICs

Once the effect of EDC-NHS and DBCO-N_3 TAT conjugation methods on GFP-G1 based RIC stability, binding affinity, and the potential for cytotoxicity was evaluated, an *in vitro* cell uptake assay was used to compare the ability of each RIC to be taken up by cells expressing a nucleus bound target protein. H1299 WT and H2B-EGFP 45 cells were incubated for 1 h with ^{111}In-DTPA-GFP-G1-TAT (1.5 nM / 1 MBq/μg) prepared using the EDC-NHS and DBCO-N_3 methods and ^{111}In-DTPA-GFP-G1 without TAT (**Figure 3.7**). With all three radioimmunoconjugates, observed uptake was higher in H2B-EGFP 45 cells in comparison to WT H1299 cells. However, only the difference in radiouptake of ^{111}In-DTPA-GFP-G1-TAT,

prepared using the N_3-DBCO method, between WT H1299 (1.44 ± 0.63) and H2B-EGFP 45 (3.11 ± 1.47) was statistically significant ($P = 0.013$).

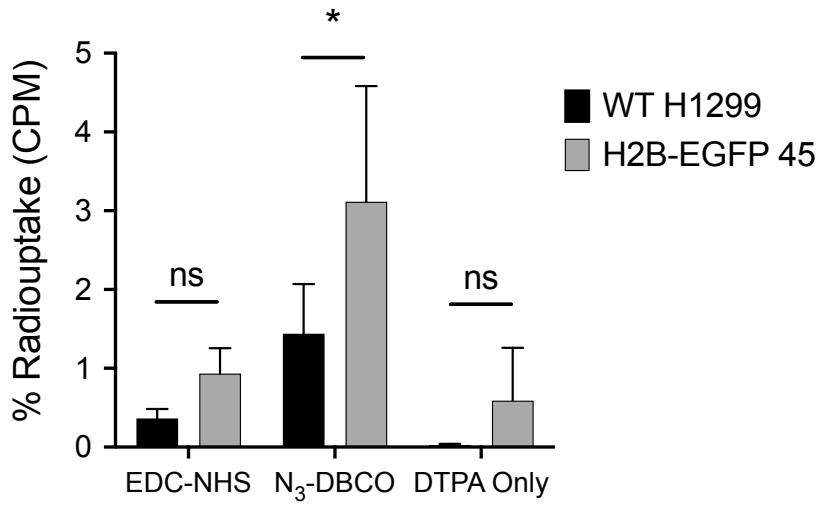


Figure 3.7) Comparison of uptake of ^{111}In-DTPA-GFP-G1-TAT prepared by different TAT conjugation methods. In vitro uptake assays showed increased uptake in GFP-positive cells for all GFP-G1-based RICS, however, only the difference in uptake using ^{111}In-DTPA-GFP-G1-TAT prepared using the N3-DBCO method was statistically significant. Bars represent mean ± SD, * = $P < 0.05$, ns = $P > 0.05$.

3.4 Discussion

Unlocking the full range of applications of antibody- or antibody fragment- based PET/SPECT imaging requires the conjugation of additional functional groups. Therefore, the choice of a reliable conjugation strategy to complement the intended application is also critical. Antibody-based PET/SPECT imaging of intranuclear epitopes requires the conjugation a chelator, such as DTPA, to carry the radioisotope for imaging, along with a CPP, for instance TAT, to promote the movement of the RIC across cellular membranes to facilitate target engagement. This project set out to develop a novel, simplified chelator/CPP conjugation approach using SPAAC click-chemistry to improve specific uptake of IgG-TAT based RICs.

One of the major advantages of using the DBCO-N_3 method is that the DBCO group is detectable by UV-visible spectroscopy (A_{max} = 309 nm), which no longer occurs once the group has been reacted with a N_3-modified functional group. This allows the user to quantitatively determine the molar ratio of IgG to attached DBCO groups and moreover the amount of DBCO groups which have reacted, providing an insight into the relative number of functional groups being conjugated onto the antibody that was not possible with the previous EDC-NHS method. The objective of this initial study was to determine conjugation conditions that were optimal for labelling each IgG molecule with at least one DTPA and at least one TAT functional group, whilst minimising potentially deleterious alterations. The reaction of a non-specific polyclonal antibody (RIgG) with increasing amounts of STP-DBCO showed that this reaction was highly efficient when the molar excess of STP-DBCO was four or less, increasing the amount of STP-DBCO beyond resulted in a progressive reduction in labelling efficiency (**Figure 3.2A**). Furthermore, when these DBCO modified antibodies were reacted with an azide-modified fluorophore (sulfo-Cy5-N_3) the reduction in labelling efficiency was further reduced.

Radiolabelling of DTPA-GFP-G1-TAT, prepared using the N_3-DBCO method, was highly efficient (>95%) and comparable to both GFP-G1 RICs prepared using the amine reactive pSCN-Bn-DTPA (**Figure 3.4A**). When compared for radiolabelling stability, DBCO-N_3 method prepared ^{111}In-DTPA-GFP-G1-TAT showed consistently lower radiolabelling purity over 72 hours when incubated at 37°C in PBS (**Figure 3.4B**). However, there was no detectable signals of released ^{111}In or degraded RIC fragments observed in samples incubated in mouse serum (**Figure 3.4C**). This accelerated degradation in PBS solution may be a result of mechanical stress due to low level non-specific binding of ^{111}In-DTPA-GFP-G1-TAT to the incubation vessel, which would be both increased in RICs conjugated with TAT and negated by incubation in a protein rich medium, such as mouse serum. It should be noted that by using a modular conjugation strategy like the N_3-DBCO method allows for relatively simple

exchange between chelators, future research will look to improve radiolabelling stability through the use of alternative chelators, such as CHX-A''-DTPA (Price and Orvig, 2014).

The radioimmunoassay demonstrated no statistically significant difference in ^{111}In-DTPA-GFP-G1 binding capacity between any of the GFP-G1 based immunoconjugates, including the unmodified GFP-G1 antibody (**Figure 3.5**). Whilst it would be beneficial to determine whether any labile amino acid side chains would be present within the antigen binding site of GFP-G1, this would involve high involved structural analyses, such as x-ray crystallography (Lu et al., 2005).

The colony formation assays showed that uptake of all GFP-G1 based RICs *in vitro* did not result in a reduction in cell viability (**Figure 3.6**). This was expected as previous reports suggest that the concentration of TAT required to impact cell viability is at least 50 μM, which is several orders of magnitude more than the concentration of IgG-TAT based RICs used in this study (El-Andaloussi et al., 2007). Furthermore, although being targeted to the cell nucleus, the radiation absorbed dose was not enough to reduce cell viability, which is consistent with previous research using both ^{111}In and ^{89}Zr labelled γH2AX, specific IgG-TAT based-RICs (Knight et al., 2015),

The comparison in radiouptake of ^{111}In-DTPA-GFP-G1-TAT in the H2B-EGFP 45 cell line showed a clear and statistically significant difference in uptake of the RIC prepared by the DBCO-N_3 conjugation method in comparison to the EDC-NHS method (3.11% ± 1.47 vs 0.93% ± 0.32 respectively, $P < 0.001$) (**Figure 3.7**). The conjugation of TAT by either the DBCO-N_3 or the EDC-NHS method was shown not alter the binding affinity of ^{111}In-DTPA-GFP-G1-TAT, therefore it is possible that this increase in specific uptake may be a result of increased non-specific cellular internalisation, promoting specific target engagement. However, this increase in specific uptake comes with the penalty of increased non-specific

uptake, with a near four-fold increase in uptake of the DBCO-N_3 prepared RIC in H1299 WT (1.44% ± 0.63 vs 0.36 ± 0.12).

Given the low non-specific uptake observed in the ^{111}In-DTPA-GFP-G1 RIC without TAT (0.02% ± 0.02), this suggests that the extent of non-specific uptake is driven by the presence and abundance per antibody of the TAT peptide. As with most antibody conjugate technologies, the functional group to antibody ratio will certainly affect the function of the immunoconjugate. Future research is required to analyse the exact nature of TAT conjugation for both the N_3-DBCO and EDC-NHS conjugation techniques, for instance determining the exact TAT / IgG ratio by mass spectrometry. This information would be critical when designing a potential IgG-TAT RIC in order to optimise the balance between specific and non-specific uptake to the intended application.

In addition to optimisation of ^{111}In-DTPA-GFP-G1-TAT for uptake in vitro, the immediate focus of this project in the future should be evaluate the uptake of ^{111}In-DTPA-GFP-G1-TAT in an *in vivo* xenograft model. A deeper understanding of how the effect of different conjugation approaches effect the pharmacokinetic properties of an RIC would be useful for optimisation of this technology, which will be vital for potential clinical translation.

In summary, this chapter sets out a novel strategy for the non-specific, simultaneous conjugation of antibodies with the CPP TAT and chelator DTPA, which allows for finer control and more immediate reaction evaluation when producing IgG-TAT based RICs.

Chapter 4

Investigating the detection limits of antibody-based immuno-PET/SPECT imaging of intranuclear epitopes

4.1 Introduction

Nuclear imaging by using radiolabelled modified antibodies, or RICs, by PET or SPECT combines the specificity, versatility and dependable pharmacokinetics typical of monoclonal antibodies with the sensitivity of PET and SPECT and has already shown great promise in cancer imaging (Dewulf et al., 2020).

A novel application of antibody based nuclear imaging is the development of RICs conjugated with cell penetrating peptides, such as TAT, as a means of targeting proteins located within the cell nucleus, which is not possible with unmodified antibodies. TAT-peptide-conjugated antibodies (IgG-TAT) has been used to image several intranuclear targets, including p21 (Hu et al., 2007), p27 (Cornelissen et al., 2009), and the phosphorylated histone protein H2AX using both PET and SPECT (Cornelissen et al., 2011, Cornelissen et al., 2014, Knight et al., 2017). This proof-of-concept work has provided a tantalising glimpse into the potential of IgG-TAT-based PET/SPECT imaging of intranuclear targets.

Given the unparalleled adaptability of antibodies, the range of possible imaging applications using intranuclear IgG-TAT imaging probes is substantial. However, as with all imaging modalities, fundamental limitations in sensitivity are to be expected. Therefore, determining

the minimum target epitope copy number required for antibody-based PET/SPECT imaging would be highly beneficial when novel protein markers are considered as potential targets. *In vivo* imaging using antibody fragments has been demonstrated with extracellular epitopes with copy numbers as low as 25,000 and 8,000 copies/cell (Kenanova et al., 2009, Rosestedt et al., 2015). Intracellular epitope detection limits would be expected to be significantly higher, but a quantitative description of this limit has not yet been explored.

To determine the lower threshold of target abundance required for successful intranuclear imaging using RICs, I previously developed a model system expressing different levels of a well-characterised, stably expressed, nuclear localised target protein construct, histone 2B tagged enhanced green fluorescent protein (H2B-EGFP) (**Chapter 2**). Furthermore, the previously evaluated anti-GFP murine monoclonal antibody GFP-G1 (**Chapter 2**) will be used as the basis of the anti-GFP RIC. This strategy removes several experimental factors that could undesirably alter target abundance, such as the potential for the probe to influence target functionality and the innate variability and temporal changeability in dosages and responses where imaging target epitopes are induced by exogenous treatment. Removing these factors allowed for a more rigorous evaluation of the technical capabilities of antibody-based intranuclear imaging.

4.2 Materials and Methods

4.2.1 Cell culture

Human lung adenocarcinoma H1299 cells (ATCC) were cultured in DMEM (Sigma-Aldrich MO, USA), supplemented with 10% FBS (Thermo Fisher Scientific, MA, USA), 2 mM L-glutamine, 100 units/mL penicillin, and 0.1 mg/mL streptomycin and maintained in a 5% CO_2 humidified atmosphere at 37°C. Cells were tested and authenticated by the providers. The

cumulative length of culture was less than 6 months following retrieval from liquid nitrogen storage. Cells were tested for the absence of mycoplasma at regular intervals. H1299 clone cells lines, stably transfected with H2B-GFP plasmid (**Chapter 2**), were cultured with 50 μg/mL G418/geneticin to promote stability of transfection. Cells were harvested and passaged as required using trypsin-EDTA solution.

4.2.2 Bioconjugation of murine monoclonal antibody GFP-G1

The murine monoclonal antibody GFP-G1 was produced and purified as previously described (**Chapter 2**). Bioconjugation of GFP-G1 with cell penetrating peptide TAT and metal ion chelator DTPA was achieved using SPAAC in a non-site-specific manner (**Chapter 3**). GFP-G1 was buffer exchanged in 0.1 M $NaHCO_3$ pH 8.5, concentrated to 25 μM and reacted with a seven-fold molar excess of DBCO-STP (Click Chemistry Tools, TX, USA) dissolved in DMSO at room temperature for 4 h. The antibody-DBCO conjugate was purified and buffer exchanged to PBS by centrifugal filtration using a Zeba Spin desalting column (7 K MWCO, 0.5 mL, Thermo Scientific, MA, USA). The amount of DBCO tags conjugated to the antibody was determined by absorbance spectroscopy at 280 and 309 nm, with a DBCO:antibody ratio of 5:1. The antibody-DBCO conjugate, at approximately 10 μM, was then reacted with a 2-fold molar equivalence relative to DBCO of 3.4 mM N_3-Bn-DTPA dissolved in PBS + 20% DMSO (synthesised by Deborah Sneddon, Department of Chemistry, University of Oxford, UK), and concurrently, a 1-fold molar equivalence (relative to DBCO) of 1 mM azide-tagged cell penetrating peptide TAT-AHA dissolved in PBS (Cambridge Peptides, Birmingham, UK) at 4°C for 12 h. The antibody conjugate was purified, and buffer exchanged to 0.5 M sodium citrate pH 5.4 to remove unreacted products as previously described. The completion of the conjugation reaction was confirmed by the reduction of UV absorption spectrometry at 309 nm to background level.

4.2.3 Radiolabelling of DTPA-Bn-GFP-G1-TAT with $^{111}InCl_3$

Radiolabelling of DTPA-GFP-G1-TAT was carried out by addition of $^{111}InCl_3$ (Perkin Elmer, MA, USA). Aliquots of 150 µg of GFP-G1 conjugate (1 mg/mL in 0.5 M sodium citrate pH 5.4) were reacted with $^{111}InCl_3$ (1 MBq/µg of antibody) in 0.5 M sodium citrate buffer pH 5.4 for 1 h at room temperature. Radiolabelling yield was determined by instant thin layer chromatography (iTLC) to be greater than 95%. The resulting radiolabelled compound ^{111}In-GFP-G1-TAT was buffer exchanged to PBS to remove free $^{111}In^{3+}$ prior to subsequent studies.

4.2.4 In vitro uptake of ^{111}In-DTPA-GFP-G1-TAT

Aliquots of 8 x 10^4 cells/well were plated in a 24 well plate cell culture dishes and allowed to adhere for 16 h. Culture medium was removed, and cells washed with PBS before addition of fresh culture medium containing ^{111}In-DTPA-GFP-G1-TAT (1.5 nM, 1 MBq/µg) and incubation at 37°C for a further 60 min. Supernatant containing unbound radiolabelled compound was collected, cells were washed twice with PBS before cells were washed for 5 min on ice in 0.1 M glycine pH 2.5 solution to remove membrane-bound radiolabelled antibody conjugate. Finally, cells were lysed by addition of 0.1 M NaOH, and cell-associated compound was collected. The relative amount of ^{111}In within each fraction was determined by automated gamma counting (Wizard^2 2480, Perkin Elmer), to calculate the percentage of cell-associated ^{111}In.

4.2.5 In vivo xenograft uptake of ^{111}In-DTPA-GFP-G1-TAT

All animal procedures were carried out in accordance with the UK Animals (Scientific Procedures) Act 1986 and with local ethical committee approval. Animals were housed in IVC cages in sex matched groups of up to 6 per cage in an artificial day-night cycle facility with *ad*

libitum access to food and water. No animals were culled for welfare reasons. Xenografts of H1299 cells, wild type or stably transfected with varying levels of H2B-EGFP, were established on the right flank of female BALB/c *nu/nu* mice (Envigo, IN, USA) by subcutaneous injection of 2 x 10^6 cells, suspended in 150 µl of equal volume ratio of PBS and phenol red free high concentration matrigel (Corning, NY, USA). Tumours were allowed to grow for 4 weeks to achieve a volume of approximately 180 mm^3 prior to imaging studies. ^{111}In-DTPA-GFP-G1-TAT (5 MBq / 5 µg) in PBS was administered to each mouse via the lateral tail vein. SPECT/CT images were acquired using a SPECT/CT scanner (VECTor^{4}CT, MILabs, Utrecht, the Netherlands) at 24 and 72 h after injection. For each imaging session, anaesthesia was induced and maintained by inhalation of 4% and 2% isoflurane respectively in room air supplemented with oxygen (80%/20% v/v; flow rate 1 L/min). Anaesthesia depth was based on respiration rate monitored using a pneumatic cushion, and isoflurane levels were adjusted to maintain a respiration rate of 40–60 breaths per minute. Induction and recovery were performed in a heated unit with a base temperature of around 37°C to maintain a core temperature of 36°C (Kersemans et al., 2019). After imaging, mice were culled, and samples of blood and other selected organs were collected to determine the percentage of the injected dose per gram of tissue (%ID/g) using a Hidex Automatic Gamma Counter (Hidex Oy, Turku, Finland). Tumour samples were immediately counted prior to flash freezing with dry ice before storage at -80°C for future analysis.

4.2.6 SPECT/CT acquisition and image analysis

All SPECT/CT imaging was carried out using the VECTor^4 imaging system (MILabs, Utrecht, Netherlands) with a rat collimator (HE-UHR-RM, 1.8 mm pinhole). Animals were initially CT imaged (55 kV, 19 mA), immediately followed by list mode SPECT (0–1200 keV) using MILabs acquisition software v11.0. Triple energy window–based scatter correction was

applied for each photon peak window (^{111}In: 155.7–190.3 keV and 218.7–267.3 keV with background windows set to 148.8-155.7 keV, 190.3–197.2 keV, 209.0–218.7 keV, and 267.3–277.0 keV) with a background weight and calibration factor of 2.5 and 1 respectively. All images were reconstructed with MILabs reconstruction software v11.0 on 0.6-mm isotropic 3D voxel grids using similarity regulated ordered-subset expectation maximization (SROSEM). After reconstruction, SPECT and corresponding CT data were coregistered and resampled to equivalent 200-µm voxel sizes. CT-based attenuation correction was applied. Reconstructed images were viewed and analysed using PMOD v.3.37 (PMOD Technologies, Zurich, Switzerland). For accurate scaling and quantification of SPECT image data, phantoms were used to determine a calibration factor applied to all images. Image processing and volume of interest (VOI) analysis was carried out using the PMOD software package (version 3.708, PMOD Technologies, Zürich, Switzerland).

4.2.7 Statistical analysis

All statistical analysis was carried out using GraphPad Prism v8 (GraphPad Software, San Diego, CA, USA). Linear regression with an extra sum of squares F test was used to determine the statistical significance of correlations between estimated regression parameters. One-way ANOVA with Tukey's post hoc test, or 2-way ANOVA was used to compare grouped data to compare individual group means, as appropriate. All data was collected at least in triplicate and presented as mean ± one standard deviation unless otherwise stated.

4.3 Results

4.3.1 In vitro cellular uptake of ^{111}In-DTPA-GFP-G1-TAT

The anti-GFP murine monoclonal antibody GFP-G1 (**Chapter 2**) was conjugated to the radiometal chelator DTPA and CPP TAT in a non-site-specific manor, using DBCO-N_3 mediated SPAAC prior to radiolabelling with $^{111}InCl_3$ (**Figure 4.1A, Chapter 3**). ^{111}In-DTPA-GFP-G1-TAT was evaluated for cellular uptake with several H1299 lung adenocarcinoma clone cell lines, including wild type (WT) H1299 cells and four clones with increasing

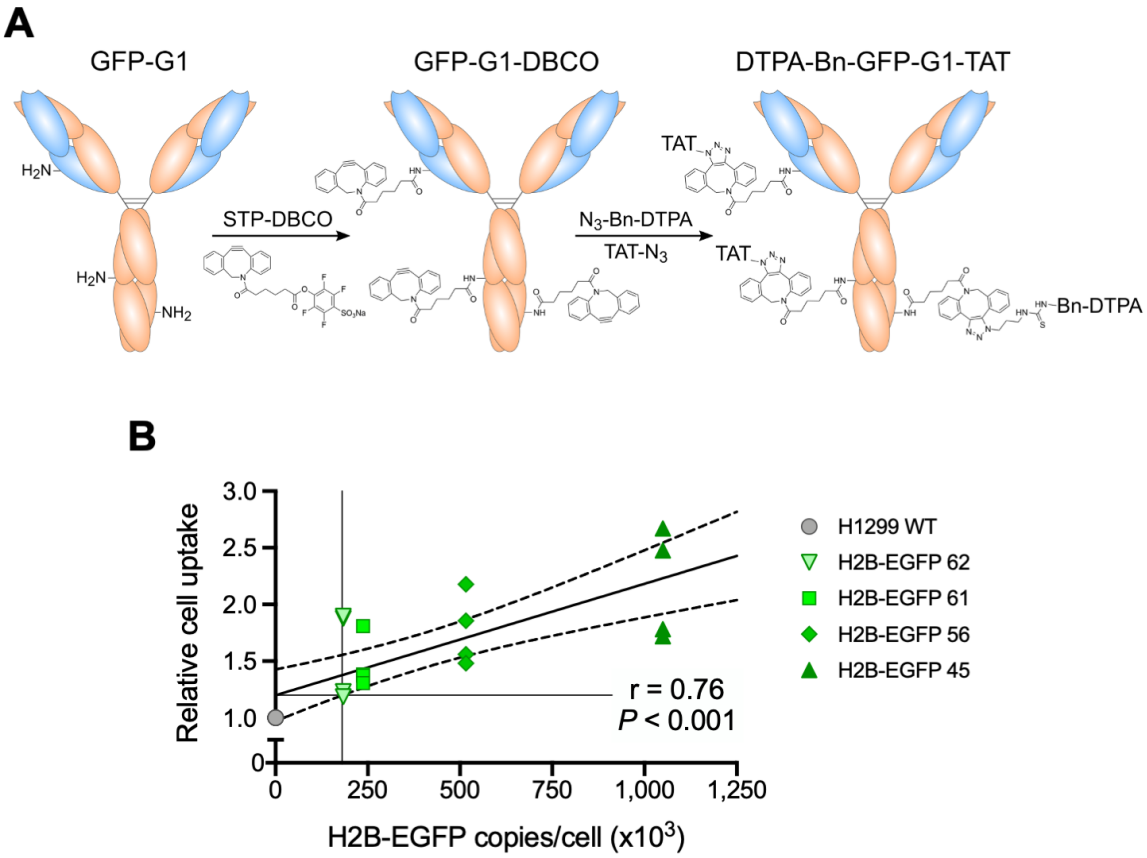


Figure 4.1) Conjugation and in vitro evaluation of ^{111}In-GFP-G1-TAT uptake. A) Schematic diagram outlaying the approach to conjugate monoclonal antibody GFP-G1 with the CPP TAT and chelating agent DTPA using SPAAC based click chemistry. B) *In vitro* radio-internalisation assay revealing the correlation between ^{111}In-GFP-G1-TAT uptake and H2B-EGFP expression.

expression of the nucleus bound GFP fusion protein H2B-EGFP (H2B-EGFP 62, 61, 56 & 45 respectively, **Chapter 2**). *In vitro* radiouptake assays revealed a correlation between cellular uptake of ^{111}In-DTPA-GFP-G1-TAT and increasing expression of H2B-EGFP, suggesting that uptake was the result of specific binding between ^{111}In-DTPA-GFP-G1-TAT and intranuclear H2B-EGFP (**Figure 4.1B**, r = 0.76, $P < 0.001$). A linear regression model relating cell uptake of ^{111}In-DTPA-GFP-G1-TAT and H2B-EGFP expression was used to predict a minimum detectable expression level of H2B-EGFP, which was approximately 182,000 copies/per cell.

4.3.2 Biodistribution of ^{111}In-DTPA-GFP-G1 in an in vivo xenograft model

Xenograft tumour mouse models were established, bearing tumours consisting of H1299 WT, H2B-EGFP 62, 56 and 45 cells. Xenograft bearing mice were administered 5 MBq / 5 μg) ^{111}In-DTPA-GFP-G1-TAT and SPECT/CT acquisition was conducted at 24 and 72 h post injection, after which the animal was sacrificed for ex vivo biodistribution studies. Ex vivo biodistribution of ^{111}In-DTPA-GFP-G1-TAT tumour uptake revealed a statistically significant correlation between tumour uptake and H2B-EGFP expression (**Figure 4.2A & B**, r = 0.63, P = 0.004), suggesting ^{111}In-DTPA-GFP-G1-TAT was capable of quantitatively determining the expression level of H2B-EGFP. Interpolation of the linear regression model of ^{111}In-DTPA-GFP-G1-TAT uptake with H2B-EGFP expression predicted that the lower abundance detection threshold of H2B-EGFP was approximately 240,000 copies per cell, which was expectedly somewhat higher than the predicted value *in vitro*. This finding was supported by the statistically significant differences in uptake of ^{111}In-DTPA-GFP-G1-TAT between H1299 WT (16.1 ± 3.4 %ID/g), H2B-EGFP 56 (21.9 ± 2.7 %ID/g; $P = 0.033$) and H2B-EGFP 45 (24.8 ± 1.6 %ID/g; $P = 0.010$). Despite the low abundance threshold predicted by the model, there was also a significantly significant difference in tumour uptake between H1299 WT and H2B-

EGFP 62 (22.4 ± 5.0 %ID/g; $P = 0.018$), which has been shown to have an expression level of 183,000 copies/cell (**Chapter 2**).

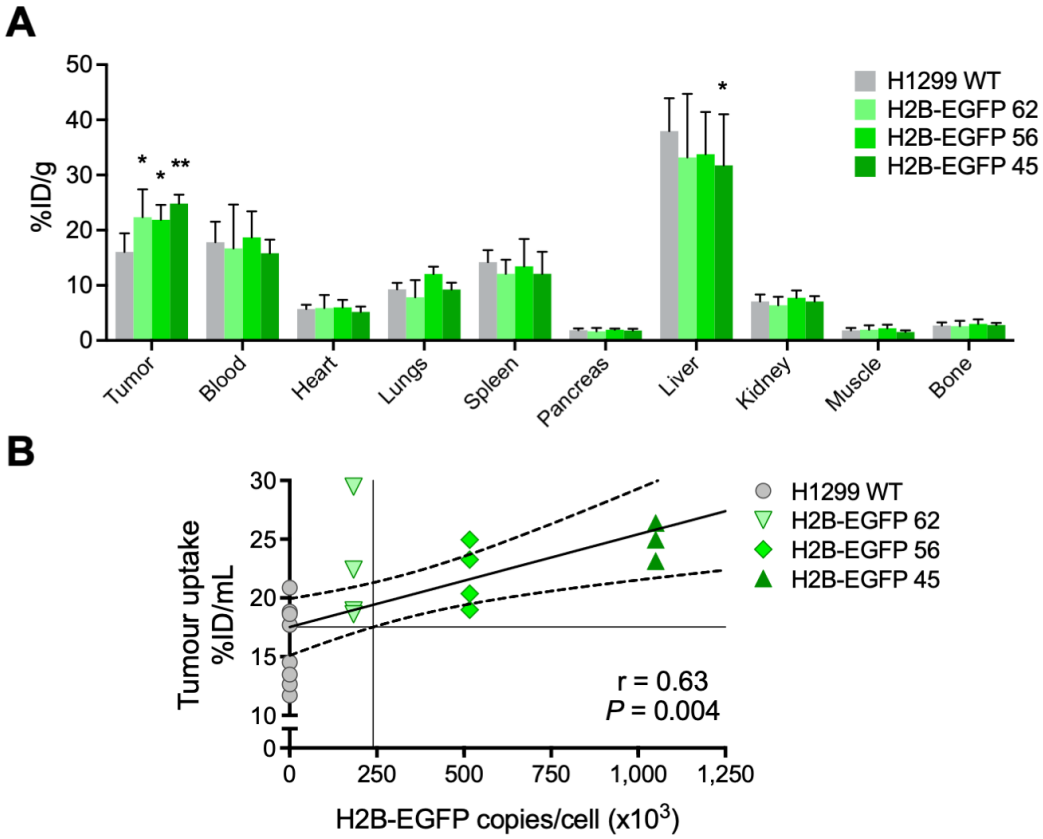


Figure 4.2) Ex vivo biodistribution and tumour uptake of ^{111}In-DTPA-GFP-G1-TAT. A) *Ex vivo* biodistribution showing the uptake of ^{111}In-DTPA-GFP-G1-TAT in selected tissues and blood, 72 h after intravenous administration. B) Tumour uptake of ^{111}In-DTPA-GFP-G1-TAT *in vivo* correlated linearly with expression of H2B-EGFP. Asterisks denote statistically significant differences in uptake from the H1299 WT group (* $P < 0.05$; ** $P < 0.01$).

4.3.3 Evaluation of ^{111}In-DTPA-GFP-G1-TAT tumour uptake by SPECT/CT image analysis.

In addition to *ex vivo* biodistribution analysis, the uptake of ^{111}In-DTPA-GFP-G1-TAT was also determined by SPECT/CT imaging (**Figure 4.3**). Image quantification analysis of ^{111}In-DTPA-GFP-G1-TAT distribution at 24 and 72 hours post injection revealed a statistically

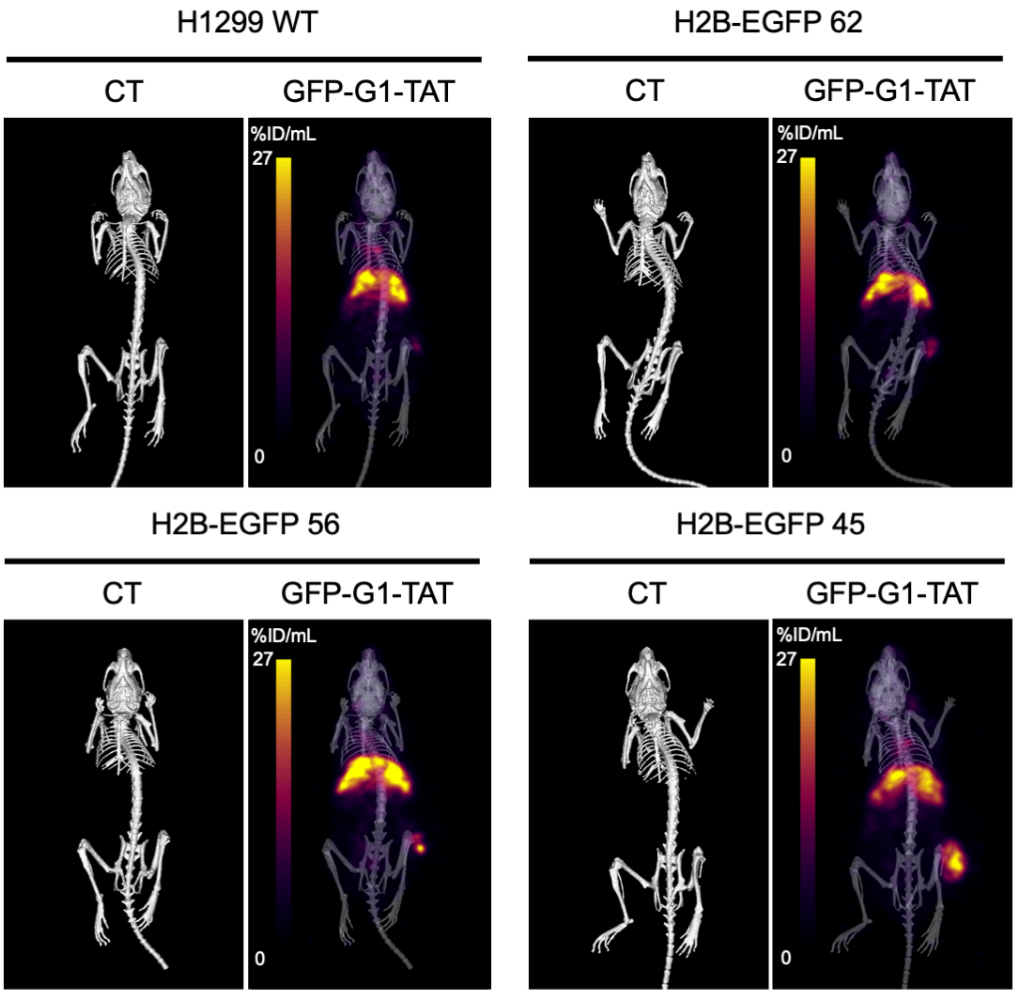


Figure 4.3) Imaging of ^{111}In-DTPA-GFP-G1-TAT *in vivo*. Representative CT and SPECT images showing distribution of ^{111}In-DTPA-GFP-G1-TAT in mice bearing H2B-EGFP transfected H1299 cells, 72 h after intravenous administration.

significant correlation between tumour uptake and expression of H2B-EGFP (r = 0.66, *P* = 0.010 & r = 0.68, *P* = 0.001 respectively; **Fig 4.4A & B**). Interpolation of the linear regression model of ^{111}In-DTPA-GFP-G1-TAT uptake at the 24-hour timepoint suggested a lower abundance detection threshold of 316,000 copes/cell. However, the predicted threshold after 72 hours was 237,000 copies/cell, which is akin to the result obtained from the biodistribution study taken at the same time point.

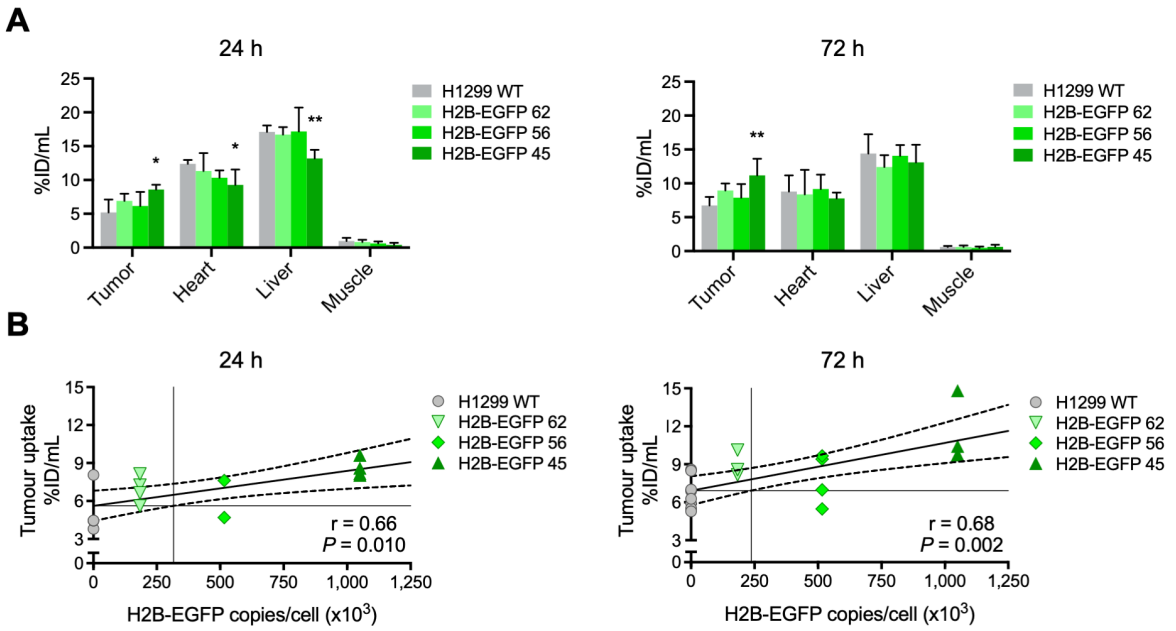


Figure 4.4) Image quantification analysis of ^{111}In-DTPA-GFP-G1-TAT biodistribution *in vivo*. A) Image quantification analysis showing uptake of ^{111}In-DTPA-GFP-G1-TAT in selected tissues, 24 h and 72 h after intravenous administration. **B)** Correlation of quantified tumour uptake with expression of H2B-EGFP, 24 h and 72 h after intravenous administration. Asterisks denote statistically significant differences in uptake from the H1299 WT group (* P < 0.05; ** P < 0.01, *** P < 0.001).

4.4 Discussion

Antibody- or antibody fragment-based PET/SPECT imaging is an expanding field of research, with an increasingly diverse selection of radioisotopes and antibody-based vector systems, which can be effectively tailored towards a specific application (Dewulf et al., 2020). The efficacy of any antibody-based PET/SPECT imaging device is primarily controlled by a combination of three factors (Reddy and Robinson, 2010). Firstly, is target abundance, which must be sufficient enough for detection in the target tissue. Next is the targeting component of the RIC, which ideally would bind the target with high affinity and fidelity. Finally, the pharmacokinetic and clearance characteristics of the RIC is critical for effective target engagement *in vivo*. Using the H2B-EGFP model system in conjugation with the previously

evaluated murine monoclonal antibody GFP-G1 allowed for interrogation of the effect of changing target abundance within the context of other characterised factors, which would otherwise confound the findings.

Evaluation of uptake of ^{111}In-DTPA-GFP-G1-TAT *in vitro* demonstrated a correlation between cellular uptake and increased expression of H2B-EGFP with a projected lower abundance detection threshold of 182,000 copies/cell (**Figure 4.1B**). This value is significantly higher than that the lower abundance threshold when targeting extracellular epitopes with antibody fragment based RICs, with reports suggesting that this value could be a low as 8,000 copies per cell (Rosestedt et al., 2015). In order to realise the full potential of this technology there are several areas of improvement that must be addressed. In particular, the relatively modest increase in ^{111}In-DTPA-GFP-G1-TAT uptake between H1299 WT and H2B-EGFP expressing cells is indicative of high levels of non-specific uptake. Whilst the conjugation of a cationic CPP such as TAT is essential to facilitate movement of the RIC across cellular membranes, this modification can increase the degree of non-specific binding as a consequence of the highly charged nature of cationic CPPs (Aguilera et al., 2009). This model system would provide a useful tool to evaluate the effects of CPP charge or CPP-IgG stoichiometry on both specific and non-specific cellular uptake.

CPP and indeed cargo protein selection can also affect the mechanism of cell internalisation, subsequently impacting the efficiency and specificity of cellular uptake. The internalisation of CPP-cargo conjugates is believed to be largely driven by endocytosis under physiological conditions (Duchardt et al., 2007), although the exact nature of which endocytic pathway is utilised is unclear, with suggestions of some level of redundancy between endocytosis pathways (Ruseska and Zimmer, 2020). One major challenge facing CPP-mediated delivery of cargo proteins is endosomal entrapment, where CPP-cargo conjugates are degraded within cellular lysosomes rather than being released into the cytosol, resulting in high cell uptake but

poor cytosolic availability and reduced target engagement (Pei and Buyanova, 2019). Recent advances using novel, cyclic derivatives of cationic CPPs have demonstrated not only remarkable increases in overall cell uptake but also cytosolic availability, in comparison with linear equivalents (Patel et al., 2019, Nischan et al., 2015). Another consideration on the efficiency of CPP-cargo uptake is molecular mass of the cargo protein. Larger proteins, such as antibodies (approximately 150 kDa), are internalised at considerably lower efficiencies than smaller proteins (Tunnemann et al., 2006). Future research should use this model system as a means to investigate whether alternative CPPs or even alternative antibody-fragment constructs could maximise specific uptake of IgG-TAT based RICs.

In vivo evaluation of ^{111}In-DTPA-GFP-G1-TAT by biodistribution and quantitative image analysis showed a similar correlation to the *in vitro* studies between tumour uptake of ^{111}In-DTPA-GFP-G1-TAT and H2B-EGFP expression (**Figures 4.2, 4.3, 4.4**). Furthermore, both ex-vivo biodistribution and quantitative image analysis 72 hours post injection suggest a low target abundance detection limit of approximately 240,000 copies/cell. This threshold was higher than that observed from the *in vitro* studies, which may be as a result of increased non-specific signal arising from the enhance permeability and retention (EPR) effect in conjunction with high blood background signal characteristic of antibodies (Maeda et al., 2013). A major feature of antibodies which contributes towards high blood retention is the presence of a functional fragment crystallisable (Fc) domain, which prevents antibody degradation though neonatal Fc receptor (FcRn) mediated recycling (Pyzik et al., 2015). Previous reports show that using smaller antibody fragments, without an Fc domain, can utilise the renal clearance pathway and negate FcRn mediated recycling, significantly reducing blood retention and potentially non-specific signal (Freise and Wu, 2015). The model system presented in this study would provide a great opportunity to thoroughly investigate whether or not using smaller

GFP-G1-based antibody fragments could improve sensitivity and reduce non-specific signal, both *in vitro* and *in vivo*.

The principal objective of this chapter was to provide an insight into the properties required for a successful candidate for intranuclear antibody-based PET/SPECT imaging. Previously, the most successful example of intranuclear imaging with antibody based RICs is with imaging the DNA damage marker γH2AX, which has an approximate cellular abundance of 800,000 copies/cell post irradiation, though this is dependent on environmental factors, such as the cell line or extent of DNA damage incurred prior to imaging (Cornelissen et al., 2011). Other examples of proteins imaged using similar approaches are p21 and p27, which both have estimated expression levels between 10^4-10^5 copies/cell at baseline in normal tissue (Bekker-Jensen et al., 2017, Hu et al., 2007, Cornelissen et al., 2009). As these expression levels fall below the minimum abundance detection threshold predicted by this study, I acknowledge that the value obtained from this study is specific to this model system and cannot be treated as absolute. What this model system does provide, however, is an approximate baseline of this novel technology, and a platform to interrogate which factors ultimately govern the efficacy of antibody- or antibody fragment- based PET/SPECT imaging of intranuclear targets.

To conclude, this research provides a proof-of-concept methodology to evaluate, quantitatively, the practical limitations of antibody-based intranuclear PET/SPECT imaging using an IgG-TAT RIC. This research simultaneously provides a basis to further investigate and optimise which parameters are required for effective antibody-based PET/SPECT imaging devices, potentially delivering a variety of more potent whole-body immuno-imaging devices.

Chapter 5

Imaging phospho-ATM using antibody-based PET/SPECT imaging

5.1 Introduction

The imaging of cancer has become a cornerstone of clinical oncology, providing a wide range of applications, such as early diagnostic tools, patient stratification and post-therapy evaluation (Fass, 2008). Given the rapid expansion of highly specific, personalised cancer therapeutics, the demand for the development of equally sophisticated complementary imaging modalities has never been more critical. Molecular imaging using novel single-photon emission computerised tomography (SPECT) or positron emission tomography (PET) radiotracers has already shown great promise to image, in some cases quantitatively, a range of cellular characteristics, from hypoxia to immune system response (James and Gambhir, 2012). The principle aim of this chapter was to develop a PET/SPECT imaging agent which is able to locate regions of high occurrence of DNA damage by imaging the phosphorylation of the serine/threonine protein kinase ataxia telangiectasia mutated (ATM) as an early indicator of the cellular DNA damage response (DDR).

Throughout life, DNA is exposed to a broad range of potential hazards, both endogenous and exogenous, resulting in tens of thousands of DNA lesions per cell per day (Lindahl and Barnes, 2000). If unrepaired, these lesions will develop into potentially deleterious mutations, which upon accumulation, ultimately manifest in cellular pathologies, including cancer. In response

to DNA lesions, the cell utilises a highly conserved repertoire of signalling pathways and mechanisms, collectively known as the DNA damage response (DDR), as a means of preventing DNA lesions developing into mutations (Jackson and Bartek, 2009). Amongst the most dangerous of DNA lesions are double strand breaks (DSBs), which can be instigated by factors, such as ionising radiation or stalled replication forks (Khanna and Jackson, 2001).

ATM is a serine/threonine protein kinase that is part of the phosphatidylinositol 3-kinase-related kinase (PIKK) family, which acts in concert with the related PIKK family members DNA dependant protein kinase (DNA-PK) and ataxia telangiectasia and Rad3-related protein (ATR) to coordinate the DDR (Blackford and Jackson, 2017). ATM in particular performs an apical role within the DDR as the principal orchestrator of the cellular response to DSBs, phosphorylating hundreds of substrates to regulate a myriad of cellular processes, including DNA repair, apoptosis, alteration of chromatin, cell cycle checkpoint activation and more (Shiloh and Ziv, 2013).

In quiescent cells, ATM exists primarily as an inactive dimer, located primarily within the nucleoplasm (Bakkenist and Kastan, 2003). Upon recognition of a DSB, ATM is recruited to the site of a DSB prior to confirmational change, causing dissociation of the dimeric structure to yield kinase active ATM monomers (**Figure 5.1**) (Paull, 2015). Despite considerable efforts, the exact mechanism that initiates this conformational change remains elusive. The earliest model suggested that ATM dimer dissociation and activation was driven by trans-autophosphorylation of ATM at several sites, notably Ser1981. However, subsequent studies have shown that mutation of these phosphorylation sites failed to ablate ATM kinase activation, both *in vitro* and *in vivo* (Lee and Paull, 2005, Daniel et al., 2008). Other reports suggest that ATM dissociation is triggered though interaction with other ligands, in particular the MRN (MRE11, RAD50, NBS1) complex, though studies have demonstrated presence of MRN to not be essential for ATM activation. Despite this uncertainty, phosphorylation of ATM at residue

Ser1981 is considered to be the canonical indicator of ATM activation (Kozlov et al., 2011). This project aims to develop an antibody-based PET/SPECT imaging probe that targets phospho-Ser1981-ATM (pATM) as a means of imaging the cellular response to DNA DSBs.

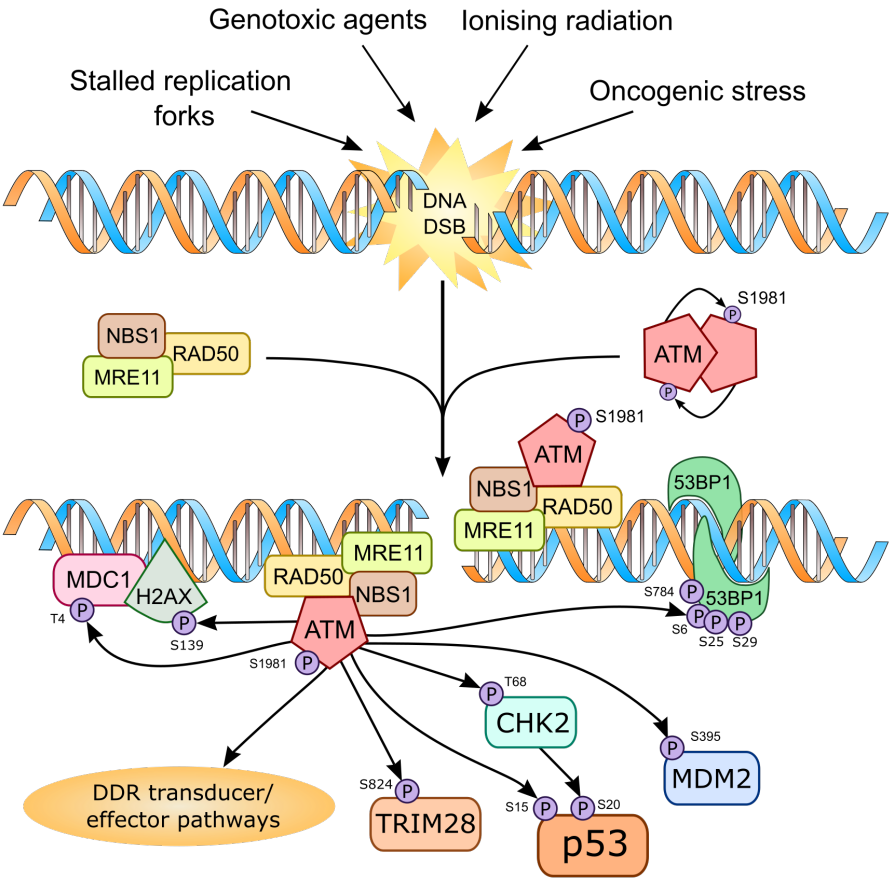


Figure 5.1) Activation and functions of protein kinase ATM within the DNA damage response. An illustration depicting the central role of protein kinase ATM in the cellular response to DNA double strand breaks (DSBs).

Imaging of the DDR by targeting pATM has potential for several diagnostic and analytical tools. Genomic instability has been long established as an *enabling characteristic* of cancer, with DNA damage and mutation occurring at early stages of tumourigenesis (Hanahan and Weinberg, 2011). Furthermore, the formation of precancerous lesions has been shown to correlate with the phosphorylation of several proteins within the DDR, including ATM and ATM target proteins, including p53 and H2AX, suggesting that imaging pATM could have a

potential application as an early diagnostic tool (Bartkova et al., 2005, Gorgoulis et al., 2005). In addition to early diagnostics, imaging changes to pATM levels in response to clinical intervention, such as radiotherapy or cytotoxic chemotherapy, would also have possible applications for monitoring therapeutic delivery and even post therapy patient evaluation (James and Gambhir, 2012).

When evaluating which approach would be best suited for imaging pATM, an antibody-based PET/SPECT imaging probe, or RIC, initially presented several advantages over alternative strategies, such as ^{11}C or ^{18}F-labelled small molecule inhibitors. Firstly, monoclonal antibodies are capable of relatively favourable sensitivities and specificities in comparison to small molecule inhibitors (Castelli et al., 2019). Furthermore antibody-based RICs can easily be conjugated with alternative functional groups without compromising the targeting or pharmacokinetic properties of the probe, increasing both functionality and versatility (Wu, 2014).

One major disadvantage of imaging an intranuclear epitope with an antibody-based imaging probe is their relatively large size (~150,000 Da) and hydrophilicity render them unable to efficiently cross cellular membranes, without medication. These barriers, however, can be overcome by the conjugation of the antibody to a cell penetrating peptide (CPP), such as the HIV-1 derived TAT peptide, which facilitates the movement of cargo proteins across the cellular membrane (Guidotti et al., 2017). As pATM localisation is predominantly within the nucleus, I will be conjugating an anti-pS1981 ATM monoclonal antibody to the cell penetrating peptide TAT, which also features an NLS which will aid the movement of the RIC to the nucleus for optimal target engagement (Efthymiadis et al., 1998).

In this chapter, I will demonstrate the initial process of developing a novel IgG-TAT-based RIC with the purpose of non-invasively imaging pATM as a marker of the DDR *in vivo* using PET or SPECT imaging. Which will involve firstly the validation of a suitable cell model

system, followed by the selection of a suitable anti-pATM antibody. The candidate antibody will then be adapted for use as an pATM targeted RIC and evaluated for cell uptake in an *in vitro* model system.

5.2 Materials and methods

5.2.1 Cell culture

Lung adenocarcinoma cell lines H1299 and COR-L105 cells, stably transfected with siRNA targeting ATM and GFP (non-targeted control) were provided by Anderson Ryan (University of Oxford, Oxford, UK). Cells were cultured in DMEM (Sigma-Aldrich, MO, USA), supplemented with 10% FBS (Life Technologies), 2 mM L-glutamine, 100 units/mL penicillin, and 0.1 mg/mL streptomycin and maintained in a 5% CO_2 humidified atmosphere at 37°C. Cells were authenticated by the providers. The cumulative length of culture was less than 6 months following retrieval from liquid nitrogen storage. Cells were tested for the absence of mycoplasma at regular intervals. Cells stably transfected siRNA were cultured with 0.5 µg/ml puromycin to promote transfection stability.

5.2.2 Cell irradiation

Cells were treated with ionisation radiation using an IBL-637 ^{137}Cs irradiator (CIS Biointernational, Saclay, France). Radiation absorbed dose was calculated based on time using a dose rate of 0.81 Gy/min.

5.2.3 Cell lysate preparation

Aliquots 1.2 x 10^5 cells were plated in 6 well plates with complete culture medium and incubated overnight at 37°C with 5% CO_2. Cells were placed on ice and washed twice in ice

cold PBS before lysis by addition of 100 µl RIPA buffer plus cOmplete™ EDTA-free Protease Inhibitor Cocktail (Sigma, Dorset, UK). Lysates were collected and set on ice for 20 min with vortexing every 5 min. Lysates were clarified by centrifugation (30 min, 16,000 x g, 4℃) and protein concentration of supernatants was determined by BCA assay (Sigma, Dorset, UK) prior to storage a -20℃ until required.

5.2.4 SDS-PAGE & western blot

Lysates were reduced and linearised by the addition of Laemmli sample loading buffer (4% SDS, 20% glycerol, 120 mM Tris-HCl pH 8.6, 0.02 % w/v bromophenol blue) and heated to 96℃ for 5 minutes prior to loading for separation on pre-cast SDS-PAGE gels (Thermo Scientific, MA, USA). Separated proteins were transferred onto a polyvinylidene fluoride (PVDF) membrane using an XCell II™ Blot Module according to manufacturer protocol (Invitrogen, CA, USA). Transferred membranes were rinsed in TBS pH 7.4 and blocked with blocking buffer (5% milk powder dissolved in TBST) for 1 h at room temperature. Membranes were incubated with primary antibody in blocking buffer overnight at 4℃. Membranes were then washed 3 x 15 min in TBST, incubated with HRP conjugated secondary antibody for 1 h at room temperature and washed 3 x 15 min again in TBST. Membranes were developed by addition of Pierce™ ECL Western Blotting Substrate (Thermo Scientific, MA, USA) and chemiluminescence was detected using C-DiGit® Blot Scanner (LI-COR, NE, USA). All primary and secondary antibodies used in this study can be found in the antibody reference table A1 in the appendices.

5.2.5 Flow cytometry

Aliquots of 2 x 10^6 cells were plated in a T175 cell culture flask with complete culture medium and incubated overnight at 37℃ with 5% CO_2. Cells were washed twice in ice cold PBS and

collected by scraping followed by another wash by centrifugation (400 x g, 5 min). Cells were fixed by incubation in PBS containing 4% PFA at 37℃ for 10 min followed by washing by centrifugation in PBS. Fixed cells were permeabilised by addition of 0.25% Triton X-100 in PBS at 4℃ for 20 min and washed again in PBS prior to blocking in flow cytometry blocking buffer (PBS containing 2% FBS) for one hour at room temperature. Samples were washed in PBS and incubated for 2 h at room temperature with primary antibody in flow cytometry blocking buffer at the desired concertation. Stained cells were washed with PBS before incubation for 1 h at room temperature with an appropriate fluorophore conjugated secondary antibody. Data was acquired using Invitrogen Attune NxT flow cytometer (Invitrogen, CA, USA). Data analysis was carried out using FlowJo™ v10.6.2 (FlowJo LLC, OR, USA). 20,000 events were counted per sample and plotted side scatter height (SSC-H) vs forward scatter height (FSC-H) to gate the cell population and exclude cell debris. From this population, doublet cells were excluded by correlation of forward scatter width (FSC-W) and side scatter area (FSC-A). The intensity of the appropriate fluorophore (AF488 or AF594) was plotted on a logarithmic scale against normalised cell count. Geometric mean fluorescence intensities were calculated for each sample for further quantification analysis.

5.2.6 Immunofluorescence microscopy

2 x 10^4 cells were plated in 8 well chambered tissue culture slides (Fisher Scientific, NH, USA) with complete culture medium and incubated overnight at 37℃ and 5% CO_2. Cells were rinsed three times in ice cold PBS twice before fixation by addition of PBS containing 4% paraformaldehyde (PFA) at 37℃ for 10 min followed by washing with PBS. Cells were then permeabilised by addition of 0.2% Triton X-100 at 4℃ for 20 min and washed again with PBS. Blocking solution of PBS + 2% FBS was added for 1 h at room temperature before washing in PBS and addition of blocking solution with the primary antibody at the desired concentration,

which was incubated at 4℃ overnight. The primary antibody solution was removed and cells washed three times in PBS for 15 min before addition of blocking solution containing the appropriate secondary antibody for 1 hour at room temperature. Stained cells were then washed three times in PBS for 15 min before mounting Vectashield® mounting media containing DAPI (Vector Laboratories, CA, USA). Confocal microscopy of stained cells was carried out on the Leica TCS SP8 platform (Leica Microsystems, Wetzlar, Germany), equipped with 63 × oil-immersion objective lenses. Within each experiment, image acquisition and processing parameters were kept consistent for each sample.

5.2.7 Bioconjugation of DTPA-D25E5-TAT by EDC/NHS crosslinking

Monoclonal antibody D25E5 (250 μg) was buffer exchanged to 0.1 M MES pH 6 and concentrated to 25 μM. The solvent accessible carboxyl groups of D25E5 were then activated for reaction with primary amines by addition of a 40-fold molar excess of EDC for 15 min at room temperature. A 100-fold excess of sulfo-NHS was simultaneously added for increased stability of the O-acylisourea intermediate. Excess EDC/NHS was removed and MES buffer was exchanged with PBS by centrifugal filtration using a Zeba Spin desalting column (7 K MWCO, 0.5 mL, Thermo Scientific, MA, USA). Antibody concentration was determined by NanoDrop (Thermo Scientific, MA, USA) before incubation with a 10-fold molar excess of the peptide TAT for 2 h. Excess TAT was removed and PBS buffer was exchanged with 0.1 M sodium bicarbonate (pH 8.5) by centrifugal filtration. TAT conjugated antibodies were then reacted with a 20 fold molar excess of S-2-(4-Isothiocyanatobenzyl)-diethylenetriamine pentaacetic acid (pSCN-Bn-DTPA) (Macrocyclics, TX, USA) for 1 h at 37°C before centrifugal filtration to remove unconjugated SCN-Bn-DTPA and exchange buffer to 0.5 M sodium citrate pH 5.5 for subsequent radiolabelling with ^{111}In. The concentration of DTPA-D25E5-TAT was determined by nanodrop and adjusted to a final concentration of 6.8 mM.

5.2.8 Bioconjugation of DTPA-D25E5-TAT by SPAAC-based click chemistry

Bioconjugation of rabbit monoclonal anti-pATM antibody D25E5 with cell penetrating peptide TAT and metal ion chelating agent DTPA was achieved using SPAAC in a non-site specific manner (**Chapter 3, Figure 3.1B**). GFP-G1 was buffer exchanged in 0.1 M $NaHCO_3$ pH 8.5, concentrated to 25 μM and reacted with a seven-fold molar excess of DBCO-STP (Click Chemistry Tools, TX, USA) dissolved in DMSO at room temperature for 4 h. The antibody-DBCO conjugate was purified and buffer exchanged to PBS by centrifugal filtration using a Zeba Spin desalting column (7 K MWCO, 0.5 mL, Thermo Scientific, MA, USA). The amount of DBCO tags conjugated to the antibody was determined by absorbance spectroscopy at 280 and 309 nm, with a DBCO:antibody ratio of 5:1. The antibody-DBCO conjugate, at approximately 10 μM, was then reacted with a 2-fold molar equivalence relative to DBCO of 3.4 mM N3-Bn-DTPA dissolved in PBS + 20% DMSO (Supplementary Fig 2; see supplemental info for full synthesis details), and, concurrently, a 1-fold molar equivalence (relative to DBCO) of 1 mM azide-tagged cell penetrating peptide TAT-N_3 dissolved in PBS, Cambridge Peptides, Birmingham, UK) at 4°C for 16 h. The antibody conjugate was purified and buffer exchanged to 0.5 M sodium citrate pH 5.4 to remove unreacted products as previously described. The completion of the conjugation reaction was confirmed by the reduction of UV absorption spectrometry at 309 nm to background level. After purification, the concentration of DTPA-D25E5-TAT was determined by nanodrop and adjusted to a final concentration of 6.8 mM.

5.2.9 Radiolabelling DTPA-D25E5-TAT with $^{111}InCl_3$

Radiolabelling of immunoconjugates was carried out by addition of $^{111}InCl_3$ (Perkin Elmer, MA, USA). Aliquots of 150 μg of D25E5 conjugate (1 mg/mL in 0.5 M sodium citrate pH 5.4)

was reacted with $^{111}InCl_3$ (1 MBq/µg of antibody) in 0.5 M sodium citrate buffer pH 5.4 for 1 h at room temperature. Radiolabelling yield was determined by instant thin layer chromatography (iTLC) to be greater than 95%. The resulting radiolabelled compound ^{111}In-DTPA-D25E5-TAT was buffer exchanged to PBS to remove free $^{111}In^{3+}$ prior to subsequent studies.

5.2.10 In vitro uptake of ^{111}In-DTPA-D25E5-TAT

Aliquots of 8 x 10^4 cells/well were plated in a 24 well plate cell culture dishes and allowed to adhere overnight. Culture medium was removed, and cells washed with PBS before addition of fresh culture medium containing ^{111}In-DTPA-D25E5-TAT (1.5 nM, 1 MBq/µg) and incubation at 37°C for 60 min before irradiation/sham irradiation. After irradiation, cells were incubated at 37°C for a further 60 min before culture media, containing unbound radiolabelled compound, was collected. Cells were then washed twice with PBS before cells were washed for 5 min on ice in 0.1 M glycine pH 2.5 solution to remove membrane-bound radiolabelled antibody conjugate. Finally, cells were lysed by addition of 0.1 M NaOH, and cell-associated compound was collected. The amount of ^{111}In within each fraction was determined by automated gamma counting (Wizard^2 2480, Perkin Elmer), to calculate the percentage of cell-associated ^{111}In.

5.2.11 In vitro retention of ^{111}In-DTPA-D25E5-TAT

Aliquots of 8 x 10^4 cells/well were plated in a 24 well plate cell culture dishes and allowed to adhere for 16 h. Culture medium was removed, and cells washed with PBS before addition of fresh culture medium containing ^{111}In-DTPA-D25E5-TAT (1.5 nM, 1 MBq/µg) and incubation at 37°C for 60 min before irradiation/sham irradiation. After irradiation, cells were incubated at 37°C for a further 60 min before culture media, containing unbound radiolabelled compound,

was collected and replaced with fresh culture medium without any RIC. Cells were incubated in this media for a range of time points (0, 15, 30, 60, 120, 240, 360 min) before media containing RIC released from the cells was collected. Cells were again washed twice with PBS before being washed for 5 min on ice in 0.1 M glycine pH 2.5 solution to remove membrane-bound radiolabelled antibody conjugate. Finally, cells were lysed by addition of 0.1 M NaOH, and cell-associated compound was collected. The amount of ^{111}In within each fraction was determined by automated gamma counting (Wizard^2 2480, Perkin Elmer), to calculate the percentage of cell-associated ^{111}In. The amount of radioactivity retained was normalised to cell associated radioactivity recorded at the 0 min time point.

5.2.12 Statistical analysis

All statistical analysis was carried out using GraphPad Prism v8 (GraphPad Software, San Diego, CA, USA). Linear regression with an extra sum of squares F test was used to determine the statistical significance of correlations between estimated regression parameters. One-way ANOVA with Tukey's post hoc test, or 2-way ANOVA was used to compare grouped data to compare individual group means, as appropriate. All data was collected at least in triplicate and presented as mean ± one standard deviation unless otherwise stated.

5.3 Results

5.3.1 Validation of pATM phosphorylation kinetics

Prior to evaluation of uptake of pATM targeted RICs, the model system using lung adenocarcinoma H1299 cells stably transfected with short hairpin RNA mediated knockdown of either gene ataxia telangiectasia mutated (ATM) or a non-specific green fluorescent protein (GFP) was validated by western blot (**Figure 5.2A**). In addition to validation of ATM presence

and phosphorylation, the radiation dose activation threshold and ATM phosphorylation kinetics 24 h post irradiation were also determined (**Figure 5.2B & 5.2C**). ATM was phosphorylated (S1981) after irradiation (0.1 Gy) and demonstrated its maximum extent of

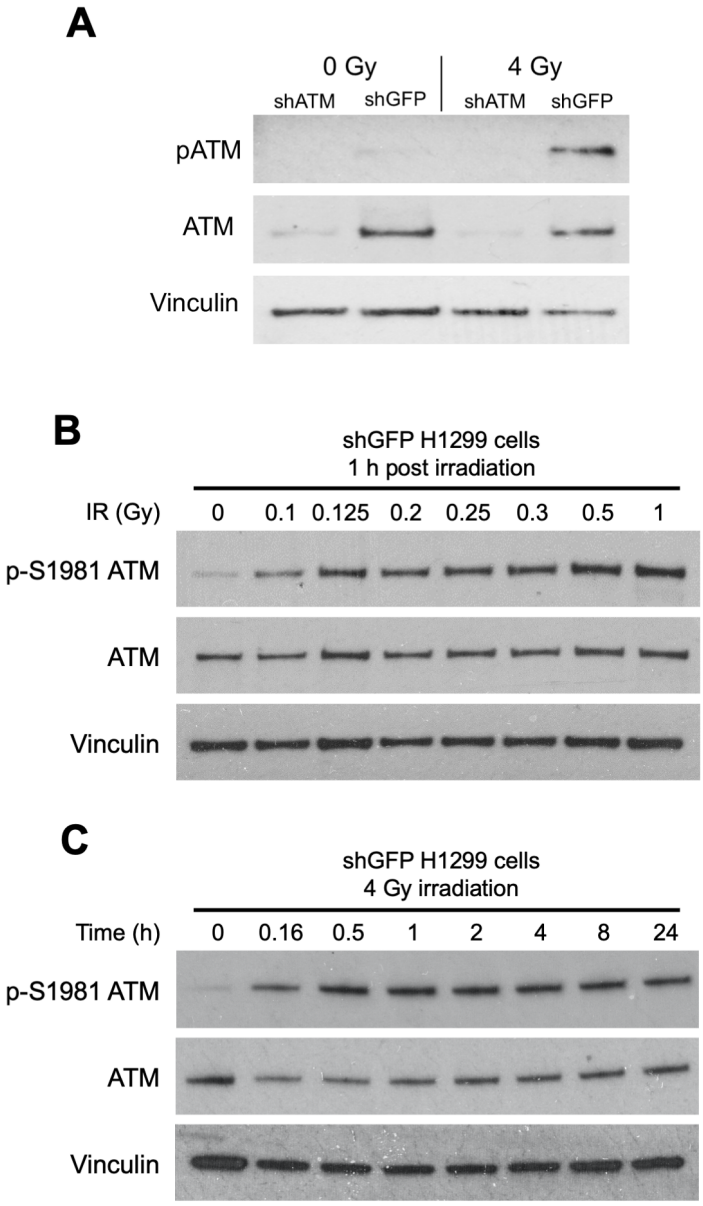


Figure 5.2) Validation of shRNA mediated knockdown of ATM and evaluation of ATM activation kinetics. A) Western blot demonstrating the difference in ATM expression between H1299 cells transfected with shRNA knockdowns of ATM (shATM) and a non-specific (shGFP) control. **B)** Western blot showing increase in ATM phosphorylation with increasing irradiation (0 - 1 Gy), cells were sampled 1 h post irradiation. **C)** Western blot showing changes in ATM phosphorylation at different time points (0 – 24 h) after 4 Gy irradiation.

phosphorylation from a radiation absorbed dose of 0.125 Gy and above. Furthermore, ATM was phosphorylated 10 min after irradiation (4 Gy) and remained phosphorylated for up to 24 h after irradiation.

5.3.2 Evaluation and selection of anti-pATM monoclonal antibodies

In order to select the optimum antibody as the targeting component of a pATM targeted RIC, a panel of several commercially available monoclonal and polyclonal antibodies were initially evaluated for performance using a combination of western blot, immunofluorescence microscopy and flow cytometry. The most promising antibody clone was D25E5 (Cell Signaling Technology, MA, USA) which demonstrated good specificity for pATM in all three assays (**Figure 5.2A, 5.3A-C**). Having selected monoclonal antibody clone D25E5 for future development, the affinity (K_D) of D25E5 was a determined by using a flow cytometry-based affinity binding assay to be 0.35 ± 0.1 nM (**Figure 5.4**).

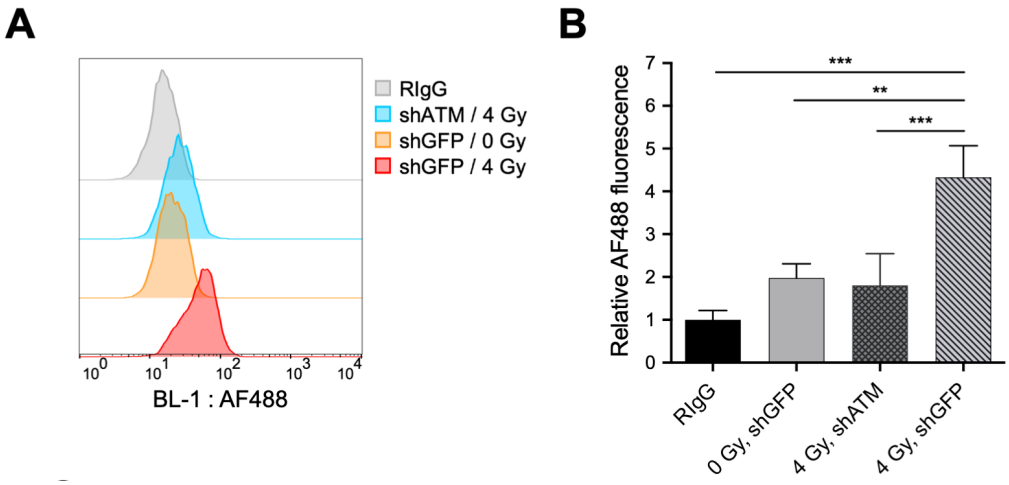


Figure 5.3) Validation of monoclonal antibody D25E5. A) Staggered histograms showing changes in binding of monoclonal antibody D25E5 to H1299 cells with shRNA mediated knockdowns of shATM and a non-specific control shGFP, following irradiation (4 Gy) or sham irradiation (0 Gy). **B)** Bar chart representation of increase in geometric mean fluorescence intensity from flow cytometry-based evaluation of monoclonal antibody D25E5. Bars represent mean ± SD ** = $P < 0.01$, *** = $P < 0.001$. [continued overleaf]

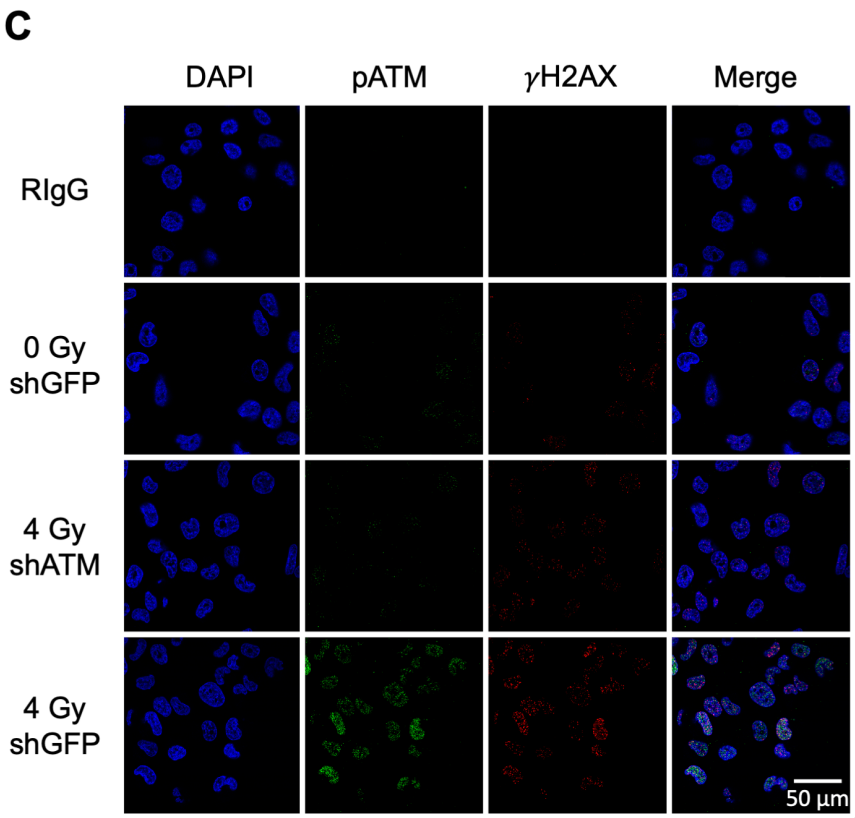


Figure 5.3) Validation of monoclonal antibody D25E5. C) Immunofluorescence microscopy showing both increase and localisation of pATM H1299 cells with shRNA mediated knockdowns of shATM and a non-specific control shGFP, following irradiation (4 Gy) or sham irradiation (0 Gy).

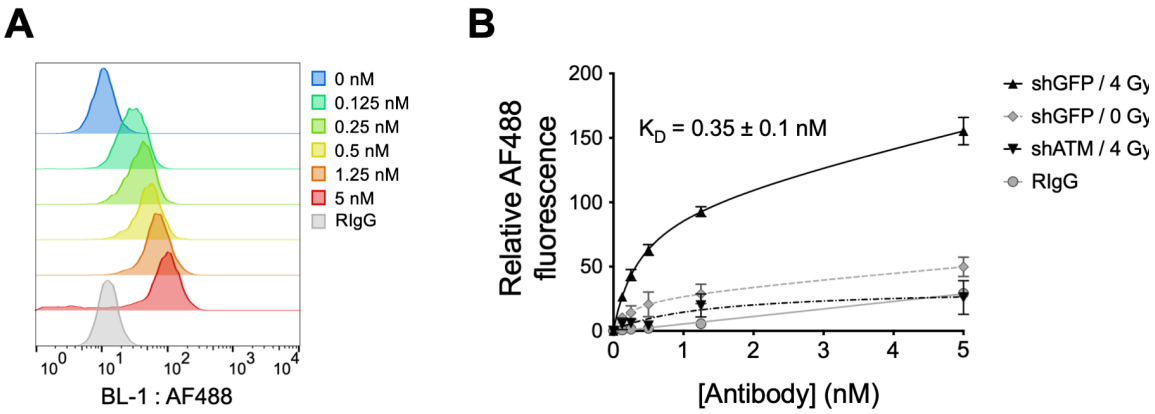


Figure 5.4) Flow cytometry-based affinity binding assay of monoclonal antibody D25E5. A) Staggered histograms showing changes in binding of monoclonal antibody D25E5 to irradiated (4 Gy) shGFP H1299 cells with increasing concentration of antibody. **B)** Plotted curve showing the fitted affinity binding curve of monoclonal antibody D25E5.

Evaluation of ^{111}In-DTPA-D25E5-TAT uptake and retention in vitro

The next stage of this project was to adapt the monoclonal antibody D25E5 into a pATM targeted RIC for evaluation of pATM binding in a cell-based model system. Initially, monoclonal antibody D25E5 was conjugated to the cell penetrating peptide TAT and chelating agent DTPA using a consecutive combination of EDC-NHS mediated crosslinking chemistry and primary amine-reactive isothiocyanate coupling, prior to radiolabelling with ^{111}In. When applied to shATM and shGFP H1299 cells in an *in vitro* radio-uptake assay. There was no significant difference in ^{111}In-DTPA-D25E5-TAT cell uptake between shGFP cells which had been irradiated (4 Gy), and shGFP cells that were not irradiated (P = 0.68, **Figure 5.5A**). Furthermore, there was no statistically significant difference between shATM and shGFP cells that have both been irradiated (P = 0.99).

In addition to using ^{111}In-DTPA-D25E5-TAT prepared by the traditional method of EDC-NHS mediated optimisation, the same assay was conducted using ^{111}In-DTPA-D25E5-TAT prepared by the optimised DBCO-N_3 based SPAAC click chemistry (**Chapter 3**). No

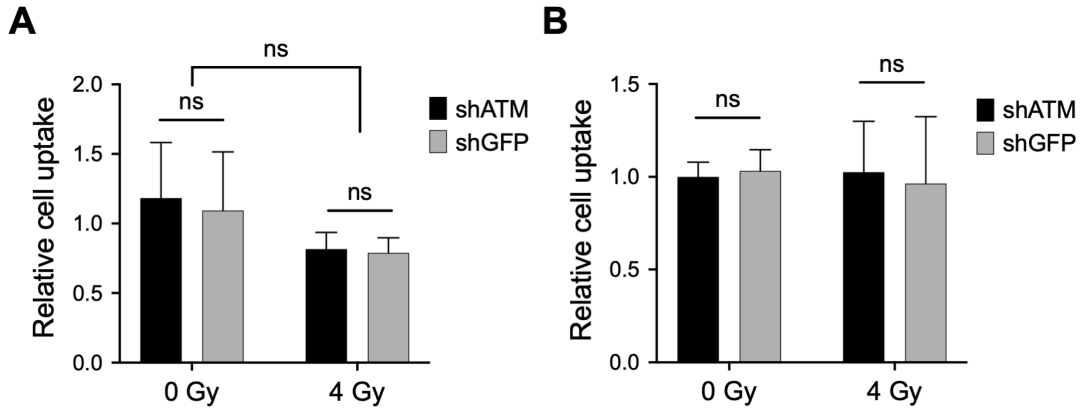


Figure 5.5) *In vitro* uptake assay of ^{111}In-DTPA-D25E5-TAT. A) Difference in relative uptake of ^{111}In-DTPA-D25E5-TAT, prepared by EDC-NHS crosslinking conjugation, in shATM and shGFP H1299 cells, with or without irradiation (4 Gy). B) Difference in relative uptake of ^{111}In-DTPA-D25E5-TAT, prepared by DBCO-N^3 click chemistry conjugation, in shATM and shGFP H1299 cells, with or without irradiation (4 Gy). Bars represent mean ± SD, ns = P > 0.05.

significant difference in relative cell uptake was observed between shGFP H1299 cells that had been irradiated (0.96 ± 0.4) or sham irradiated (1.03 ± 0.1) (P = 99, **Figure 5.5B**).

Given the lack of difference observed in cellular uptake studies, an *in vitro* cellular retention assay was carried out to determine whether cells with elevated pATM were able to retain ^{111}In-DTPA-D25E5-TAT for extended periods of time in contrast with pATM negative cells. However, there was no statistically significant difference between the rate of ^{111}In-DTPA-D25E5-TAT retention between shGFP H1299 cells that had been irradiated ($t_{1/2}$ = 84 ± 50 min) or sham irradiated ($t_{1/2}$ = 93 ± 30 min) (P = 0.41, **Figure 5.6**).

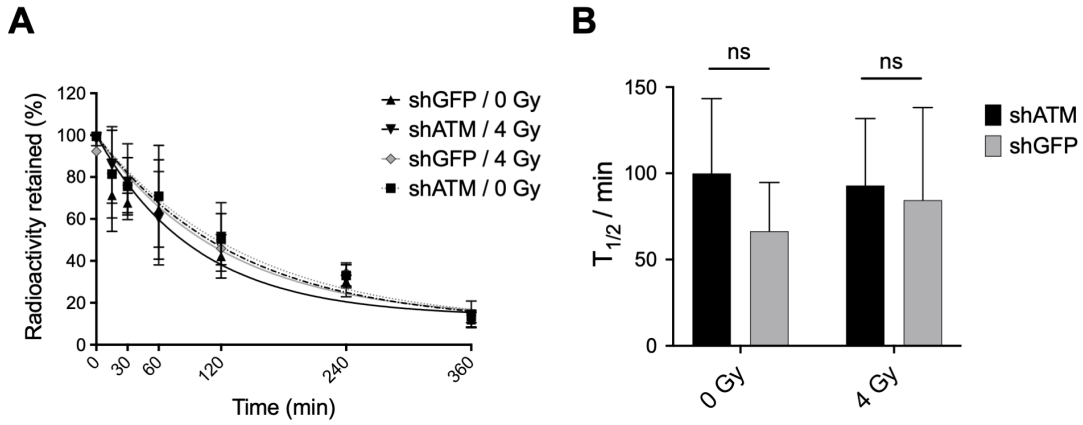


Figure 5.6) *In vitro* retention assay of ^{111}In-DTPA-D25E5-TAT. A) Radio-retention assay showing rate of release of internalised ^{111}In-DTPA-D25E5-TAT, prepared by DBCO-N_3 click chemistry conjugation in shATM and shGFP H1299 cells, with or without irradiation (4 Gy). B) Summary of half-lives of ^{111}In-DTPA-D25E5-TAT recorded from retention assays. Bars represent mean ± SD, ns = P > 0.05.

Discussion

Imaging the DNA damage response presents a plethora of potential applications, including early diagnostic tools, therapy evaluation and patient stratification. More specifically, *in vivo* imaging the phosphorylation of ATM at site Ser1981 as a surrogate marker of ATM activation may give significant insight into the cellular response to DNA double strand breaks, for

instance determining the efficacy of therapeutic drugs such as PARP and ATM inhibitors, which influence DNA damage repair, (Yi et al., 2019).

Successful imaging of pATM requires overcoming three principal challenges. Firstly, a relatively high number of proteins share the phosphorylation site consensus sequence, such as H2AX and ATR, therefore using an imaging probe with high specificity towards pATM is critical for successful imaging so as not to detect false positives. Moreover, the low estimated cellular abundance of ATM, and therefore pATM, requires an imaging probe with a high enough sensitivity to generate signal contrast in tissues where pATM is present. Finally, the subcellular localisation of pATM requires an imaging probe that is capable of crossing cellular membranes to achieve target engagement. For these reasons I decided to use a pATM targeted IgG-TAT based imaging probe as this would provide a suitable level of specificity and sensitivity with a technology I have demonstrated to work successfully with several other targets, including γH2AX, p21 and p27 (Hu et al., 2007, Cornelissen et al., 2009, Cornelissen et al., 2011).

The basis of a successful IgG-TAT based imaging probe relies on the selection of an antibody which shows good selectivity and specificity for the selected target. I evaluated the performance of several commercially available pATM monoclonal antibodies using a combination of western blot, flow cytometry and immunofluorescence microscopy as this would allow testing in a variety of settings with slightly different epitope presentations, whilst also giving insight into the subcellular location of candidate antibody binding. The monoclonal antibody clone D25E5 demonstrated the best all round performance across each assay and was therefore selected for development of an anti-pATM imaging probe (**Figure 5.3**). A flow cytometry-based affinity binding assay demonstrated that D25E5 has a favourable affinity for pATM (K_d = 0.35 ± 10 nM) (**Figure 5.4**). For reference, the clinically approved anti-ErbB2 monoclonal antibody Herceptin has a K_D of 5 nM (De Lorenzo et al., 2005). It is important to

note, however, that due to the limited availability of D25E5 antibody, I were unable to evaluate whether or not the process of conjugation affected the affinity of D25E5.

In vitro evaluation demonstrated that both uptake and retention of ^{111}In-DTPA-D25E5-TAT was not distinguishable between pATM positive and pATM negative H1299 cells. Although a multitude of factors influence specific uptake of an RIC, target abundance is critical for generating a sufficient signal to overcome both fundamental detection limits and signals arising from non-specific binding. Reports utilising high throughput mass spectrometry techniques project the endogenous copy number of ATM to range between 0.5 and 5.0 x 10^4 copies per cell with variation between the cell lines tested (Bekker-Jensen et al., 2017, Wisniewski et al., 2014, Beck et al., 2011). Furthermore, research investigating pATM phosphorylation dynamics has shown that only 60% of total ATM is phosphorylated at site Ser1981 after 5 Gy irradiation (Kozlov et al., 2011). Research presented in previous chapters using a nucleus-bound GFP model system in conjunction with a GFP-targeted IgG-TAT RIC indicated a lower target abundance threshold of approximately 1.8 x 10^5 copies per cell (**Chapter 4**), suggesting that the endogenous expression level of ATM may not high enough for imaging using an IgG-TAT based RIC. However, it should be noted that other features, such as antibody affinity, will also likely affect the lower abundance detection threshold.

Given that the cellular abundance of pATM may not be sufficient for IgG-TAT based molecular imaging, future research should be focused on investigating alternative strategies for imaging ATM activation. One such strategy could involve utilising an IgG-TAT based RIC to image a more abundant protein which is phosphorylated, preferably exclusively, by pATM. One example would be KRAB-associated protein 1 (KAP1). KAP1 is a multifunctional regulator of a range of cellular processes, including transcriptional co-repression and degradation of tumour suppressor p53 (Czerwinska et al., 2017). As part of the DNA damage response, KAP1 is phosphorylated predominantly by ATM at Ser824, which disrupts the

interaction of KAP1 with chromatin remodelling factors, thereby relaxing the structure of chromatin and promoting accessibly of DDR factors around the damaged site (Ziv et al., 2006). The endogenous expression level of KAP1 has been estimated to be between 0.15 and 5 x 10^6 copies per cell, which would be considerably more favourable for IgG-TAT-based imaging (Wisniewski et al., 2014).

Alternative approaches towards imaging ATM *in vivo* could involve utilising a different type of imaging probe altogether. Recent advances in radiochemical synthesis pathways have made it possible to incorporate radioisotopes, such as ^{11}C into highly potent and selective small molecule inhibitors of ATM (ATMi) (Durant et al., 2018). For instance, PET imaging using a ^{11}C radiolabelled ATMi, [^{11}C]AZD1390, has been used to demonstrate that AZD1390 can penetrate the blood brain barrier, highly relevant for the treatment of glioblastoma multiforme (GBM) (Jucaite et al., 2020). Although it is not stated whether or not the affinity for AZD1390 for ATM is different for the active and inactive conformations of ATM and therefore might not be suitable for imaging activation of ATM.

In summary, this chapter involved an attempt to image pATM, a technically challenging intranuclear epitope, using an IgG-TAT-based RIC as a means of non-invasively monitor the DDR *in vivo*. Although unsuccessful in its primary objective, the information gained form this research will no doubt be useful for future projects involving IgG-TAT based intranuclear imaging.

Chapter 6

Discussion and future work

6.1 Conclusion and future directions

6.1.1 General aims

The development and utilisation of monoclonal antibodies represents one of the most significant advances in molecular biology and clinical research over the last half century. Within the burgeoning field of nuclear medicine, antibody-based molecular imaging has already shown great potential for a range of applications. Within this thesis, I attempted to gain a greater understanding of how I can utilise the unique properties of monoclonal antibodies to image targets within the cell nucleus, thus broadening the scope of this relatively new technology.

The principle aim of this project was to test the limits of IgG-TAT based molecular imaging of intranuclear epitopes, and more specifically the lower target abundance threshold required for detection for PET/SPECT imaging *in vivo*. The H2B-EGFP model system allowed us to evaluate the lower detection limits of IgG-TAT-based intranuclear imaging. This proof-of-concept study indicated a detection threshold *in vitro* of approximately 180,000 copies per cell and *in vivo* 240,000 copies per cell. Whilst this can be considered a triumph, it also highlights that this technology requires significant improvement and refinement before being genuinely considered for clinical translation. In Chapter 3, I began this optimisation with a development of the N_3-DBCO conjugation strategy to label the monoclonal antibody GFP-G1 with the cell penetrating peptide TAT and chelator DTPA. Despite this optimisation, I were unable to

successfully detect the phosphorylation of the DNA damage response protein ATM using IgG-TAT based RICs. Whilst unsuccessful in this aspect, this model does provide a platform for future development of antibody-based intranuclear imaging that could make imaging targets such as phospho-ATM possible in the future. In this chapter I will discuss which areas of antibody-based intranuclear PET/SPECT could be improved in future research.

6.1.2 H2B-EGFP / GFP-G1 model system

One of the clearest benefits of antibody based molecular imaging is the combination of versatility and sensitivity that opens up the potential to image an incredibly broad range of epitopes with predictable bioavailability and pharmacokinetic properties. Such a range of targeting capabilities prompts the question of characteristics make an epitope of interest a suitable target? Whilst previous research has already demonstrated that intranuclear PET/SPECT imaging using IgG-TAT RICs is possible on a small collection of nuclear targets, no prior study has attempted to define what the quantitative limits of target abundance for IgG-TAT based molecular imaging.

The majority of research utilising IgG-TAT PET/SPECT imaging has been focused on specific applications, for instance imaging γH2AX as a means of gauging the extent of DNA damage. In these cases, the abundance of the target changes with external intervention, such as ionising irradiation, making quantitative evaluation of target abundance difficult, especially *in vivo*. By using multiple clones constitutively expressing different levels of a target, I could reliably evaluate how changes in target abundance effect RIC uptake, *in vitro* and *in vivo*.

The H2B-EFGP model system had several advantages as a means to generate an adequate model system. Firstly, the H2B-GFP plasmid was readily available and has been used successfully in a variety of cell lines using reasonably simple transfection protocols. Furthermore, the fluorescent nature of EGFP was useful for selection of clones with a range of

expression levels without requiring immunoassays such as ELISA or western blot with potential sources of variation. Finally, the availability of a previously validated anti GFP hybridoma cell line was highly beneficial as this allowed for exploration and optimisation of the conjugation approach and refinement of assays *in vitro*. However, this model system also has notable drawbacks which should be addressed in future research, firstly, I was unable to generate a stable H2B-EGFP clone with a copy number less than 180,000 copies per cell. This could be a result of antibiotic selection removing stably transfected clones with low transfection levels due to lack of G418 resistance gene expression. Furthermore, culture *in vitro* without G418 for 6 weeks showed a marked decrease in H2B-EGFP expression in two of the four selected clones. Although this could be controlled *in vitro* with antibiotic selection, this could not be applied *in vivo*. Future research could utilise a lentiviral transfection method to improve both the stability and ideally the range of H2B-EGFP expression, possibly in an array of cell lines derived from different cancers to produce a more systematic platform for further optimisation of CPP-based immuno-PET/SPECT imaging (Naldini et al., 2016).

6.1.3 Imaging alternative cellular compartments

The H2B-EGFP model system was designed to test the limits of antibody-based PET/SPECT imaging of intranuclear targets, however the eukaryotic cell features several other organelles and cellular compartments, such as the Golgi apparatus or the inner leaflet of the plasma membrane. To further broaden the range of applications of antibody-based intracellular imaging, it would be useful to determine whether or not a similar approach could be used to target proteins expressed in other cellular compartments. By transfecting expressing GFP fused to an intracellular trafficking motif, such as the CAAX tetrapeptide motif (C = cysteine, A = aliphatic amino acid, X = terminal amino acid), which is a signal for translocation to the inner leaflet of the plasma membrane used by the Ras superfamily of GTPases, I could modify the

intracellular location of GFP expression to evaluate whether this technology is capable of detecting epitopes at other cellular locations (Berndt et al., 2011).

6.1.4 Conjugation strategies

In chapter 3, I developed a conjugation approach (DBCO-N_3) with the goal of improving specific uptake of TAT-IgG RICs in comparison to the current conventional method of EDC-NHS mediated crosslinking. Indeed, anti-GFP RICs produced using the DBCO-N_3 method did show increased uptake in the H2B-EGFP positive cell line H2B-EGFP 45 *in vitro* relative to the alternative EDC-NHS conjugated equivalent. However, there was also an increase in non-specific uptake, in part negating the increased specific uptake. The first point of research should be to see whether this result *in vitro* translates to an *in vivo* model, which could be carried out using the H2B-EGFP clone xenograft model used in this project.

It is important to note that there is an abundance of alternative conjugation strategies could be utilised to ensure a more controllable and consistent conjugation ratio and placement (Dennler et al., 2015). The main advantage of both the DBCO-N_3 and traditional EDC-NHS methods is that they modify naturally occurring amino acid side chains and can therefore be applied to almost any monoclonal antibody or antibody fragment of interest. However, this degree of versatility comes with the significant cost in heterogeneity in both conjugate to IgG ratios and conjugate placement, making thorough characterisation and optimisation difficult.

One outstanding question that must be addressed is what is the ratio of TAT to IgG molecule achieved when using these alternative methods? Furthermore, what difference does the TAT to IgG ratio have on specific, and non-specific uptake of RICs? It is well documented across a range of applications that the ratio of covalently bound CPP to cargo protein can influence the degree of CPP-cargo conjugate uptake (Sung et al., 2006). By using a combination of absorbance of the DBCO linker in conjunction with the N_3-modified fluorophore sulfo-Cy5-

N_3, I inferred a TAT-IgG ratio of approximately 1.5:1, however this needs to be explicitly confirmed using mass spectrometry.

In this thesis, CPP TAT and chelator DTPA were simultaneously conjugated onto the relevant antibody, which resulted in potential obscurity in the exact ratios of both moieties onto the antibody. On potential refinement of this method could be to sequentially conjugate TAT-N_3 and DTPA-Bn-N_3 and observing the reduction in absorbance at 309 nm for each reaction, thereby giving greater clarity over the relative degrees of TAT and DTPA conjugation ratios. Future research should seek to implement this refined DBCO-N_3 conjugation strategy to titrate the TAT-IgG ratio to determine what is optimal for imaging *in vivo*. Although this refinement would improve insight into TAT-IgG ratios overall, it would still not offer a homogenous level of TAT conjugation across each individual IgG molecule, resulting in potentially inconsistent performance.

Furthermore, the N3-DBCO conjugation method is also unable to label antibodies in a site specific manner. Research by Gaston and co-workers used genetic modification to tag a whole antibody with a selection of CPPs at different sites to evaluate changes in cytosolic delivery of the CPP-IgG fusion protein (Gaston et al., 2019). Interestingly, the study showed that uptake of CPP-IgG fusion proteins can be dramatically changed by the location of the CPP. Given that the hybridoma cell line is available, future research could implement a similar approach, using genetic engineering to directly incorporate TAT, or other CPPs into a CPP-GFP-G1 fusion protein for a more thorough analysis of how the location and stoichiometry of CPP conjugation determines RIC uptake.

6.1.5 Cell penetrating peptide optimisation

Cell penetrating peptides, since their discovery over 30 years ago, continue to grow as an exciting field of research and are considered to be one of the most useful methods of

intracellular macromolecule delivery (Xie et al., 2020). In this project, I utilised the cationic CPP TAT as a means to deliver an antibody-based RIC to the nucleus of a cell, demonstrating an increase in specific uptake in comparison to a non-TAT modified RIC. However, conjugation of TAT also increases non-specific cellular uptake, potentially compromising ultimate sensitivity by masking specific uptake of low abundance targets.

Despite initial controversy, the general consensus is that CPPs are delivered into the cell by some form of endocytosis. One of the major challenges currently facing CPP mediated intracellular delivery is endosomal entrapment, where a CPP-cargo complex is unable to reach the cytosol of the cell and is instead trafficked to a lysosome and degraded. Several reports have indicated The CPP TAT has been shown to have poor endosomal escape capacity and that this is the rate limited step of TAT-mediated cell penetration (Lee et al., 2008, Lonn et al., 2016). Therefore, the choice of TAT as a CPP for antibody-based intranuclear imaging could well be compromising attempts to image low abundance targets, such as phospho-ATM.

In order to combat the relatively poor cytosolic delivery of TAT-based conjugates, several groups have been able to improve cytosolic delivery through additional modification of TAT, including the addition of ‘endosome escape domains’ (Lonn et al., 2016), multivalent TAT constructs (Allen et al., 2018), and even cyclic derivatives of TAT (Nischan et al., 2015). In addition, several non-TAT based CPPs have shown far superior cytosolic delivery of TAT-cargo complexes, including the cyclic polyarginine-based CPP12 (Qian et al., 2016). It is also important to note that the majority of research caried out to optimise CPP mediated intracellular delivery of antibody-based conjugates utilises an antibody targeted at an extracellular epitope, thereby targeting the CPP-antibody complex to the target cell before internalisation. However, in this project, initial internalisation of the CPP-antibody conjugate is not cell-specific, and the antibody is targeted at an intranuclear target (H2B-EGFP). This distinction is critical as an intracellular targeted RIC must not only be optimised for cytosolic delivery, but also for cell

export in cells which do not contain the target epitope. Future research could use the model system established in this project to evaluate a panel of CPPs to find which is best suited for antibody-based intranuclear PET/SPECT imaging.

6.1.6 Whole IgG versus antibody fragments

Research and development around monoclonal antibodies has rendered a myriad of engineered antibody-based fragments, each of which has distinct characteristics that can be tailored for specific applications (Strohl, 2018). Whole, intact antibodies are relatively large molecules. which can have profound consequences for the characteristics and performance of an imaging probe for several reasons. Firstly, at the cellular level, it has been demonstrated that CPP mediate internalisation is less efficient with larger cargo proteins (Tunnemann et al., 2006) and it is also unclear whether the efficiency of endosomal escape is affected by the size of the cargo protein. At the organismal level, the molecular mass of the probe will determine the clearance pathway, serum longevity, tumour uptake and penetration.

Intriguingly, the characteristics of an IgG-based RIC could have both positive and negative consequences for imaging of lowly expressed targets *in vivo*. On one hand, the long serum persistence and high tumour uptake as a result of the EPR effect promotes maximal engagement of the probe with the target (Xenaki et al., 2017). However, these benefits are offset by the significant degree of non-specific uptake caused by the EPR effect, resulting in poor contrast, compromising sensitivity (Wu, 2014). In the context of CPP-mediated intranuclear imaging, it is unclear whether or not a smaller targeted vector, such as a cys-diabody (~55 kDa) would improve the lower abundance detection threshold. Future research should exploit the availability of the GFP-G1 hybridoma cell line, and thus the sequence of the variable domains, to produce a selection of anti-GFP antibody fragments to gather a better understanding of the effect on molecular mass on the efficacy of intracellular immuno-PET/SPECT imaging.

6.1.7 Intranuclear immuno-PET using PET, SPECT or both?

Throughout this project, the SPECT radioisotope ^{111}In in conjunction with the radiometal chelator DTPA has been used exclusively for both *in vitro* and *in vivo* research. This combination was selected as it is a reliable and reproducible method of producing RICs suitable for pre-clinical molecular imaging studies. However, for the purposes of clinical translation, PET possesses several advantages over SPECT, including superior spatial resolution, sensitivity and easier attenuation correction and thus quantification (Wernick and Aarsvold, 2004). One particularly attractive radioisotope for immuno-PET is ^{89}Zr, which has a radioactive half-life of 78.4 h, matching the biological half-life of whole antibodies (van de Watering et al., 2014). Furthermore, the relatively low energy of positrons released from ^{89}Zr (average energy 395 keV) allows for higher resolution imaging in contrast to other PET radioisotopes. Several previous reports have already demonstrated intranuclear PET using ^{89}Zr radiolabelled IgG-TAT RICs, combining a γH2AX targeted antibody with the chelator desferoxamine (DFO) (Knight et al., 2015, Poty et al., 2020). A relatively simple modification would allow the N_3-DBCO conjugation method to be adapted for the conjugation of DFO instead of DTPA, allowing for radiolabelling with ^{89}Zr to take advantage of the benefits of PET over SPECT.

One notable advantage of SPECT over PET is the capacity for multiplexing. Multi-isotope SPECT or SPECT/PET imaging uses a combination of SPECT or PET isotopes to effectively image two, or more, features of a biological system at the same time and has already been used in a variety of applications, including in the clinic (Hsieh et al., 2010, van der Bruggen et al., 2010). Previously, Knight et al. combined a ^{89}Zr-radioabelled monoclonal antibody specific for human epidermal growth factor receptor 2 (HER2) with an ^{111}In-radiolabelled non-specific isotype control antibody to distinguish between specific and non-specific tumour uptake (Knight et al., 2019b). An interesting experiment would involve a similar approach, using the DBCO-N_3 approach to produce a ^{89}Zr-radiolabelled GFP-G1-TAT RIC and an ^{111}In-

radiolabelled TAT-conjugated isotype control, or a scrambled GFP-G1 mutant antibody, to demonstrate the degree of non-specific uptake of TAT-IgG RICs in the same subject.

6.1.8 IgG-TAT targeted Auger electron radioimmunotherapy

In addition to performing imaging and diagnostic tasks, antibody-based radiopharmaceuticals have also been utilised for therapeutic applications for delivery of cytotoxic radionuclide warheads, otherwise known as radioimmunotherapy (RIT) (Koppe et al., 2005). Despite relatively limited translation into clinical translation so far with only two RIT agents gaining approval from the United States FDA, the rapid development novel antibody formats, conjugation strategies and more stable radiometal chelators has generated a burgeoning area of research around RIT (White et al., 2021).

Auger electrons (AEs) are very low energy (<25 keV) electrons, which are emitted by radionuclides that undergo decay by electron capture (Ku et al., 2019). Despite their low energy, AEs deposit this energy over extremely short distances (1 nm – 30 μm), allowing for the delivery of extremely localised, moderate to high linear energy transfer (LET) radiation to a target location (Cornelissen and Vallis, 2010). Because of this short range, AE radiotherapy requires the radionuclide to be brought into very close proximity to the target, often requiring some form of internalising motif in conjunction with an antibody that targets an epitope expressed on the cell surface. In this thesis, I successfully demonstrated the ability to engage a nucleus bound epitope using a TAT-IgG RIC. It is therefore plausible to use a similar approach to deliver a therapeutic dose of an AE emitting radionuclide, such as ^{111}In or ^{123}I, directly to a target located within the cell nucleus, producing a highly specific and potent RIT agent. Future research should explore the therapeutic capabilities of TAT-IgG RICs in addition to imaging applications, further increasing the versatility of this technology.

6.1.9 Closing remarks: The end of the beginning

Molecular imaging using antibodies is a rapidly expanding field with a clear and potential for an variety of research and clinical applications. This project set out to define what is currently possible with antibody-based intranuclear PET/SPECT imaging, whilst simultaneously providing a platform for future optimisation of this imaging technique. In this respect, this project has been largely successful. However, as with all worthwhile scientific endeavours, this project has ultimately generated more questions than answers surrounding this exciting, yet enigmatic, technology. Hopefully this research will prove to be a catalyst for the future development of more powerful antibody-based molecular imaging devices.

Bibliography

AGRAWAL, P., BHALLA, S., USMANI, S. S., SINGH, S., CHAUDHARY, K., RAGHAVA, G. P. & GAUTAM, A. 2016. CPPsite 2.0: a repository of experimentally validated cell-penetrating peptides. *Nucleic Acids Res,* 44**,** D1098-103.

AGUILERA, T. A., OLSON, E. S., TIMMERS, M. M., JIANG, T. & TSIEN, R. Y. 2009. Systemic in vivo distribution of activatable cell penetrating peptides is superior to that of cell penetrating peptides. *Integr Biol (Camb),* 1**,** 371-81.

ALAM, I. S., ARSHAD, M. A., NGUYEN, Q. D. & ABOAGYE, E. O. 2015. Radiopharmaceuticals as probes to characterize tumour tissue. *Eur J Nucl Med Mol Imaging,* 42**,** 537-61.

ALBERTS, B., JOHNSON, A., LEWIS, J., RAFF, M., ROBERTS, K. & WALTER, P. 2008. *Molecular biology of the cell,* NY, Garland Science.

ALLEN, J. K., BROCK, D. J., KONDOW-MCCONAGHY, H. M. & PELLOIS, J. P. 2018. Efficient Delivery of Macromolecules into Human Cells by Improving the Endosomal Escape Activity of Cell-Penetrating Peptides: Lessons Learned from dfTAT and its Analogs. *Biomolecules,* 8.

ALVES, N. J., CHAMPION, M. M., STEFANICK, J. F., HANDLOGTEN, M. W., MOUSTAKAS, D. T., SHI, Y., SHAW, B. F., NAVARI, R. M., KIZILTEPE, T. & BILGICER, B. 2013. Selective photocrosslinking of functional ligands to antibodies via the conserved nucleotide binding site. *Biomaterials,* 34**,** 5700-5710.

BAKKENIST, C. J. & KASTAN, M. B. 2003. DNA damage activates ATM through intermolecular autophosphorylation and dimer dissociation. *Nature,* 421**,** 499-506.

BANAN, M. 2020. Recent advances in CRISPR/Cas9-mediated knock-ins in mammalian cells. *J Biotechnol,* 308**,** 1-9.

BARNEA, I., BEN-YOSEF, R., KARAUSH, V., BENHAR, I. & VEXLER, A. 2013. Targeting EGFR-positive cancer cells with cetuximab–ZZ-PE38: Results of in vitro and in vivo studies. *Head & neck,* 35**,** 1171-1177.

BARTKOVA, J., HOREJSI, Z., KOED, K., KRAMER, A., TORT, F., ZIEGER, K., GULDBERG, P., SEHESTED, M., NESLAND, J. M., LUKAS, C., ORNTOFT, T., LUKAS, J. & BARTEK, J. 2005. DNA damage response as a candidate anti-cancer barrier in early human tumorigenesis. *Nature,* 434**,** 864-70.

BECK, A., GOETSCH, L., DUMONTET, C. & CORVAÏA, N. 2017. Strategies and challenges for the next generation of antibody–drug conjugates. *Nature reviews Drug discovery,* 16**,** 315-337.

BECK, M., SCHMIDT, A., MALMSTROEM, J., CLAASSEN, M., ORI, A., SZYMBORSKA, A., HERZOG, F., RINNER, O., ELLENBERG, J. & AEBERSOLD, R. 2011. The quantitative proteome of a human cell line. *Mol Syst Biol,* 7**,** 549.

BEERS, S. A., GLENNIE, M. J. & WHITE, A. L. 2016. Influence of immunoglobulin isotype on therapeutic antibody function. *Blood,* 127**,** 1097-101.

BEKKER-JENSEN, D. B., KELSTRUP, C. D., BATTH, T. S., LARSEN, S. C., HALDRUP, C., BRAMSEN, J. B., SORENSEN, K. D., HOYER, S., ORNTOFT, T. F., ANDERSEN, C. L., NIELSEN, M. L. & OLSEN, J. V. 2017. An Optimized Shotgun Strategy for the Rapid Generation of Comprehensive Human Proteomes. *Cell Syst,* 4**,** 587-599 e4.

BERNARDIM, B., MATOS, M. J., FERHATI, X., COMPAÑÓN, I., GUERREIRO, A., AKKAPEDDI, P., BURTOLOSO, A. C. B., JIMÉNEZ-OSÉS, G., CORZANA, F. & BERNARDES, G. J. L. 2019. Efficient and irreversible antibody–cysteine bioconjugation using carbonylacrylic reagents. *Nature Protocols,* 14**,** 86-99.

BERNDT, N., HAMILTON, A. D. & SEBTI, S. M. 2011. Targeting protein prenylation for cancer therapy. *Nat Rev Cancer,* 11**,** 775-91.

BLACKFORD, A. N. & JACKSON, S. P. 2017. ATM, ATR, and DNA-PK: The Trinity at the Heart of the DNA Damage Response. *Mol Cell,* 66**,** 801-817.

CARDOZO, A. K., BUCHILLIER, V., MATHIEU, M., CHEN, J., ORTIS, F., LADRIERE, L., ALLAMAN-PILLET, N., POIROT, O., KELLENBERGER, S., BECKMANN, J. S., EIZIRIK, D. L., BONNY, C. & MAURER, F. 2007. Cell-permeable peptides induce dose- and length-dependent cytotoxic effects. *Biochim Biophys Acta,* 1768**,** 2222-34.

CAREY, D. J. 1997. Syndecans: multifunctional cell-surface co-receptors. *The Biochemical journal,* 327 (Pt 1)**,** 1-16.

CARTER, L. M., POTY, S., SHARMA, S. K. & LEWIS, J. S. 2018. Preclinical optimization of antibody-based radiopharmaceuticals for cancer imaging and radionuclide therapy-Model, vector, and radionuclide selection. *J Labelled Comp Radiopharm,* 61**,** 611-635.

CARTER, P. 2001. Improving the efficacy of antibody-based cancer therapies. *Nat Rev Cancer,* 1**,** 118-29.

CASTELLI, M. S., MCGONIGLE, P. & HORNBY, P. J. 2019. The pharmacology and therapeutic applications of monoclonal antibodies. *Pharmacology Research & Perspectives,* 7**,** e00535.

CONNER, S. D. & SCHMID, S. L. 2003. Regulated portals of entry into the cell. *Nature,* 422**,** 37-44.

CONTI, M. & ERIKSSON, L. 2016. Physics of pure and non-pure positron emitters for PET: a review and a discussion. *EJNMMI physics,* 3**,** 8-8.

CORNELISSEN, B., ABLE, S., KARTSONAKI, C., KERSEMANS, V., ALLEN, P. D., CAVALLO, F., CAZIER, J. B., IEZZI, M., KNIGHT, J., MUSCHEL, R., SMART, S.

& VALLIS, K. A. 2014. Imaging DNA damage allows detection of preneoplasia in the BALB-neuT model of breast cancer. *J Nucl Med,* 55**,** 2026-31.

CORNELISSEN, B., KERSEMANS, V., DARBAR, S., THOMPSON, J., SHAH, K., SLEETH, K., HILL, M. A. & VALLIS, K. A. 2011. Imaging DNA damage in vivo using gammaH2AX-targeted immunoconjugates. *Cancer Res,* 71**,** 4539-49.

CORNELISSEN, B., KERSEMANS, V., MCLARTY, K., TRAN, L., VALLIS, K. A. & REILLY, R. M. 2009. In vivo monitoring of intranuclear p27(kip1) protein expression in breast cancer cells during trastuzumab (Herceptin) therapy. *Nucl Med Biol,* 36**,** 811-9.

CORNELISSEN, B. & VALLIS, K. A. 2010. Targeting the nucleus: an overview of Auger-electron radionuclide therapy. *Curr Drug Discov Technol,* 7**,** 263-79.

CROCE, C. M. 2008. Oncogenes and Cancer. *New England Journal of Medicine,* 358**,** 502-511.

CZERWINSKA, P., MAZUREK, S. & WIZNEROWICZ, M. 2017. The complexity of TRIM28 contribution to cancer. *J Biomed Sci,* 24**,** 63.

DAMMES, N. & PEER, D. 2020. Monoclonal antibody-based molecular imaging strategies and theranostic opportunities. *Theranostics,* 10**,** 938-955.

DANIEL, J. A., PELLEGRINI, M., LEE, J. H., PAULL, T. T., FEIGENBAUM, L. & NUSSENZWEIG, A. 2008. Multiple autophosphorylation sites are dispensable for murine ATM activation in vivo. *J Cell Biol,* 183**,** 777-83.

DE LORENZO, C., COZZOLINO, R., CARPENTIERI, A., PUCCI, P., LACCETTI, P. & D'ALESSIO, G. 2005. Biological properties of a human compact anti-ErbB2 antibody. *Carcinogenesis,* 26**,** 1890-5.

DENNLER, P., FISCHER, E. & SCHIBLI, R. 2015. Antibody conjugates: from heterogeneous populations to defined reagents. *Antibodies,* 4**,** 197-224.

DEROSSI, D., CHASSAING, G. & PROCHIANTZ, A. 1998. Trojan peptides: the penetratin system for intracellular delivery. *Trends Cell Biol,* 8**,** 84-7.

DEROSSI, D., JOLIOT, A. H., CHASSAING, G. & PROCHIANTZ, A. 1994. The third helix of the Antennapedia homeodomain translocates through biological membranes. *J Biol Chem,* 269**,** 10444-50.

DEWULF, J., ADHIKARI, K., VANGESTEL, C., WYNGAERT, T. V. D. & ELVAS, F. 2020. Development of Antibody Immuno-PET/SPECT Radiopharmaceuticals for Imaging of Oncological Disorders-An Update. *Cancers (Basel),* 12.

DOMMERHOLT, J., RUTJES, F. & VAN DELFT, F. L. 2016. Strain-Promoted 1,3-Dipolar Cycloaddition of Cycloalkynes and Organic Azides. *Top Curr Chem (Cham),* 374**,** 16.

DONATE-MACIAN, P., ALVAREZ-MARIMON, E., SEPULCRE, F., VAZQUEZ-IBAR, J. L. & PERALVAREZ-MARIN, A. 2019. The Membrane Proximal Domain of TRPV1 and TRPV2 Channels Mediates Protein(-)Protein Interactions and Lipid Binding In Vitro. *Int J Mol Sci,* 20.

DUCHARDT, F., FOTIN-MLECZEK, M., SCHWARZ, H., FISCHER, R. & BROCK, R. 2007. A comprehensive model for the cellular uptake of cationic cell-penetrating peptides. *Traffic,* 8**,** 848-66.

DURANT, S. T., ZHENG, L., WANG, Y., CHEN, K., ZHANG, L., ZHANG, T., YANG, Z., RICHES, L., TRINIDAD, A. G., FOK, J. H. L., HUNT, T., PIKE, K. G., WILSON, J., SMITH, A., COLCLOUGH, N., REDDY, V. P., SYKES, A., JANEFELDT, A., JOHNSTROM, P., VARNAS, K., TAKANO, A., LING, S., ORME, J., STOTT, J., ROBERTS, C., BARRETT, I., JONES, G., ROUDIER, M., PIERCE, A., ALLEN, J., KAHN, J., SULE, A., KARLIN, J., CRONIN, A., CHAPMAN, M., VALERIE, K., ILLINGWORTH, R. & PASS, M. 2018. The brain-penetrant clinical ATM inhibitor

AZD1390 radiosensitizes and improves survival of preclinical brain tumor models. *Sci Adv,* 4**,** eaat1719.

EFTHYMIADIS, A., BRIGGS, L. J. & JANS, D. A. 1998. The HIV-1 Tat nuclear localization sequence confers novel nuclear import properties. *J Biol Chem,* 273**,** 1623-8.

EL-ANDALOUSSI, S., JARVER, P., JOHANSSON, H. J. & LANGEL, U. 2007. Cargo-dependent cytotoxicity and delivery efficacy of cell-penetrating peptides: a comparative study. *Biochem J,* 407**,** 285-92.

FASS, L. 2008. Imaging and cancer: a review. *Mol Oncol,* 2**,** 115-52.

FERRARI, A., PELLEGRINI, V., ARCANGELI, C., FITTIPALDI, A., GIACCA, M. & BELTRAM, F. 2003. Caveolae-mediated internalization of extracellular HIV-1 tat fusion proteins visualized in real time. *Mol Ther,* 8**,** 284-94.

FRANKEL, A. D. & PABO, C. O. 1988. Cellular uptake of the tat protein from human immunodeficiency virus. *Cell,* 55**,** 1189-93.

FREISE, A. C. & WU, A. M. 2015. In vivo imaging with antibodies and engineered fragments. *Mol Immunol,* 67**,** 142-52.

FREITAS, N. & CUNHA, C. 2009. Mechanisms and signals for the nuclear import of proteins. *Curr Genomics,* 10**,** 550-7.

FRETZ, M. M., PENNING, N. A., AL-TAEI, S., FUTAKI, S., TAKEUCHI, T., NAKASE, I., STORM, G. & JONES, A. T. 2007. Temperature-, concentration- and cholesterol-dependent translocation of L- and D-octa-arginine across the plasma and nuclear membrane of CD34+ leukaemia cells. *Biochem J,* 403**,** 335-42.

FUNHOFF, A. M., VAN NOSTRUM, C. F., KONING, G. A., SCHUURMANS-NIEUWENBROEK, N. M., CROMMELIN, D. J. & HENNINK, W. E. 2004. Endosomal escape of polymeric gene delivery complexes is not always enhanced by polymers buffering at low pH. *Biomacromolecules,* 5**,** 32-9.

GALLAMINI, A., ZWARTHOED, C. & BORRA, A. 2014. Positron Emission Tomography (PET) in Oncology. *Cancers (Basel),* 6**,** 1821-89.

GAO, C., MAO, S., DITZEL, H. J., FARNAES, L., WIRSCHING, P., LERNER, R. A. & JANDA, K. D. 2002. A cell-penetrating peptide from a novel pVII-pIX phage-displayed random peptide library. *Bioorg Med Chem,* 10**,** 4057-65.

GAO, W., CHO, E., LIU, Y. & LU, Y. 2019. Advances and challenges in cell-free incorporation of unnatural amino acids into proteins. *Frontiers in pharmacology,* 10**,** 611.

GAROUSI, J., ORLOVA, A., FREJD, F. Y. & TOLMACHEV, V. 2020. Imaging using radiolabelled targeted proteins: radioimmunodetection and beyond. *EJNMMI Radiopharmacy and Chemistry,* 5**,** 16.

GASTON, J., MAESTRALI, N., LALLE, G., GAGNAIRE, M., MASIERO, A., DUMAS, B., DABDOUBI, T., RADOSEVIC, K. & BERNE, P. F. 2019. Intracellular delivery of therapeutic antibodies into specific cells using antibody-peptide fusions. *Sci Rep,* 9**,** 18688.

GAUTHIER, M. A. & KLOK, H.-A. 2008. Peptide/protein–polymer conjugates: synthetic strategies and design concepts. *Chemical Communications***,** 2591-2611.

GORGOULIS, V. G., VASSILIOU, L. V., KARAKAIDOS, P., ZACHARATOS, P., KOTSINAS, A., LILOGLOU, T., VENERE, M., DITULLIO, R. A., JR., KASTRINAKIS, N. G., LEVY, B., KLETSAS, D., YONETA, A., HERLYN, M., KITTAS, C. & HALAZONETIS, T. D. 2005. Activation of the DNA damage checkpoint and genomic instability in human precancerous lesions. *Nature,* 434**,** 907-13.

GREEN, L. L., HARDY, M. C., MAYNARD-CURRIE, C. E., TSUDA, H., LOUIE, D. M., MENDEZ, M. J., ABDERRAHIM, H., NOGUCHI, M., SMITH, D. H., ZENG, Y.,

DAVID, N. E., SASAI, H., GARZA, D., BRENNER, D. G., HALES, J. F., MCGUINNESS, R. P., CAPON, D. J., KLAPHOLZ, S. & JAKOBOVITS, A. 1994. Antigen-specific human monoclonal antibodies from mice engineered with human Ig heavy and light chain YACs. *Nat Genet,* 7**,** 13-21.

GUIDOTTI, G., BRAMBILLA, L. & ROSSI, D. 2017. Cell-Penetrating Peptides: From Basic Research to Clinics. *Trends Pharmacol Sci,* 38**,** 406-424.

HAMID, O., ROBERT, C., DAUD, A., HODI, F. S., HWU, W. J., KEFFORD, R., WOLCHOK, J. D., HERSEY, P., JOSEPH, R. W., WEBER, J. S., DRONCA, R., GANGADHAR, T. C., PATNAIK, A., ZAROUR, H., JOSHUA, A. M., GERGICH, K., ELASSAISS-SCHAAP, J., ALGAZI, A., MATEUS, C., BOASBERG, P., TUMEH, P. C., CHMIELOWSKI, B., EBBINGHAUS, S. W., LI, X. N., KANG, S. P. & RIBAS, A. 2013. Safety and tumor responses with lambrolizumab (anti-PD-1) in melanoma. *N Engl J Med,* 369**,** 134-44.

HANAHAN, D. & WEINBERG, R. A. 2000. The hallmarks of cancer. *Cell,* 100**,** 57-70.

HANAHAN, D. & WEINBERG, R. A. 2011. Hallmarks of cancer: the next generation. *Cell,* 144**,** 646-74.

HERMANSON, G. T. 2013. *Bioconjugate techniques,* London ; Waltham, MA, Elsevier/AP.

HSIEH, P. C., LEE, I. H., YEH, T. L., CHEN, K. C., HUANG, H. C., CHEN, P. S., YANG, Y. K., YAO, W. J., LU, R.-B. & CHIU, N. T. 2010. Distribution volume ratio of serotonin and dopamine transporters in euthymic patients with a history of major depression — a dual-isotope SPECT study. *Psychiatry Research: Neuroimaging,* 184**,** 157-161.

HU, M., CHEN, P., WANG, J., SCOLLARD, D. A., VALLIS, K. A. & REILLY, R. M. 2007. 123I-labeled HIV-1 tat peptide radioimmunoconjugates are imported into the nucleus of human breast cancer cells and functionally interact in vitro and in vivo with the cyclin-

dependent kinase inhibitor, p21(WAF-1/Cip-1). *Eur J Nucl Med Mol Imaging,* 34**,** 368-77.

HU, Y. B., DAMMER, E. B., REN, R. J. & WANG, G. 2015. The endosomal-lysosomal system: from acidification and cargo sorting to neurodegeneration. *Transl Neurodegener,* 4**,** 18.

HUANG, S., ARMSTRONG, E. A., BENAVENTE, S., CHINNAIYAN, P. & HARARI, P. M. 2004. Dual-agent molecular targeting of the epidermal growth factor receptor (EGFR): combining anti-EGFR antibody with tyrosine kinase inhibitor. *Cancer Res,* 64**,** 5355-62.

HUTTON, B. F. 2014. The origins of SPECT and SPECT/CT. *Eur J Nucl Med Mol Imaging,* 41 Suppl 1**,** S3-16.

INFORMA. 2020. *Pharma R&D Annual Review 2020 Whitepaper* [Online]. Available: https://pharmaintelligence.informa.com/resources/product-content/pharma-rd-annual-review-2020-whitepaper [Accessed 2020].

JACKSON, S. P. & BARTEK, J. 2009. The DNA-damage response in human biology and disease. *Nature,* 461**,** 1071-8.

JAFFEE, E. M., DANG, C. V., AGUS, D. B., ALEXANDER, B. M., ANDERSON, K. C., ASHWORTH, A., BARKER, A. D., BASTANI, R., BHATIA, S., BLUESTONE, J. A., BRAWLEY, O., BUTTE, A. J., COIT, D. G., DAVIDSON, N. E., DAVIS, M., DEPINHO, R. A., DIASIO, R. B., DRAETTA, G., FRAZIER, A. L., FUTREAL, A., GAMBHIR, S. S., GANZ, P. A., GARRAWAY, L., GERSON, S., GUPTA, S., HEATH, J., HOFFMAN, R. I., HUDIS, C., HUGHES-HALBERT, C., IBRAHIM, R., JADVAR, H., KAVANAGH, B., KITTLES, R., LE, Q. T., LIPPMAN, S. M., MANKOFF, D., MARDIS, E. R., MAYER, D. K., MCMASTERS, K., MEROPOL, N. J., MITCHELL, B., NAREDI, P., ORNISH, D., PAWLIK, T. M., PEPPERCORN, J.,

POMPER, M. G., RAGHAVAN, D., RITCHIE, C., SCHWARZ, S. W., SULLIVAN, R., WAHL, R., WOLCHOK, J. D., WONG, S. L. & YUNG, A. 2017. Future cancer research priorities in the USA: a Lancet Oncology Commission. *Lancet Oncol,* 18**,** e653-e706.

JAMES, M. L. & GAMBHIR, S. S. 2012. A molecular imaging primer: modalities, imaging agents, and applications. *Physiol Rev,* 92**,** 897-965.

JOLIOT, A., PERNELLE, C., DEAGOSTINI-BAZIN, H. & PROCHIANTZ, A. 1991. Antennapedia homeobox peptide regulates neural morphogenesis. *Proc Natl Acad Sci U S A,* 88**,** 1864-8.

JUCAITE, A., STENKRONA, P., CSELÉNYI, Z., DE VITA, S., BUIL-BRUNA, N., VARNÄS, K., SAVAGE, A., VARRONE, A., JOHNSTRÖM, P., SCHOU, M., DAVISON, C., SYKES, A., REDDY, V. P., HOCH, M., VAZQUEZ-ROMERO, A., MOEIN, M. M., HALLDIN, C., MERCHANT, M. S., PASS, M. & FARDE, L. 2020. Brain exposure of the ATM inhibitor AZD1390 in humans - a positron emission tomography (PET) study. *Neuro-Oncology*.

KANAZAWA, T., MORISAKI, K., SUZUKI, S. & TAKASHIMA, Y. 2014. Prolongation of life in rats with malignant glioma by intranasal siRNA/drug codelivery to the brain with cell-penetrating peptide-modified micelles. *Mol Pharm,* 11**,** 1471-8.

KANDA, T., SULLIVAN, K. F. & WAHL, G. M. 1998. Histone-GFP fusion protein enables sensitive analysis of chromosome dynamics in living mammalian cells. *Curr Biol,* 8**,** 377-85.

KAPLAN, I. M., WADIA, J. S. & DOWDY, S. F. 2005. Cationic TAT peptide transduction domain enters cells by macropinocytosis. *J Control Release,* 102**,** 247-53.

KAUFFMAN, W. B., FUSELIER, T., HE, J. & WIMLEY, W. C. 2015. Mechanism Matters: A Taxonomy of Cell Penetrating Peptides. *Trends Biochem Sci,* 40**,** 749-764.

KAUR, P., TOMECHKO, S. E., KISELAR, J., SHI, W., DEPERALTA, G., WECKSLER, A. T., GOKULRANGAN, G., LING, V. & CHANCE, M. R. 2015. Characterizing monoclonal antibody structure by carboxyl group footprinting. *MAbs,* 7**,** 540-52.

KAWAGUCHI, Y., TAKEUCHI, T., KUWATA, K., CHIBA, J., HATANAKA, Y., NAKASE, I. & FUTAKI, S. 2016. Syndecan-4 Is a Receptor for Clathrin-Mediated Endocytosis of Arginine-Rich Cell-Penetrating Peptides. *Bioconjug Chem,* 27**,** 1119-30.

KENANOVA, V., BARAT, B., OLAFSEN, T., CHATZIIOANNOU, A., HERSCHMAN, H. R., BRAUN, J. & WU, A. M. 2009. Recombinant carcinoembryonic antigen as a reporter gene for molecular imaging. *Eur J Nucl Med Mol Imaging,* 36**,** 104-14.

KERSEMANS, V., GILCHRIST, S., WALLINGTON, S., ALLEN, P. D., GOMES, A. L., DIAS, G. M., CORNELISSEN, B., KINCHESH, P. & SMART, S. C. 2019. A Carbon-Fiber Sheet Resistor for MR-, CT-, SPECT-, and PET-Compatible Temperature Maintenance in Small Animals. *Tomography,* 5**,** 274-281.

KERSEMANS, V., KERSEMANS, K. & CORNELISSEN, B. 2008. Cell penetrating peptides for in vivo molecular imaging applications. *Curr Pharm Des,* 14**,** 2415-47.

KEYES, J. W., JR., ORLANDEA, N., HEETDERKS, W. J., LEONARD, P. F. & ROGERS, W. L. 1977. The Humongotron--a scintillation-camera transaxial tomograph. *J Nucl Med,* 18**,** 381-7.

KHANNA, K. K. & JACKSON, S. P. 2001. DNA double-strand breaks: signaling, repair and the cancer connection. *Nat Genet,* 27**,** 247-54.

KHONGORZUL, P., LING, C. J., KHAN, F. U., IHSAN, A. U. & ZHANG, J. 2020. Antibody–Drug Conjugates: A Comprehensive Review. *Molecular Cancer Research,* 18**,** 3.

KIRKHAM, M. & PARTON, R. G. 2005. Clathrin-independent endocytosis: new insights into caveolae and non-caveolar lipid raft carriers. *Biochim Biophys Acta,* 1746**,** 349-63.

KNIGHT, J. C., BAGUNA TORRES, J., GOLDIN, R., MOSLEY, M., DIAS, G. M., CONTRERAS BRAVO, L., KERSEMANS, V., ALLEN, P. D., MUKHERJEE, S., SMART, S. C. & CORNELISSEN, B. 2019a. Early Detection in a Mouse Model of Pancreatic Cancer by Imaging DNA Damage Response Signalling. *J Nucl Med*.

KNIGHT, J. C., MOSLEY, M. J., BRAVO, L. C., KERSEMANS, V., ALLEN, P. D., MUKHERJEE, S., O'NEILL, E. & CORNELISSEN, B. 2017. (89)Zr-anti-gammaH2AX-TAT but not (18)F-FDG Allows Early Monitoring of Response to Chemotherapy in a Mouse Model of Pancreatic Ductal Adenocarcinoma. *Clin Cancer Res,* 23**,** 6498-6504.

KNIGHT, J. C., MOSLEY, M. J., KERSEMANS, V., DIAS, G. M., ALLEN, P. D., SMART, S. & CORNELISSEN, B. 2019b. Dual-isotope imaging allows in vivo immunohistochemistry using radiolabelled antibodies in tumours. *Nuclear Medicine and Biology,* 70**,** 14-22.

KNIGHT, J. C., TOPPING, C., MOSLEY, M., KERSEMANS, V., FALZONE, N., FERNANDEZ-VAREA, J. M. & CORNELISSEN, B. 2015. PET imaging of DNA damage using (89)Zr-labelled anti-gammaH2AX-TAT immunoconjugates. *Eur J Nucl Med Mol Imaging,* 42**,** 1707-1717.

KOHLER, G. & MILSTEIN, C. 1975. Continuous cultures of fused cells secreting antibody of predefined specificity. *Nature,* 256**,** 495-7.

KOPPE, M. J., POSTEMA, E. J., AARTS, F., OYEN, W. J., BLEICHRODT, R. P. & BOERMAN, O. C. 2005. Antibody-guided radiation therapy of cancer. *Cancer Metastasis Rev,* 24**,** 539-67.

KOSUGE, M., TAKEUCHI, T., NAKASE, I., JONES, A. T. & FUTAKI, S. 2008. Cellular internalization and distribution of arginine-rich peptides as a function of extracellular

peptide concentration, serum, and plasma membrane associated proteoglycans. *Bioconjug Chem,* 19**,** 656-64.

KOZLOV, S. V., GRAHAM, M. E., JAKOB, B., TOBIAS, F., KIJAS, A. W., TANUJI, M., CHEN, P., ROBINSON, P. J., TAUCHER-SCHOLZ, G., SUZUKI, K., SO, S., CHEN, D. & LAVIN, M. F. 2011. Autophosphorylation and ATM activation: additional sites add to the complexity. *J Biol Chem,* 286**,** 9107-19.

KRAPP, S., MIMURA, Y., JEFFERIS, R., HUBER, R. & SONDERMANN, P. 2003. Structural Analysis of Human IgG-Fc Glycoforms Reveals a Correlation Between Glycosylation and Structural Integrity. *Journal of Molecular Biology,* 325**,** 979-989.

KU, A., FACCA, V. J., CAI, Z. & REILLY, R. M. 2019. Auger electrons for cancer therapy – a review. *EJNMMI Radiopharmacy and Chemistry,* 4**,** 27.

LECHER, J. C., NOWAK, S. J. & MCMURRY, J. L. 2017. Breaking in and busting out: cell-penetrating peptides and the endosomal escape problem. *Biomolecular concepts,* 8**,** 131-141.

LEE, J. H. & PAULL, T. T. 2005. ATM activation by DNA double-strand breaks through the Mre11-Rad50-Nbs1 complex. *Science,* 308**,** 551-4.

LEE, Y. J., DATTA, S. & PELLOIS, J. P. 2008. Real-time fluorescence detection of protein transduction into live cells. *J Am Chem Soc,* 130**,** 2398-9.

LETOHA, T., KELLER-PINTÉR, A., KUSZ, E., KOLOZSI, C., BOZSÓ, Z., TÓTH, G., VIZLER, C., OLÁH, Z. & SZILÁK, L. 2010. Cell-penetrating peptide exploited syndecans. *Biochimica et Biophysica Acta (BBA) - Biomembranes,* 1798**,** 2258-2265.

LI, Z., KRIPPENDORFF, B. F., SHARMA, S., WALZ, A. C., LAVE, T. & SHAH, D. K. 2016. Influence of molecular size on tissue distribution of antibody fragments. *MAbs,* 8**,** 113-9.

LIBERTI, M. V. & LOCASALE, J. W. 2016. The Warburg Effect: How Does it Benefit Cancer Cells? *Trends Biochem Sci,* 41**,** 211-218.

LINDAHL, T. & BARNES, D. E. 2000. Repair of endogenous DNA damage. *Cold Spring Harb Symp Quant Biol,* 65**,** 127-33.

LIU, H., CHUMSAE, C., GAZA-BULSECO, G., HURKMANS, K. & RADZIEJEWSKI, C. H. 2010. Ranking the susceptibility of disulfide bonds in human IgG1 antibodies by reduction, differential Alkylation, and LC− MS analysis. *Analytical chemistry,* 82**,** 5219-5226.

LONN, P., KACSINTA, A. D., CUI, X. S., HAMIL, A. S., KAULICH, M., GOGOI, K. & DOWDY, S. F. 2016. Enhancing Endosomal Escape for Intracellular Delivery of Macromolecular Biologic Therapeutics. *Sci Rep,* 6**,** 32301.

LU, S. X., TAKACH, E. J., SOLOMON, M., ZHU, Q., LAW, S. J. & HSIEH, F. Y. 2005. Mass spectral analyses of labile DOTA-NHS and heterogeneity determination of DOTA or DM1 conjugated anti-PSMA antibody for prostate cancer therapy. *J Pharm Sci,* 94**,** 788-97.

LUNDBERG, P. & LANGEL, U. 2003. A brief introduction to cell-penetrating peptides. *J Mol Recognit,* 16**,** 227-33.

LUTJE, S., VAN RIJ, C. M., FRANSSEN, G. M., FRACASSO, G., HELFRICH, W., EEK, A., OYEN, W. J., COLOMBATTI, M. & BOERMAN, O. C. 2015. Targeting human prostate cancer with 111In-labeled D2B IgG, F(ab')2 and Fab fragments in nude mice with PSMA-expressing xenografts. *Contrast Media Mol Imaging,* 10**,** 28-36.

MAEDA, H., NAKAMURA, H. & FANG, J. 2013. The EPR effect for macromolecular drug delivery to solid tumors: Improvement of tumor uptake, lowering of systemic toxicity, and distinct tumor imaging in vivo. *Adv Drug Deliv Rev,* 65**,** 71-9.

MALONEY, D. G., GRILLO-LOPEZ, A. J., WHITE, C. A., BODKIN, D., SCHILDER, R. J., NEIDHART, J. A., JANAKIRAMAN, N., FOON, K. A., LILES, T. M., DALLAIRE, B. K., WEY, K., ROYSTON, I., DAVIS, T. & LEVY, R. 1997. IDEC-C2B8 (Rituximab) anti-CD20 monoclonal antibody therapy in patients with relapsed low-grade non-Hodgkin's lymphoma. *Blood,* 90**,** 2188-95.

MARCULESCU, C., LAKSHMINARAYANAN, A., GAULT, J., KNIGHT, J. C., FOLKES, L. K., SPINK, T., ROBINSON, C. V., VALLIS, K., DAVIS, B. G. & CORNELISSEN, B. 2019. Probing the limits of Q-tag bioconjugation of antibodies. *Chemical Communications,* 55**,** 11342-11345.

MASTRANGELI, R., PALINSKY, W. & BIERAU, H. 2019. Glycoengineered antibodies: towards the next-generation of immunotherapeutics. *Glycobiology,* 29**,** 199-210.

MAYOR, S., PARTON, R. G. & DONALDSON, J. G. 2014. Clathrin-independent pathways of endocytosis. *Cold Spring Harb Perspect Biol,* 6.

MCAULEY, A., JACOB, J., KOLVENBACH, C. G., WESTLAND, K., LEE, H. J., BRYCH, S. R., REHDER, D., KLEEMANN, G. R., BREMS, D. N. & MATSUMURA, M. 2008. Contributions of a disulfide bond to the structure, stability, and dimerization of human IgG1 antibody CH3 domain. *Protein Science,* 17**,** 95-106.

MCMAHON, H. T. & BOUCROT, E. 2011. Molecular mechanism and physiological functions of clathrin-mediated endocytosis. *Nature reviews Molecular cell biology,* 12**,** 517-533.

MEDICINE, U. N. L. O. 2020. ClinicalTrials.gov.

MUELLER, B. M., WRASIDLO, W. A. & REISFELD, R. A. 1988. Determination of the number of e-amino groups available for conjugation of effector molecules to monoclonal antibodies. *Hybridoma,* 7**,** 453-6.

MUSSBACH, F., FRANKE, M., ZOCH, A., SCHAEFER, B. & REISSMANN, S. 2011. Transduction of peptides and proteins into live cells by cell penetrating peptides. *J Cell Biochem,* 112**,** 3824-33.

NAKASE, I., OSAKI, K., TANAKA, G., UTANI, A. & FUTAKI, S. 2014. Molecular interplays involved in the cellular uptake of octaarginine on cell surfaces and the importance of syndecan-4 cytoplasmic V domain for the activation of protein kinase Calpha. *Biochem Biophys Res Commun,* 446**,** 857-62.

NAKASE, I., TADOKORO, A., KAWABATA, N., TAKEUCHI, T., KATOH, H., HIRAMOTO, K., NEGISHI, M., NOMIZU, M., SUGIURA, Y. & FUTAKI, S. 2007. Interaction of arginine-rich peptides with membrane-associated proteoglycans is crucial for induction of actin organization and macropinocytosis. *Biochemistry,* 46**,** 492-501.

NAKAYAMA, F., YASUDA, T., UMEDA, S., ASADA, M., IMAMURA, T., MEINEKE, V. & AKASHI, M. 2011. Fibroblast growth factor-12 (FGF12) translocation into intestinal epithelial cells is dependent on a novel cell-penetrating peptide domain: involvement of internalization in the in vivo role of exogenous FGF12. *J Biol Chem,* 286**,** 25823-34.

NALDINI, L., TRONO, D. & VERMA, I. M. 2016. Lentiviral vectors, two decades later. *Science,* 353**,** 1101-1102.

NISCHAN, N., HERCE, H. D., NATALE, F., BOHLKE, N., BUDISA, N., CARDOSO, M. C. & HACKENBERGER, C. P. 2015. Covalent attachment of cyclic TAT peptides to GFP results in protein delivery into live cells with immediate bioavailability. *Angew Chem Int Ed Engl,* 54**,** 1950-3.

O'NEILL, E., KERSEMANS, V., ALLEN, P. D., TERRY, S. Y. A., TORRES, J. B., MOSLEY, M., SMART, S., LEE, B. Q., FALZONE, N., VALLIS, K. A., KONIJNENBERG, M. W., DE JONG, M., NONNEKENS, J. & CORNELISSEN, B.

2020. Imaging DNA Damage Repair In Vivo After (177)Lu-DOTATATE Therapy. *J Nucl Med,* 61**,** 743-750.

PANG, H. B., BRAUN, G. B. & RUOSLAHTI, E. 2015. Neuropilin-1 and heparan sulfate proteoglycans cooperate in cellular uptake of nanoparticles functionalized by cationic cell-penetrating peptides. *Sci Adv,* 1**,** e1500821.

PARK, H. I., YOON, H. W. & JUNG, S. T. 2016. The Highly Evolvable Antibody Fc Domain. *Trends Biotechnol,* 34**,** 895-908.

PARTON, R. G. 2018. Caveolae: Structure, Function, and Relationship to Disease. *Annu Rev Cell Dev Biol,* 34**,** 111-136.

PATEL, S. G., SAYERS, E. J., HE, L., NARAYAN, R., WILLIAMS, T. L., MILLS, E. M., ALLEMANN, R. K., LUK, L. Y. P., JONES, A. T. & TSAI, Y. H. 2019. Cell-penetrating peptide sequence and modification dependent uptake and subcellular distribution of green florescent protein in different cell lines. *Sci Rep,* 9**,** 6298.

PAULL, T. T. 2015. Mechanisms of ATM Activation. *Annu Rev Biochem,* 84**,** 711-38.

PEI, D. & BUYANOVA, M. 2019. Overcoming Endosomal Entrapment in Drug Delivery. *Bioconjug Chem,* 30**,** 273-283.

PETRONI, D., MENICHETTI, L. & POLI, M. 2020. Historical and radiopharmaceutical relevance of [18F]FDG. *Journal of Radioanalytical and Nuclear Chemistry,* 323**,** 1017-1031.

POOGA, M. & LANGEL, U. 2015. Classes of Cell-Penetrating Peptides. *Methods Mol Biol,* 1324**,** 3-28.

POTY, S., MANDLEYWALA, K., O'NEILL, E., KNIGHT, J. C., CORNELISSEN, B. & LEWIS, J. S. 2020. (89)Zr-PET imaging of DNA double-strand breaks for the early monitoring of response following alpha- and beta-particle radioimmunotherapy in a mouse model of pancreatic ductal adenocarcinoma. *Theranostics,* 10**,** 5802-5814.

PRICE, E. W. & ORVIG, C. 2014. Matching chelators to radiometals for radiopharmaceuticals. *Chem Soc Rev,* 43**,** 260-90.

PYZIK, M., RATH, T., LENCER, W. I., BAKER, K. & BLUMBERG, R. S. 2015. FcRn: The Architect Behind the Immune and Nonimmune Functions of IgG and Albumin. *J Immunol,* 194**,** 4595-603.

QIAN, Z., MARTYNA, A., HARD, R. L., WANG, J., APPIAH-KUBI, G., COSS, C., PHELPS, M. A., ROSSMAN, J. S. & PEI, D. 2016. Discovery and Mechanism of Highly Efficient Cyclic Cell-Penetrating Peptides. *Biochemistry,* 55**,** 2601-12.

RANADIVE, G. N., ROSENZWEIG, H. S., EPPERLY, M. W., SESKEY, T. & BLOOMER, W. D. 1993. A new method of technetium-99m labeling of monoclonal antibodies through sugar residues. A study with TAG-72 specific CC-49 antibody. *Nuclear medicine and biology,* 20**,** 719-726.

REDDY, S. & ROBINSON, M. K. 2010. Immuno-positron emission tomography in cancer models. *Semin Nucl Med,* 40**,** 182-9.

REJMAN, J., OBERLE, V., ZUHORN, I. S. & HOEKSTRA, D. 2004. Size-dependent internalization of particles via the pathways of clathrin- and caveolae-mediated endocytosis. *Biochem J,* 377**,** 159-69.

RICHARD, J. P., MELIKOV, K., BROOKS, H., PREVOT, P., LEBLEU, B. & CHERNOMORDIK, L. V. 2005. Cellular uptake of unconjugated TAT peptide involves clathrin-dependent endocytosis and heparan sulfate receptors. *J Biol Chem,* 280**,** 15300-6.

RITZEFELD, M. 2014. Sortagging: a robust and efficient chemoenzymatic ligation strategy. *Chemistry (Weinheim an der Bergstrasse, Germany),* 20.

ROSESTEDT, M., ANDERSSON, K. G., MITRAN, B., TOLMACHEV, V., LOFBLOM, J., ORLOVA, A. & STAHL, S. 2015. Affibody-mediated PET imaging of HER3 expression in malignant tumours. *Sci Rep,* 5**,** 15226.

RUSESKA, I. & ZIMMER, A. 2020. Internalization mechanisms of cell-penetrating peptides. *Beilstein J Nanotechnol,* 11**,** 101-123.

SAALIK, P., PADARI, K., NIINEP, A., LORENTS, A., HANSEN, M., JOKITALO, E., LANGEL, U. & POOGA, M. 2009. Protein delivery with transportans is mediated by caveolae rather than flotillin-dependent pathways. *Bioconjug Chem,* 20**,** 877-87.

SAHNI, A., QIAN, Z. & PEI, D. 2020. Cell-Penetrating Peptides Escape the Endosome by Inducing Vesicle Budding and Collapse. *ACS Chem Biol,* 15**,** 2485-2492.

SCHECK, R. A. & FRANCIS, M. B. 2007. Regioselective labeling of antibodies through N-terminal transamination. *ACS chemical biology,* 2**,** 247-251.

SERVICE, N. H. 2020. *2018/19 National Cost Collection data* [Online]. NHS Improvement. Available: https://improvement.nhs.uk/resources/national-cost-collection/#ncc1819 [Accessed].

SHAIKEN, T. E. & OPEKUN, A. R. 2014. Dissecting the cell to nucleus, perinucleus and cytosol. *Sci Rep,* 4**,** 4923.

SHERR, C. J. 2004. Principles of tumor suppression. *Cell,* 116**,** 235-246.

SHILOH, Y. & ZIV, Y. 2013. The ATM protein kinase: regulating the cellular response to genotoxic stress, and more. *Nat Rev Mol Cell Biol,* 14**,** 197-210.

SMITH, A. F., HALL, P. S., HULME, C. T., DUNN, J. A., MCCONKEY, C. C., RAHMAN, J. K., MCCABE, C. & MEHANNA, H. 2017a. Cost-effectiveness analysis of PET-CT-guided management for locally advanced head and neck cancer. *Eur J Cancer,* 85**,** 6-14.

SMITH, K. M., HIMIARI, Z., TSIMBALYUK, S. & FORWOOD, J. K. 2017b. Structural Basis for Importin-alpha Binding of the Human Immunodeficiency Virus Tat. *Sci Rep,* 7**,** 1650.

SONAWANE, N. D., SZOKA, F. C., JR. & VERKMAN, A. S. 2003. Chloride accumulation and swelling in endosomes enhances DNA transfer by polyamine-DNA polyplexes. *J Biol Chem,* 278**,** 44826-31.

STAECKER, H., JOKOVIC, G., KARPISHCHENKO, S., KIENLE-GOGOLOK, A., KRZYZANIAK, A., LIN, C. D., NAVRATIL, P., TZVETKOV, V., WRIGHT, N. & MEYER, T. 2019. Efficacy and Safety of AM-111 in the Treatment of Acute Unilateral Sudden Deafness-A Double-blind, Randomized, Placebo-controlled Phase 3 Study. *Otol Neurotol,* 40**,** 584-594.

STIMMEL, J. B., MERRILL, B. M., MOXHAM, C. P., HUTCHINS, J. T., KULL JR, F. C., KUYPER, L. F. & FLING, M. E. 2000. Site-specific conjugation on serine→ cysteine variant monoclonal antibodies. *Journal of Biological Chemistry,* 275**,** 30445-30450.

STREBHARDT, K. & ULLRICH, A. 2008. Paul Ehrlich's magic bullet concept: 100 years of progress. *Nature Reviews Cancer,* 8**,** 473-480.

STROHL, W. R. 2018. Current progress in innovative engineered antibodies. *Protein Cell,* 9**,** 86-120.

STROP, P. 2014. Versatility of microbial transglutaminase. *Bioconjugate chemistry,* 25**,** 855-862.

SUNG, M., POON, G. M. & GARIEPY, J. 2006. The importance of valency in enhancing the import and cell routing potential of protein transduction domain-containing molecules. *Biochim Biophys Acta,* 1758**,** 355-63.

SUZUKI, T., FUTAKI, S., NIWA, M., TANAKA, S., UEDA, K. & SUGIURA, Y. 2002. Possible existence of common internalization mechanisms among arginine-rich peptides. *J Biol Chem,* 277**,** 2437-43.

SWANSON, J. A. & KING, J. S. 2019. The breadth of macropinocytosis research. *Philos Trans R Soc Lond B Biol Sci,* 374**,** 20180146.

TANAKA, G., NAKASE, I., FUKUDA, Y., MASUDA, R., OISHI, S., SHIMURA, K., KAWAGUCHI, Y., TAKATANI-NAKASE, T., LANGEL, U., GRASLUND, A., OKAWA, K., MATSUOKA, M., FUJII, N., HATANAKA, Y. & FUTAKI, S. 2012. CXCR4 stimulates macropinocytosis: implications for cellular uptake of arginine-rich cell-penetrating peptides and HIV. *Chem Biol,* 19**,** 1437-46.

TIBAU, A., MOLTO, C., OCANA, A., TEMPLETON, A. J., DEL CARPIO, L. P., DEL PAGGIO, J. C., BARNADAS, A., BOOTH, C. M. & AMIR, E. 2018. Magnitude of Clinical Benefit of Cancer Drugs Approved by the US Food and Drug Administration. *J Natl Cancer Inst,* 110**,** 486-492.

TRABULO, S., CARDOSO, A. L., MANO, M. & DE LIMA, M. C. 2010. Cell-Penetrating Peptides-Mechanisms of Cellular Uptake and Generation of Delivery Systems. *Pharmaceuticals (Basel),* 3**,** 961-993.

TRUANT, R. & CULLEN, B. R. 1999. The arginine-rich domains present in human immunodeficiency virus type 1 Tat and Rev function as direct importin beta-dependent nuclear localization signals. *Mol Cell Biol,* 19**,** 1210-7.

TUMEY, L. N., CHARATI, M., HE, T., SOUSA, E., MA, D., HAN, X., CLARK, T., CASAVANT, J., LOGANZO, F. & BARLETTA, F. 2014. Mild method for succinimide hydrolysis on ADCs: impact on ADC potency, stability, exposure, and efficacy. *Bioconjugate chemistry,* 25**,** 1871-1880.

TUNNEMANN, G., MARTIN, R. M., HAUPT, S., PATSCH, C., EDENHOFER, F. & CARDOSO, M. C. 2006. Cargo-dependent mode of uptake and bioavailability of TAT-containing proteins and peptides in living cells. *FASEB J,* 20**,** 1775-84.

UR REHMAN, Z., HOEKSTRA, D. & ZUHORN, I. S. 2013. Mechanism of polyplex- and lipoplex-mediated delivery of nucleic acids: real-time visualization of transient membrane destabilization without endosomal lysis. *ACS Nano,* 7**,** 3767-77.

URQUHART, L. 2020. Top companies and drugs by sales in 2019. *Nat Rev Drug Discov,* 19**,** 228.

VAN DE WATERING, F. C. J., RIJPKEMA, M., PERK, L., BRINKMANN, U., OYEN, W. J. G. & BOERMAN, O. C. 2014. Zirconium-89 Labeled Antibodies: A New Tool for Molecular Imaging in Cancer Patients. *BioMed Research International,* 2014**,** 203601.

VAN DER BRUGGEN, W., BLEEKER-ROVERS, C. P., BOERMAN, O. C., GOTTHARDT, M. & OYEN, W. J. G. 2010. PET and SPECT in Osteomyelitis and Prosthetic Bone and Joint Infections: A Systematic Review. *Seminars in Nuclear Medicine,* 40**,** 3-15.

VARKOUHI, A. K., SCHOLTE, M., STORM, G. & HAISMA, H. J. 2011. Endosomal escape pathways for delivery of biologicals. *J Control Release,* 151**,** 220-8.

VAUGHAN, T. J., WILLIAMS, A. J., PRITCHARD, K., OSBOURN, J. K., POPE, A. R., EARNSHAW, J. C., MCCAFFERTY, J., HODITS, R. A., WILTON, J. & JOHNSON, K. S. 1996. Human Antibodies with Sub-nanomolar Affinities Isolated from a Large Non-immunized Phage Display Library. *Nature Biotechnology,* 14**,** 309-314.

VIEIRA, P. & RAJEWSKY, K. 1988. The half-lives of serum immunoglobulins in adult mice. *Eur J Immunol,* 18**,** 313-6.

VIOLA-VILLEGAS, N. T., SEVAK, K. K., CARLIN, S. D., DORAN, M. G., EVANS, H. W., BARTLETT, D. W., WU, A. M. & LEWIS, J. S. 2014. Noninvasive Imaging of PSMA

in prostate tumors with (89)Zr-Labeled huJ591 engineered antibody fragments: the faster alternatives. *Mol Pharm,* 11**,** 3965-73.

VIVES, E., BRODIN, P. & LEBLEU, B. 1997. A truncated HIV-1 Tat protein basic domain rapidly translocates through the plasma membrane and accumulates in the cell nucleus. *J Biol Chem,* 272**,** 16010-7.

VIVES, E., RICHARD, J. P., RISPAL, C. & LEBLEU, B. 2003. TAT peptide internalization: seeking the mechanism of entry. *Curr Protein Pept Sci,* 4**,** 125-32.

WADIA, J. S., STAN, R. V. & DOWDY, S. F. 2004. Transducible TAT-HA fusogenic peptide enhances escape of TAT-fusion proteins after lipid raft macropinocytosis. *Nat Med,* 10**,** 310-5.

WAKANKAR, A. A., FEENEY, M. B., RIVERA, J., CHEN, Y., KIM, M., SHARMA, V. K. & WANG, Y. J. 2010. Physicochemical stability of the antibody-drug conjugate Trastuzumab-DM1: changes due to modification and conjugation processes. *Bioconjug Chem,* 21**,** 1588-95.

WEBER, W. A., CZERNIN, J., ANDERSON, C. J., BADAWI, R. D., BARTHEL, H., BENGEL, F., BODEI, L., BUVAT, I., DICARLI, M., GRAHAM, M. M., GRIMM, J., HERRMANN, K., KOSTAKOGLU, L., LEWIS, J. S., MANKOFF, D. A., PETERSON, T. E., SCHELBERT, H., SCHODER, H., SIEGEL, B. A. & STRAUSS, H. W. 2020. The Future of Nuclear Medicine, Molecular Imaging, and Theranostics. *J Nucl Med,* 61**,** 263S-272S.

WENDER, P. A., MITCHELL, D. J., PATTABIRAMAN, K., PELKEY, E. T., STEINMAN, L. & ROTHBARD, J. B. 2000. The design, synthesis, and evaluation of molecules that enable or enhance cellular uptake: peptoid molecular transporters. *Proc Natl Acad Sci U S A,* 97**,** 13003-8.

WERNICK, M. N. & AARSVOLD, J. N. 2004. *Emission tomography: the fundamentals of PET and SPECT*, Elsevier.

WHITE, J. M., ESCORCIA, F. E. & VIOLA, N. T. 2021. Perspectives on metals-based radioimmunotherapy (RIT): moving forward. *Theranostics,* 11**,** 6293-6314.

WILD, C., WEIDERPASS, E., STEWART, B. W., INTERNATIONAL AGENCY FOR RESEARCH ON CANCER & WORLD HEALTH ORGANIZATION 2020. *World cancer report 2020,* Lyon, France

Geneva, Switzerland, International Agency for Research on Cancer

WHO Press.

WILSON, T. C., XAVIER, M. A., KNIGHT, J., VERHOOG, S., TORRES, J. B., MOSLEY, M., HOPKINS, S. L., WALLINGTON, S., ALLEN, P. D., KERSEMANS, V., HUETING, R., SMART, S., GOUVERNEUR, V. & CORNELISSEN, B. 2019. PET Imaging of PARP Expression Using (18)F-Olaparib. *J Nucl Med,* 60**,** 504-510.

WISNIEWSKI, J. R., HEIN, M. Y., COX, J. & MANN, M. 2014. A "proteomic ruler" for protein copy number and concentration estimation without spike-in standards. *Mol Cell Proteomics,* 13**,** 3497-506.

WOLFF, A. C., HAMMOND, M. E. H., ALLISON, K. H., HARVEY, B. E., MANGU, P. B., BARTLETT, J. M. S., BILOUS, M., ELLIS, I. O., FITZGIBBONS, P., HANNA, W., JENKINS, R. B., PRESS, M. F., SPEARS, P. A., VANCE, G. H., VIALE, G., MCSHANE, L. M. & DOWSETT, M. 2018. Human Epidermal Growth Factor Receptor 2 Testing in Breast Cancer: American Society of Clinical Oncology/College of American Pathologists Clinical Practice Guideline Focused Update. *J Clin Oncol,* 36**,** 2105-2122.

WU, A. M. 2014. Engineered antibodies for molecular imaging of cancer. *Methods,* 65**,** 139-47.

XENAKI, K. T., OLIVEIRA, S. & VAN BERGEN EN HENEGOUWEN, P. M. P. 2017. Antibody or Antibody Fragments: Implications for Molecular Imaging and Targeted Therapy of Solid Tumors. *Frontiers in immunology,* 8**,** 1287-1287.

XIAO, H., CHATTERJEE, A., CHOI, S. H., BAJJURI, K. M., SINHA, S. C. & SCHULTZ, P. G. 2013. Genetic incorporation of multiple unnatural amino acids into proteins in mammalian cells. *Angewandte Chemie,* 125**,** 14330-14333.

XIE, J., BI, Y., ZHANG, H., DONG, S., TENG, L., LEE, R. J. & YANG, Z. 2020. Cell-Penetrating Peptides in Diagnosis and Treatment of Human Diseases: From Preclinical Research to Clinical Application. *Front Pharmacol,* 11**,** 697.

YAMAGATA, M. & SANES, J. R. 2012. Transgenic strategy for identifying synaptic connections in mice by fluorescence complementation (GRASP). *Front Mol Neurosci,* 5**,** 18.

YE, J. X., PEI, X., CUI, H., YU, Z. L., LEE, H., WANG, J. X., WANG, X., SUN, L., HE, H. N. & YANG, V. C. 2018. Cellular uptake mechanism and comparative in vitro cytotoxicity studies of monomeric LMWP-siRNA conjugate. *Journal of Industrial and Engineering Chemistry,* 63**,** 103-111.

YI, M., DONG, B., QIN, S., CHU, Q., WU, K. & LUO, S. 2019. Advances and perspectives of PARP inhibitors. *Exp Hematol Oncol,* 8**,** 29.

ZEGLIS, B. M., DAVIS, C. B., AGGELER, R., KANG, H. C., CHEN, A., AGNEW, B. J. & LEWIS, J. S. 2013. Enzyme-Mediated Methodology for the Site-Specific Radiolabeling of Antibodies Based on Catalyst-Free Click Chemistry. *Bioconjugate Chemistry,* 24**,** 1057-1067.

ZHAO, F., ZHAO, Y., LIU, Y., CHANG, X., CHEN, C. & ZHAO, Y. 2011. Cellular uptake, intracellular trafficking, and cytotoxicity of nanomaterials. *Small,* 7**,** 1322-37.

ZHOU, Q., STEFANO, J. E., MANNING, C., KYAZIKE, J., CHEN, B., GIANOLIO, D. A., PARK, A., BUSCH, M., BIRD, J. & ZHENG, X. 2014. Site-specific antibody–drug conjugation through glycoengineering. *Bioconjugate chemistry,* 25**,** 510-520.

ZIV, Y., BIELOPOLSKI, D., GALANTY, Y., LUKAS, C., TAYA, Y., SCHULTZ, D. C., LUKAS, J., BEKKER-JENSEN, S., BARTEK, J. & SHILOH, Y. 2006. Chromatin relaxation in response to DNA double-strand breaks is modulated by a novel ATM- and KAP-1 dependent pathway. *Nat Cell Biol,* 8**,** 870-6.

Appendix

Target	Species	Host	Clonality	Clone ID	Supplier	Cat #
Primary Antibodies						
GFP	N/A	M	Mono	GFP-G1	Developmental Studies Hybridoma Bank, IA, USA	AB_2619561
Lamin B1	H, M, Rt	M	Mono	B-10	Santa Cruz Biotechnology, TX, USA	sc-374015
pS1981-ATM	H,M,Rt	Rb	Poly	N./A	R&D Systems, MN, USA	AF1655
pS1981-ATM	H	Rb	Mono	D25E5	Cell Signal Technology, MA, USA	13050
pS1981-ATM	H	Rb	Mono	1163B	R&D Systems, MN, USA	MAB2290
pS1981-ATM	H	M	Mono	10H11.E12	Cell Signal Technology, MA, USA	4526S
pS1981-ATM	H	Rb	Mono	EP1890Y	AbCam, Cambridge, UK	2152-1
pS1981-ATM	H,M	M	Mono	MAT3-4G10/8	Sigma-Aldrich, MO, USA	A1106
Vinculin	H, M, Rt	Rb	Mono	EPR8185	AbCam, Cambridge, UK	ab129002
γH2AX	H, M, Rt	Rb	Mono	JBW301	MerckMillipore, MA, USA	05-636-I
Secondary Antibodies						
Mouse IgG (HRP)	M	Gt	Poly	N/A	Bio-Rad, CA, USA	5178-2504
Rabbit IgG (HRP)	Rb	Gt	Poly	N/A	Invitrogen, CA, USA	656120
Mouse IgG (AF488)	M	Gt	Poly	N/A	Thermo Fisher Scientific, MA, USA	A-11001
Rabbit IgG (AF594)	Rb	Gt	Poly	N/A	Thermo Fisher Scientific, MA, USA	A32740
Mouse IgG (AF594)	M	Gt	Poly	N/A	Thermo Fisher Scientific, MA, USA	A32742

Table A.1) Antibody reference table. A complete summary of all antibodies presented in this thesis. Secondary antibodies are listed with conjugate groups in parenthesis, HRP = horseradish peroxidase, AF = Alexa Fluor. H = human, Gt – goat, M = mouse, Rb = rabbit, Rt = rat.